Spot Welding of Advanced High Strength Steels

by

Mohammad Ibraheem Khan

A thesis
presented to the University of Waterloo
in fulfillment of the
thesis requirement for the degree of
Master of Applied Science
in
Mechanical Engineering

Waterloo, Ontario, Canada, 2007

I hereby declare that I am the sole author of this thesis. This is a true copy of the thesis, including any required final revisions, as accepted by my examiners.

I understand that my thesis may be made electronically available to the public.

Abstract

Efforts to reduce vehicle weight and improve crash performance have resulted in increased application of advanced high strength steels (AHSS) and a recent focus on the weldability of these alloys. Resistance spot welding (RSW) is the primary sheet metal welding process in the manufacture of automotive assemblies. Integration of AHSS into the automotive architecture has brought renewed challenges for achieving acceptable welds. The varying alloying content and processing techniques has further complicated this initiative. The current study examines resistance spot welding of high strength and advance high strength steels including high strength low alloy (HSLA), dual phase (DP) and a ferritic-bainitic steel (590R). The mechanical properties and microstructure of these RSW welded steel alloys are detailed. Furthermore a relationship between chemistries and hardness is produced.

The effect of strain rate on the joint strength and failure mode is also an important consideration in the design of welded structures. Current literature, however, does not explain the effects of weld microstructure and there are no comprehensive comparisons of steels. This work details the relationship between the joint microstructure and impact performance of spot welded AHSS. Quasi-static and impact tests were conducted using a universal tensile tester and an instrumented drop tower, respectively. Results for elongation, failure load and energy absorption for each material are presented. Failure modes are detailed by observing weld fracture surfaces. In addition, cross-sections of partially fractured weldments were examined to detail fracture paths during static loading. Correlations between the fracture path and mechanical properties are developed using observed microstructures in the fusion zone and heat-affected-zone.

Friction stir spot welding (FSSW) has proven to be a potential candidate for spot welding AHSS. A comparative study of RSW and FSSW on spot welding AHSS has also been completed. The objective of this work is to compare the

microstructure and mechanical properties of Zn-coated DP600 AHSS (1.2mm thick) spot welds conducted using both processes. This was accomplished by examining the metallurgical cross-sections and local hardnesses of various spot weld regions. High speed data acquisition was also used to monitor process parameters and attain energy outputs for each process.

Acknowledgements

I wish to thank my academic supervisors, Dr. Y. Norman Zhou and Dr. Michael Kuntz, for their time, guidance, support and assistance in this endeavor. Their knowledge and guidance encouraged me through the journey of this research. I would also like to thank Dr. Tom North, Dr. Peter Su and Adrian Gerlich from my alma mater, the University of Toronto. Their training helped equip me for the various challenges I faced during this research.

Financial contributions to this research project included funding from AUTO21, a national research initiative supported by the Government of Canada through the Networks of Centres of Excellence Research Initiative. In particular I could not have done this without the services and supplies provided by Dofasco and Huys.

I would like to thank my family, friends and loved ones for giving me support through the good and bad times. Also, I thank members from the Centre for Advanced Materials Joining (CAMJ) at the University of Waterloo who quickly became my friends.

Table of Contents

CHAPTER 1: INTRODUCTION 1

1.1 Resistance Spot Welding 1
1.2 Advanced High Strength Steel 3
1.3 Justification and Problem 4
1.4 Objective 4
1.5 Criteria and Constrains 5
1.6 Thesis Outline 5

CHAPTER 2: LITERATURE REVIEW 6

2.1 Resistance Spot Welding of Coated and Uncoated Steel Alloys 6
2.2 Nugget Formation 8
2.3 Weldability 10
2.4 Welding Parameters 11
2.4.1 Weld current 12
2.4.2 Weld Time 12
2.4.3 Weld Force 13
2.5 Electrodes and Electrode Degradation 13
2.6 Phase Transformations 14
2.6.1 Fe-C Phase Diagram 14
2.6.2 Time-Temperature Transformation Diagrams 16
2.6.3 Carbon Equivalence 17
2.7 RSW Characterization 18
2.8 HSS and AHSS 19
2.8.1 High Strength Low Alloy 19
2.8.2 Dual Phase 20
2.8.3 590R 21
2.8.4 Transformation Induced Plasticity 22
2.9 Friction Stir Spot Welding 23
2.10 Spot Welding of AHSS 24
2.10.1 Weldability 24
2.10.2 Mechanical Performance and Microstructure 25
2.10.3 Static and Impact testing of RSW AHSS 31
2.11 Summary 33

CHAPTER 3: EXPERIMENTAL METHODS 35

3.1 Welding Equipment 35
3.1.1 Resistance Spot Welding Set-up 35
3.1.2 Data Acquisition System 36
3.1.3 Friction Stir Spot Welding 38
3.2 Material Selection 40
3.2.1 Specimen Dimensions 42
3.3 Mechanical Testing 42
3.3.1 Tensile Shear Testing 42
3.4 Impact Testing 43
3.4.1 Peel Testing 44
3.5 Parameter Optimisation 45
3.6 Metallographic Examination 46
3.6.1 Sample Preparation 46
3.6.2 Microscopy 46
3.6.3 XRD Analysis 46

CHAPTER 4: RESISTANCE SPOT WELDING OF ADVANCED HIGH STRENGTH STEEL 47

4.1 Parameter Optimization and Mechanical Properties 47
4.2 Microstructural Observations 50

4.2.1 HSLA 50
4.2.2 590R 51
4.2.3 DP600 51
4.2.4 DP780 55
4.2.5 TRIP780 55
4.3 Hardness observations 58
4.4 Discussion 58
4.4.1 Base Metal 58
4.4.2 Fusion Zone 62
4.4.3 Heat Affected Zone 67
4.5 Summary 70

CHAPTER 5: FRACTURE SURFACES AND IMPACT TESTING 71

5.1 Fracture Surfaces and Energy Input 71
5.2 Impact Testing 76
5.2.1 Data Analysis 76
5.2.2 Displacement 77
5.2.3 Energy absorption 78
5.2.4 Failure Loads 80
5.3 Impact Fracture Surfaces and Detailed Examination 81
5.3.1 HSLA 81
5.3.2 590R 82
5.3.3 DP600 83
5.3.4 DP780 85
5.3.5 TRIP 86
5.3.6 Summary 87

CHAPTER 6: COMPARISON OF RESISTANCE AND FRICTION STIR SPOT WELDING 88

6.1 Resistance Spot Welding 88
6.2 Friction Stir Spot Welding 89
6.3 Tensile Shear Testing 92
6.4 Microstructure and Hardness 94
6.5 Fracture Analysis and Mechanical Properties 96
6.6 Additional Factors 98
6.7 Summary 100

CHAPTER 7: CONCLUSION 101

7.1 Microstructure 101
7.2 Mechanical Properties 102
7.3 Failure Analysis 102
7.4 Resistance and Friction Stir Spot Welding 103

APPENDIX A 105

REFERENCES 109

List of Figures

Figure 1.1: Schematic of RSW Process 2

Figure 1.2 : Elongation and strength relationship for various steels [1] 3

Figure 2.1: Electrical resistance during RSW 6

Figure 2.2: Material resistance Vs temperature [8] 7

Figure 2.3: Relative resistance during RSW 8

Figure 2.4: Cross-section of welded HDG Zn-Coated Sheet Steel 9

Figure 2.5: Cross-section of welded uncoated sheet steel 9

Figure 2.6: A schematic of a weldability lobe diagram 10

Figure 2.7: A schematic of a weldability lobe for AHSS, HSLA and mild steel 11

Figure 2.8: Common electrode geometries [15] 14

Figure 2.9: Iron carbon binary phase diagram 15

Figure 2.10: CCT diagram for mild steel 16

Figure 2.11: Peak temperatures of weld regions [8] 19

Figure 2.12: HSLA base metal microstructure 20

Figure 2.13: DP base metal microstructure [1] 21

Figure 2.14: 590R base metal microstructure 22

Figure 2.15: TRIP base metal microstructure 23

Figure 2.16 : Schematic of the FSSW process 23

Figure 2.17: Hardness distribution across DP spot welds 26

Figure 2.18: Weld metal microstructure of RSW DP780 and DP980 [46] 26

Figure 2.19: Cross-section of different failure modes during cross tension testing of a) TRIP 800 and b) DP800 [47] 27

Figure 2.20: Modified welding scheme for TRIP800 [47] 28

Figure 2.21: Button pull-out failure mode for TRIP800 [47] 28

Figure 2.22: Weld diameter and failure load relative to current [48] 29

Figure 2.23: Microstructure of DP20 weld metal [48] 30

Figure 2.24: Dendrites in solidification voids [48] 30

Figure 2.25: Failure loads Vs loading rate for bare and galvanized HSLA 31

Figure 2.26: Absorbed energy as a function of test temperature for various loading rates [50] 32

Figure 2.27: Peak load as a function of loading rate at 23 ^{o}C [50] 33

Figure 3.1: Centerline AC RSW apparatus 35

Figure 3.2: Data acquisition system set-up for resistance spot welding 36

Figure 3.3: Typical DAQ output for a single pulse weld 37

Figure 3.4: StirSpot welding apparatus 38

Figure 3.5: Typical FSSW DAQ output 39

Figure 3.6: Standard 0.9mm – 1.29mm thick sheet steel test coupon dimension [14] 41

Figure 3.7: Tensile shear test 43

Figure 3.8: Schematic of falling weight test 44

Figure 3.9: Coach-peel testing 45

Figure 4.1: Representative weld lobe data for DP600 48

Figure 4.2: Mechanical Properties of weldment 50

Figure 4.3: Microstructure for HSLA 52

Figure 4.4: Microstructure for 590R 53

Figure 4.5: Microstructure of DP600 Weld 54

Figure 4.6: Microstructure for DP780 spot weld 56

Figure 4.7: Microstructure for TRIP780 spot weld 57

Figure 4.8: Hardness mapping of HSLA RSW weld 59

Figure 4.9: Hardness mapping for 590R RSW weld 59

Figure 4.10: Hardness mapping of DP600 RSW weld 60

Figure 4.11: Hardness Mapping for DP780 RSW weld 60

Figure 4.12: Hardness Mapping of TRIP780 RSW weld 61

Figure 4.13: Carbon Equivalence Vs Vickers Hardness 64

Figure 4.14: Fusion zone hardness Vs P_{cm} and CE(IIW) 66

Figure 4.15: CE vs Hv 67

Figure 4.16: XRD results for BM, IC HAZ and FZ of TRIP spot weld 69

Figure 5.1: Fracture surface for coach peel testing of weldments produced using optimal welding conditions. 72

Figure 5.2: Fracture surface for tensile shear testing of weldments produced using optimal welding conditions 73

Figure 5.3: Failure Load Vs Energy Input for RSW AHSS 75

Figure 5.4: Hardness Trace from BM to FZ for DP780, DP600 and 590R 76

Figure 5.5: Representative load-displacement curve for DP600 77

Figure 5.6: Elongation Vs Test Velocity 78

Figure 5.7: Energy Vs Test Velocity 79

Figure 5.8: Failure Load Vs Test Velocity 80

Figure 5.9: Fracture Surface of HSLA 81

Figure 5.10: Fracture surface for 590R 82

Figure 5.11: Load-displacement curve for 590R 83

Figure 5.12: Fracture surface for DP600 84

Figure 5.13: Fracture surface for DP780 85

Figure 5.14: Fracture surface of TRIP 780 87

Figure 6.1: Microstructure for different weld sites in FSSW 90

Figure 6.2: Microhardness maps of FSSW cross-section 91

Figure 6.3: Partial tensile of RSW cross-section 93

Figure 6.4: Partial tensile of FSSW cross-section 93
Figure 6.5: Weld and fracture surface for RSW and FSSW welds 94
Figure 6.6: Failure load Vs total energy 96
Figure 6.7: Failure load Vs bonded area 97
Figure 6.8: Bonded area Vs energy 98

List of Tables

Table 3-1: Material Properties.....40

Table 3-2: Equipment and test velocity.....43

Table 4-1: Optimal welding parameters.....49

Table 5-1: Summary of Fracture Modes.....71

CHAPTER 1: INTRODUCTION

Advanced high strength steel (AHSS) sheet has been introduced into auto body closures and suspension components resulting in a recent focus on the weldability of these alloys [1]. Resistance spot welding (RSW) is the primary sheet metal joining process in the manufacture of automotive assemblies. The microstructure of AHSS results in mechanical properties that are ideal for automotive applications with a high strength to weight ratio and good ductility; however, microstructural changes during RSW dramatically affect mechanical properties by transforming the base metal microstructure. To date, the microstructures and failure mechanisms of resistance spot welded AHSS have not been examined in sufficient detail. This is essential to the integration of AHSS sheet material in today's automobiles. For example, interfacial fracture, which is believed to have detrimental effects on the crashworthiness of vehicles, is a common occurrence when resistance spot welding AHSS [2].

1.1 Resistance Spot Welding

During the RSW process two continuously cooled electrodes clamp down on two or more worksheets as shown in Figure 1.1. AC or DC current is then passed through the electrodes at low voltage which results in fusion at the faying surface of the worksheets. Each welding schedule typically involves five sequential steps [3]: 1) the initial squeeze where the electrode clamps the material. 2) an intensification force at which welding occurs 3) The application of current which results in fusion 4) a hold time to allow for solidification of molten metal and finally 5) electrode release.

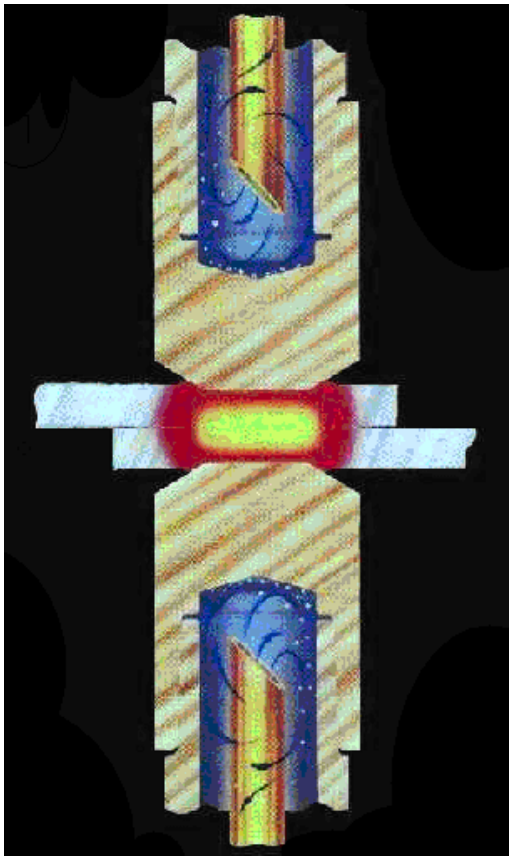

Figure 1.1: Schematic of RSW Process

The heat generated during the RSW process due to interface contact resistance and bulk resistance is given by the following equation:

$$Q = kI^2Rt \qquad 1.1$$

Where *Q* is the total heat, k is a calibration constant, *I* the weld current, *R* the total circuit resistance, and *t* the weld time. From this equation it can be shown that the current, resistance and time are key parameters for heat generation and hence the quality of the weld. Furthermore the contact resistance is dependent on the magnitude of force applied, which can decrease with increased force.

1.2 Advanced High Strength Steel

In recent years, automotive manufacturers have successfully introduced high strength steels (HSS) into the automobile architecture, resulting in improved occupant safety through better crash performance. There is a current drive to increase the percentage of higher strength-to-weight-ratio materials to reduce auto body weight, and thus reduce energy consumption and emissions. Integration of advanced high strength steels (AHSS) for structural components can help accomplish this objective. AHSS materials exhibit high ultimate tensile strengths, compared to conventional HSS, typically exceeding 600 MPa. However as shown in Figure 1.1 there is a reduction in elongation with increasing strength, which can reduce impact performance of these steels.

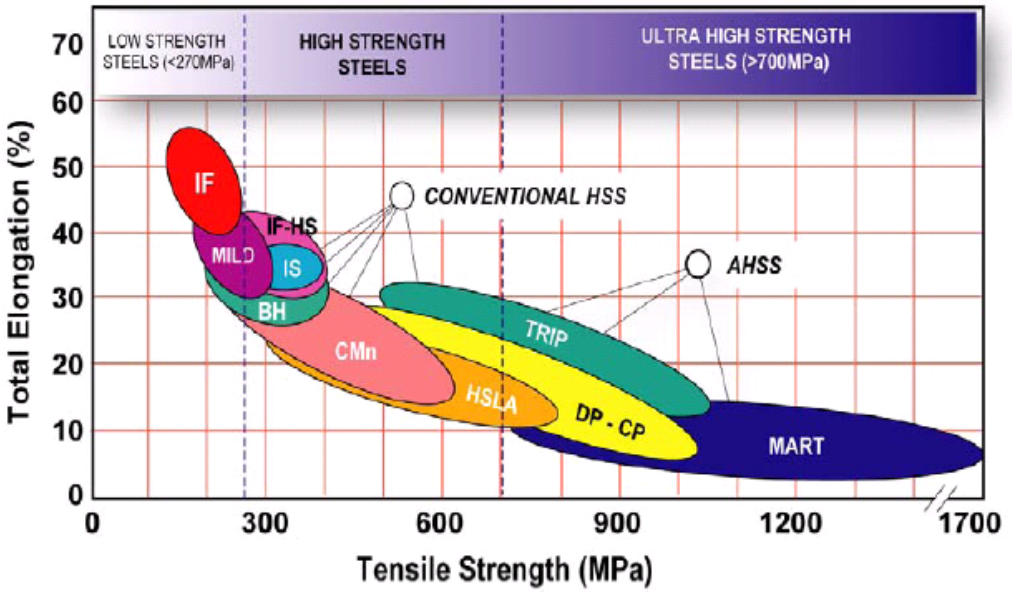

Figure 1.2 : Elongation and strength relationship for various steels [1]

One of the challenges faced with the integration of AHSS as a substitute for HSS include the lack of knowledge on the weldability of these alloys [1]. The base metal microstructure of AHSS results in mechanical properties that are ideal for automotive applications with high strength and good ductility; however,

microstructural changes during welding can dramatically affect mechanical properties by transforming base metal microstructures. Resistance spot welding is the primary sheet metal welding process in the manufacture of automotive assemblies. The mechanical and metallurgical changes in AHSS after the RSW process are documented in the literature [4,5,6]; however, much work is left to be done to improve the quality and attain optimal mechanical properties. For example, excessive hardening or softening in the weldments of certain AHSS can result in decreased strength or toughness of the joint [7]. Improving weld performance is essential to the further integration of AHSS sheet in future automobiles.

1.3 Justification and Problem

Current literature does not compare the effects of RSW on the different types of AHSS available. Furthermore, the metallurgical response to thermal cycles is yet to be detailed. Understanding the weldability of AHSS is required for the integration into the automotive architecture. However, more work is required in order to understand the effects of RSW on these materials before further implementation can occur.

1.4 Objective

The objective of this thesis is to study the RSW of AHSS by examining the process, structure and properties of sheet steel material used in the automotive industry. Specific objectives include

1) Characterization of spot welded AHSS microstructure
2) Comparison of mechanical properties, including strength and impact performance.
3) Analysis of failure modes and fracture paths of spot welds
4) Comparison of RSW of DP600 to the friction stir spot welding process

1.5 Criteria and Constrains

RSW is a relatively mature welding process which is widely implemented in automotive production. Numerous standards exist, which detail procedures for spot welding AHSS. In this study, North American standards governed by the American Welding Society (AWS) are used as criteria for testing spot welded AHSS [14]. This includes sample size and testing procedures for optimising weld parameters. These are detailed in Chapter 3.

Various combinations of materials and electrodes can be spot welded using the RSW process. This study is limited to five materials, which include four AHSS and an HSLA for comparison purposes. Material thickness is restricted to 1.0 mm-1.2 mm and electrode sizes were selected following the AWS standards.

1.6 Thesis Outline

In this thesis Chapter 2 details the resistance welding process and presents a literature review on subjects relating to RSW and AHSS. Chapter 3 introduces the experimental set-up and conditions for welding and performance testing. In Chapter 4, the microstructure and mechanical properties of various resistance spot welded AHSS are examined, including HSLA, 590R, DP600, DP780 and TRIP780. Static and impact performance of these weldments are detailed in Chapter 5. In Chapter 6 a comparative study of RSW and friction stir spot welding of DP600 is investigated. Finally Chapter 6 summarizes key results attained form this work and proposes future work.

CHAPTER 2: LITERATURE REVIEW

2.1 Resistance Spot Welding of Coated and Uncoated Steel Alloys

Electrical resistance in a two sheet stack-up is shown in Figure 2.1. Resistance generated during RSW can be attributed to the contact resistance at the electrode-sheet interfaces (R2) and sheet faying surface (R1) and bulk resistance of the material (R3) [8]. Contact resistance is strongly influenced by temperature and pressure while bulk resistance changes with only temperature.

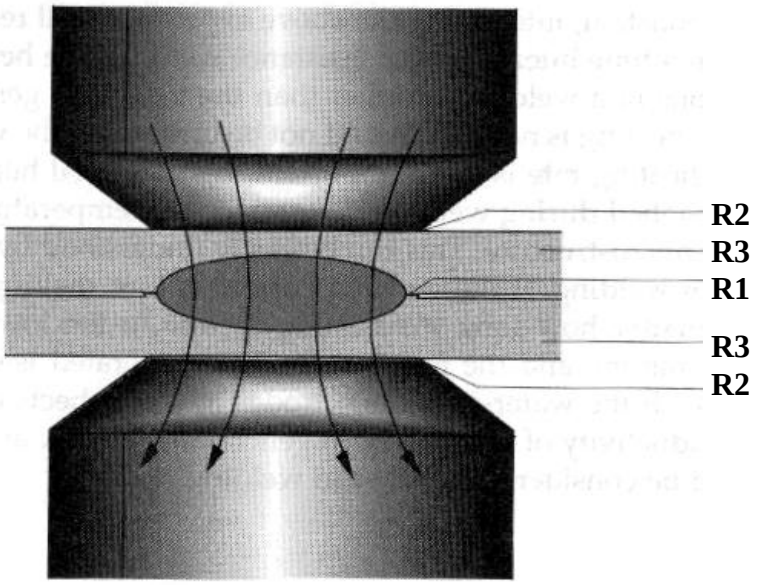

Figure 2.1: Electrical resistance during RSW

Figure 2.2 shows the relationship between bulk electrical resistance and temperature for steel, copper and aluminum alloys. All three materials exhibit an increase in resistivity with increasing temperature. In particular, the steel experiences a larger increase in resistivity at elevated temperatures while copper remains significantly lower [9]. During welding the material is heated due to the

combination of contact and bulk resistance, which is greater in the steel sheet compared to the copper electrodes.

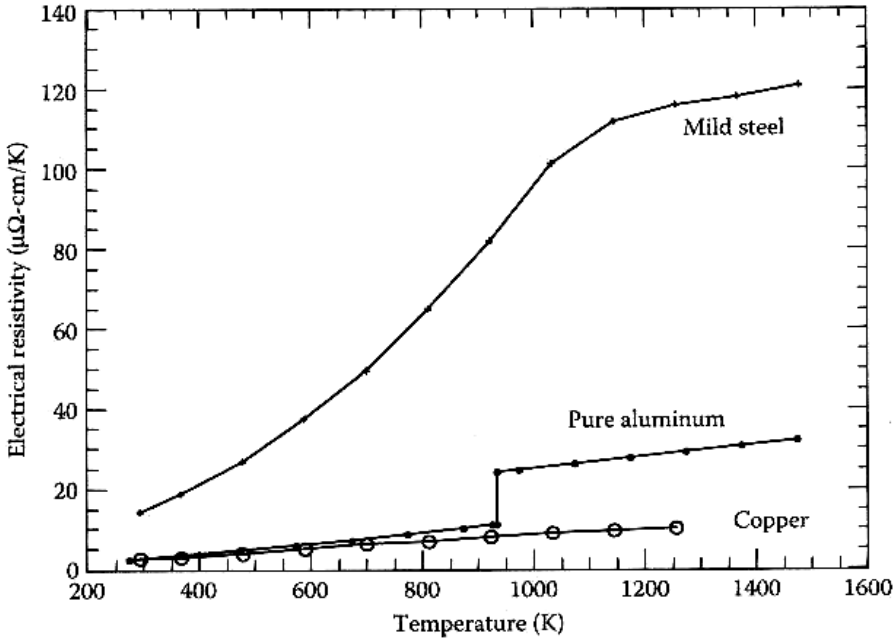

Figure 2.2: Material resistance Vs temperature [8]

Figure 2.3 a) and b) shows the relative resistance and temperatures during RSW of a two sheet metal stack-up for uncoated and Zn-coated steel, respectively. Maximum resistance is experienced at the faying surface (R1) of the material being welded. As formulated in Equation 1.1, heat generation increases with increased resistance. Melting occurs at the interface where generated heat causes peak temperatures to exceed liquidus forming the fusion zone and subsequently joining the material. The dynamic nature of resistance during welding further increases localized heating at the interface. Furthermore, the relatively lower resistance of Zn-coating causes a decrease in relative resistance and an increase in peak temperatures. This in turn can affect the weldability and electrode degradation during RSW, which is detailed in later sections of this chapter [10,11].

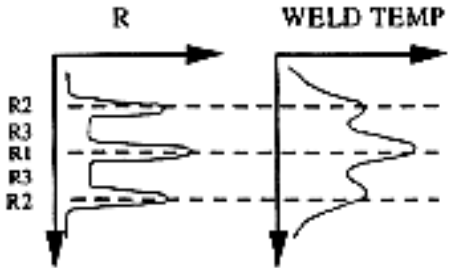

a) Uncoated

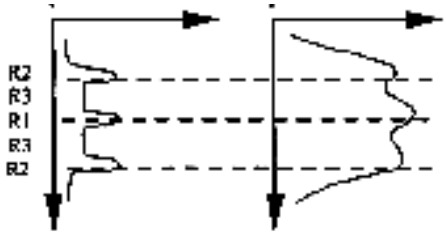

b) Coated

Figure 2.3: Relative resistance during RSW

2.2 Nugget Formation

During the RSW process, resistance at the faying surface generates heat which can cause peak temperatures to exceed liquidus. Studies have shown that the zinc coating on coated steels melts at the faying surface and is pushed to the periphery of the contact area [12]. This in turn causes annular shunting and localized heating as shown in Figure 2.4. With increased time the annulus grows to form a spheroid shaped fusion zone. Figure 2.5 shows the un-coated steel which does not exhibit the annular melting and instead shows localized heating that facilitates nugget formation at the centre of the faying surface.

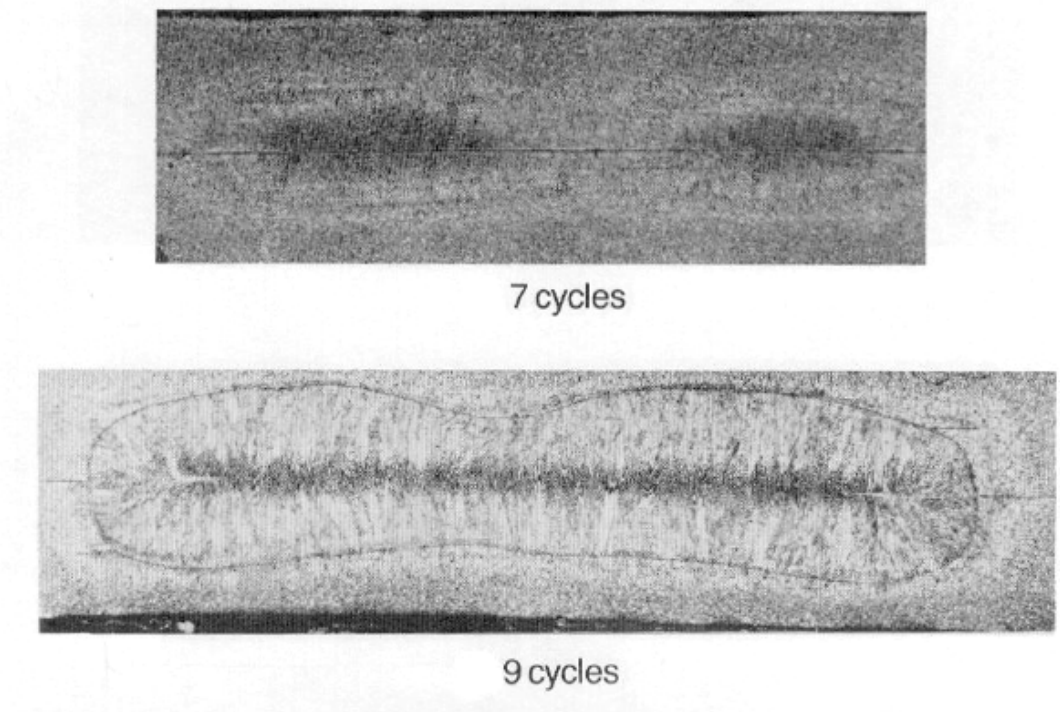

Figure 2.4: Cross-section of welded HDG Zn-Coated Sheet Steel

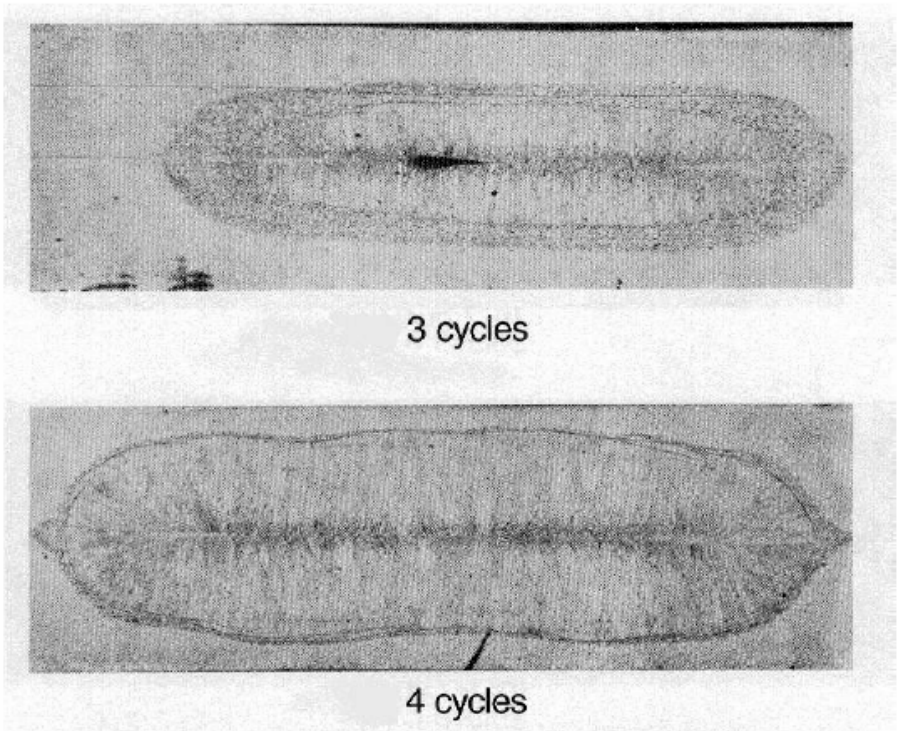

Figure 2.5: Cross-section of welded uncoated sheet steel

2.3 Weldability

Weldability in RSW is a measure of how effectively a particular worksheet can be welded using specific electrodes and materials. This can aid in determining the welding window, which encompasses the acceptable range of welding parameters for a specific material. Studying weldability includes a performance evaluation of weldments in order to determine upper and lower bounds of the welding window. The upper bound is typically defined by expulsion during welding. Excessive heat generation during welding can lead to the expulsion of molten material which in turn can degrade weld performance. North American standards typically define the lower limits by the minimum nugget diameter of $4\sqrt{t}$ where t is the material thickness [14].

Weldability lobes are typically used to determine the upper and lower limits of weld performance. RSW parameters include the welding force, current and time. The width of a weld lobe is a measure of the welding window which can produce acceptable welds. Figure 2.6 shows a schematic of a weldability lobe diagram. This diagram can aid in assessing the current range and time which can yield acceptable nuggets, also known as the welding window.

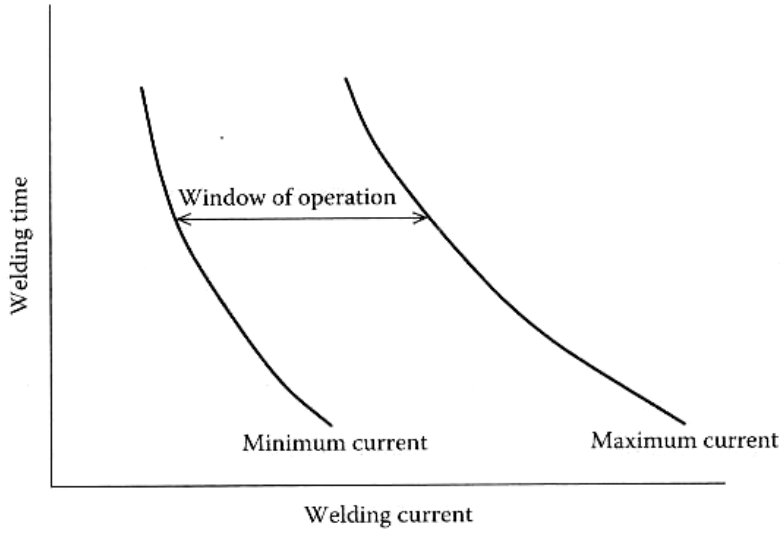

Figure 2.6: A schematic of a weldability lobe diagram

It is more desirable to have materials which have larger weld lobes since deviations from the designated currents will not significantly affect the weld quality. Quantification comparison can be conducted on the weldability of different steel alloys by examining the weld lobe. Figure 2.7 shows a schematic of the weldability lobe diagram for HSLA, AHSS and mild steel. In particular the required current to weld each steel can be compared in Figure 2.7. AHSS requires a relatively lower current range while the leaner chemistry HSLA and mild steel demanded the higher currents. Differences in resistivity due to richer chemistries found in AHSS can result in a reduction of the required currents for welding [13]. Also shown is the relatively narrow welding window for AHSS compared to HSLA and mild steel. Hence, AHSS has a reduced weldability window when compared to HSLA.

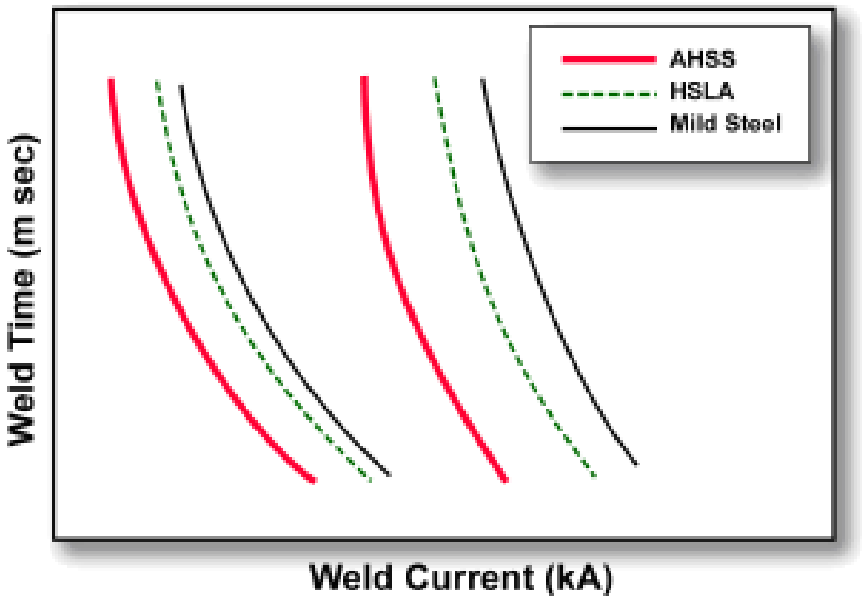

Figure 2.7: A schematic of a weldability lobe for AHSS, HSLA and mild steel

2.4 Welding Parameters

Key welding parameters for RSW are welding current, weld force, welding time and post weld hold time. Other factors that can also influence welds include conduction angles and electrode shape and size. Welding parameters for sheet steel RSW has been studied in great detail and has resulted in the

standardization for particular material thicknesses. These standards were derived for conventional high strength steels and are constituted by the “Recommended Practices for Evaluating the Resistance Spot Welding Behavior of Automotive Sheet Steel Materials” and the “Resistance Welding Manual” [14,15].The three main parameters which require detailed experimental testing include weld current weld time, and weld force and these are detailed in the following sections.

2.4.1 Weld current

Welding current is essential for heat generation. Both AC and DC welding processes can be used to provide high current densities which subsequently generate the heat required for fusion. Hofman et al. showed that both types of current provide similar weld qualities; however, the DC system can reduce electrical demands when welding AHSS, making DC RSW more efficient [16].

Current profiles for RSW can be altered with the addition of up slopes, down slopes and pulsing. Tawade et al. showed that the addition of up sloping can aid in increasing the window in the welding lobe for AHSS [45]. Khan et al. showed use of pulsing for in-situ tempering of the weldments [17]. It was shown that the mechanical performance of weldments could be altered with the addition of weld pulses, which resulted in hardening or softening of the final weld microstructure.

2.4.2 Weld Time

Welding time is directly proportional to the amount of heat being generated. Increased welding time results in increased heat generation. For AC welding supplies the unit time measurements is in cycles with 60 cycles/second for the typical 60Hz North American machine. Weld time for DC power supplies is measured in milliseconds.

Weld time is normally set depending on the material thickness and coating conditions. The interaction of zinc coating at the interface can require increased welding time. Dickenson et al. showed a 50%-100% increase in time was required to weld zinc coated steel [18]. Increased time allows for the molten zinc

to be displaced from the weld area; furthermore, it facilitates nugget growth which enhances the mechanical performance of weldments. However, excessive welding time results in expulsion due to nugget overgrowth. This can introducing weld defects into the weldment, such as voids and excessive indentation, which adversely affect weld performance.

2.4.3 Weld Force

Most RSW processes utilize two distinct welding forces, an initial squeeze followed by an increase to the full welding force. The initial squeeze is required to avoid impacting of the electrodes and aid in material alignment [15]. This is followed by the application of a full force which can be experimentally determined or selected from recommended handbook values [14,15].

The welding force can influence the contact resistance of a material. Higher welding forces typically results in better interfacial contact and reduced resistance. This can result in lower heat generated during welding, which needs to be compensated with increase weld time or higher current inputs [8]. In addition, excessive welding force can cause excessive indentation in the work piece.

2.5 Electrodes and Electrode Degradation

The function of alloyed copper RSW electrodes include applying force to the work piece, providing necessary current densities and facilitating post-weld cooling. Typical electrode geometries are shown in Figure 2.8. Truncated electrodes are commonly used in industrial applications due their limited contact tip growth. However care must be taken during alignment of truncated electrodes since the weld quality can be severely affected with misalignment. Dome type electrodes are less susceptible to misalignment issues and are also commonly employed for industrial applications.

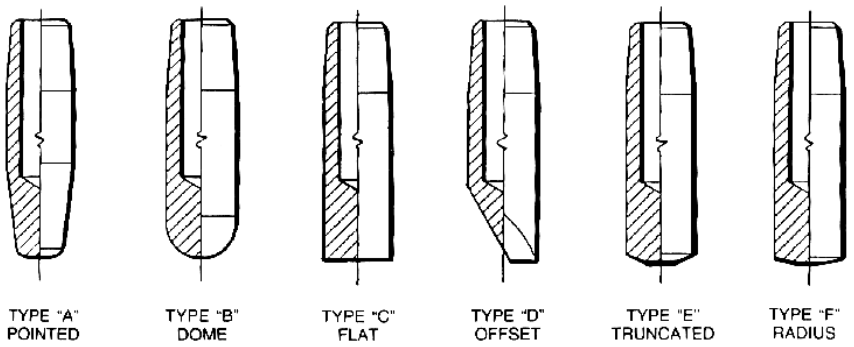

Figure 2.8: Common electrode geometries [15]

Electrode degradation can result in welds with insufficient fusion or irregular nugget formation. During degradation the electrode contact area increases and reaches a size where adequate current densities can not be attained. Ultimately this results in poor quality welds. Hence it is important to maximize electrode life to consistently achieve acceptable welds.

In order to enhance corrosion resistance, automotive steels are typically zinc coated. The addition of coatings can alter the resistance profile at the interface of an RSW stack-up. Figure 2.3 b) shows the modified resistance and temperature profile with the addition of Zn coating. Increased temperatures aid in melting and vaporization of the Zn-coatings. This in turn can aid inter-diffusion of copper and zinc which results in the formation of alloys. Furthermore, increased peak temperatures at the electrode-sheet interface have shown to accelerate electrode degradation during welding [19,20].

2.6 Phase Transformations

2.6.1 Fe-C Phase Diagram

The Fe-C phase diagram in Figure 2.9 shows a range below the eutectoid composition of steel (0.77 wt% C) which is typically found in automotive steel alloys [21]. When peak temperatures surpass A_3 a fully austenitized structure is created and subsequently cooled. With slow cooling the austenite volume fraction decreases as regions of soft BCC ferrite nucleate and grow containing

small amounts of dissolved carbon within the structure. At the eutectoid temperature (723^{o}C) remaining austenite transforms into pearlite producing a eutectoid structure consisting of ferrite and cementite. Higher cooling rates can bring the transformation temperature below those marked on the phase diagram [22].

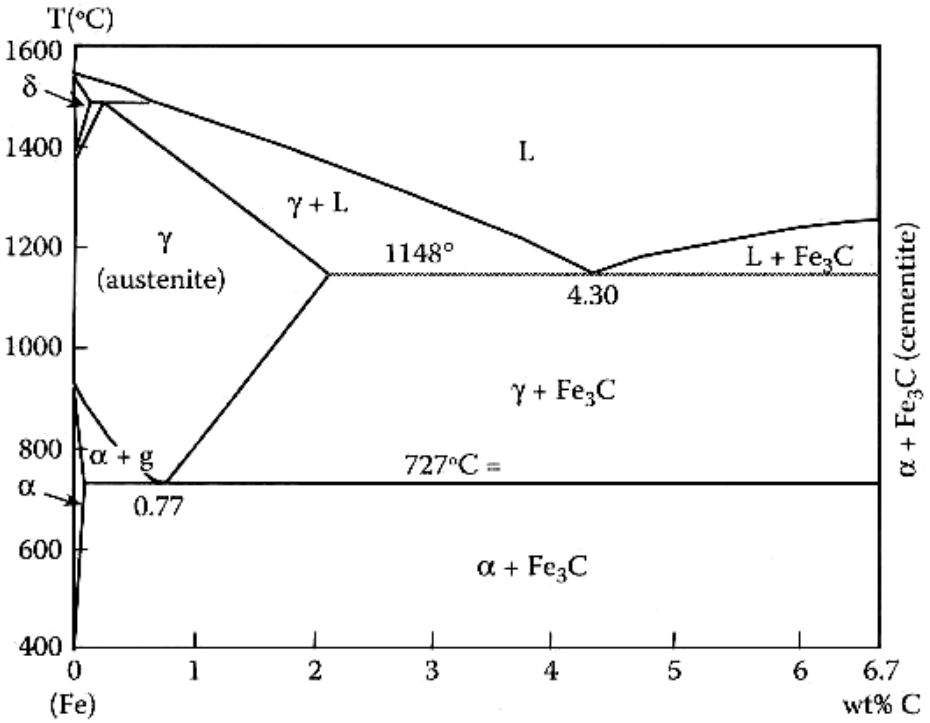

Figure 2.9: Iron carbon binary phase diagram [23]

Significantly higher cooling rates typically experienced during RSW can alter transformation temperatures from those predicted from the equilibrium phase diagram. Depending on the cooling rate and alloy composition, morphology of phases can alter and form bainite, pearlite or martensite. Rapid cooling during RSW depresses transformation temperatures found on phase diagrams. At lower temperatures this can result in high nucleation combined with reduced growth forming a finer structure. At elevated peak temperatures fully austenitized regions typically transform into martensite. However the binary phase diagram can aid in understanding phase transformations occurring in typical automotive steels.

2.6.2 Time-Temperature Transformation Diagrams

Transformation diagrams are important tools which aid in understand the types of microstructures produced during cooling. Since the majority of industrial heat treatments undergo controlled cooling methods rather than isothermal transformations, continuous cooling transformation (CCT) diagrams are more applicable than time-temperature transformation (TTT) diagrams. CCT and TTT diagrams are similar except CCT diagrams encompass a wide range of transformation temperatures while TTT diagrams detail isothermal transformations. A typical CCT diagram for mild steel is shown in Figure 2.10. Slow cooling rates results in a mixture of ferrite and pearlite. Intermediate cooling has a tendency to produce a ferrite, bainite and martensite mixture. Finally, rapid cooling results in the instantaneous and diffusionless transformation of martensite.

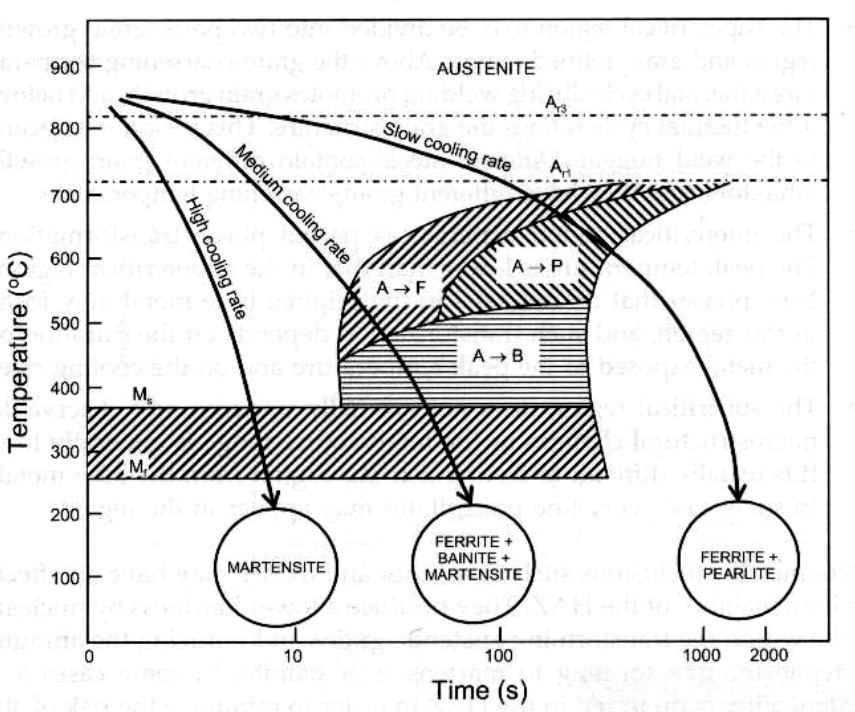

Figure 2.10: CCT diagram for mild steel

Various alloying elements in steel can alter the pearlite nose position in the CCT diagram. Elements such as titanium, tungsten and molybdenum are known ferrite

stabilizers and aid in lowering the eutectoid carbon content and raise transformation temperatures. In CCT diagrams these elements raise the pearlite nose and move it to the left, which results in increased time and temperature for pearlite transformations to occur. Other elements, such as nickel and manganese, lower eutectoid carbon content and transformation temperature. These elements, also known as austenite stabilizers, affect the CCT diagram by lowering the pearlite nose and pushing it to the right. Most elements increase the hardenability of steels by moving the CCT curve to the right, allowing martensite to form at lower cooling rates.

2.6.3 Carbon Equivalence

The carbon equivalence (CE) value of transformable steels is an index measure which predicts a materials susceptibility to post-weld cold cracking in the HAZ. The susceptibility of cold cracking is directly related to the amount of martensite within the HAZ. Alloying elements can aid in the formation of martensite by increasing required transformation times and hence the CE provides an index measure of the effects that alloying elements have on the formation of martensite.

Multiple CE equations are available in literature [24,25,26,27,29] each taking into account numerous alloying elements, which include ferrite and austenite stabilizers. Available equations include the CE (IIW) [28] and P_{cm} developed by Ito et al. [29] which are expressed in Equation 2.1 and 2.2, respectively:

$$CE(IIW) = C + \frac{Mn}{6} + \frac{Cu + Ni}{15} + \frac{Cr + Mo + V}{5} \qquad 2.1$$

$$P_{cm} = C + \frac{Si}{30} + \frac{Mn}{20} + \frac{Cu}{20} + \frac{Ni}{60} + \frac{Cr}{20} + \frac{Mo}{15} + \frac{V}{10} + 5B \qquad 2.2$$

Studies have shown the CE(IIW) to better suit higher carbon steels with greater then 0.16% carbon [30]. P_{cm} on the other hand is more appropriate for low-carbon low-alloy steel [31]. However, the wide range of carbon contents found in AHSS can not be accommodated using one simple equation.

Yurioka et al. used various test methods to determine preheating temperatures required to avoid cold cracking during welding [32]. In particular, the Stout slot weld tests were carried out on 20 different steels [33]. The steels had various structural applications with each containing various amount of alloying elements. From this work the following equation was proposed:

$$CE_Y = C + A(C)\cdot\left\{5B + \frac{Si}{24} + \frac{Mn}{6} + \frac{Cu}{15} + \frac{Ni}{20} + \frac{Cr + Mo + Nb + V}{5}\right\} \qquad 2.3$$

Where CE_Y is the Yurioka carbon equivalence and A(C) = 0.75 + 0.25tanh {20(C-0.12)}. Equation 2.3 contains an accommodation factor, A(C) which approaches 0.5 when carbon is below 0.08% and increases to 1.0 with carbon contents above 0.18%. The A(C) factor eliminates the use of two CE equations and allows for CE_Y to be applicable for steels alloys with carbon contents ranging between 0.02 and 0.2. Furthermore this single equation can accommodate the unique chemistries of most AHSS.

2.7 RSW Characterization

Figure 2.11 shows the relationship between peak temperature during gas metal arc welding (GMAW) and the Fe-C binary phase diagram. Similar peak temperatures and weld regions are attained during the RSW process. A typical fusion weld is composed of the fusion zone (FZ) and heat affected zone (HAZ). Temperatures in the FZ exceed liquidus temperatures, which results in molten material.

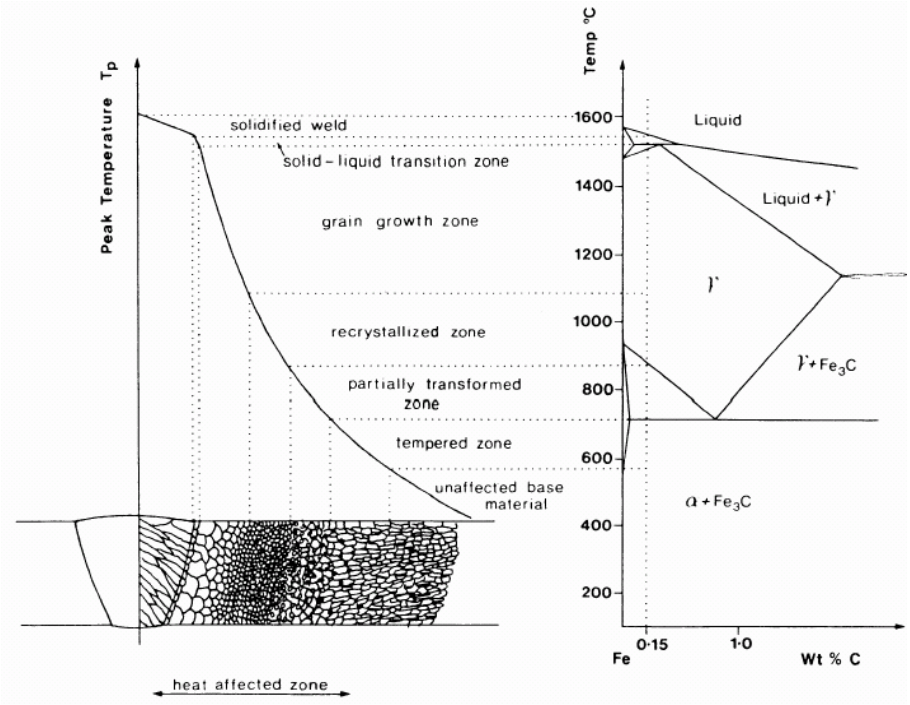

Figure 2.11: Peak temperatures of weld regions [8]

The HAZ undergoes transformations caused by peak temperatures surpassing eutectoid temperatures. As a result the BM microstructure is altered. The HAZ can be subdivided in to three main regions which include the coarse grain (CG), fine grain (FG) and intercritical (IC) HAZ. Peak temperatures in CG HAZ are well above Ac_3, transforming BM microstructure into austenite. The FG HAZ experiences temperatures slightly surpassing Ac_3 which results in fine recrystallized grains. Finally, the IC HAZ consists of a partially transformed microstructure caused by peak temperatures ranging between Ac_1 and Ac_3.

2.8 HSS and AHSS

2.8.1 High Strength Low Alloy

High strength low alloy (HSLA) sheet steel has been effectively integrated into the automotive architecture. Typical HSLA production consists of a laminar cooling stage where the nucleation and growth of ferrite is facilitated and carbides form at the boundaries. Figure 2.12 shows the typical HSLA

microstructure consisting of ferrite grains with carbide particles situated at the grain boundaries. A combination of strength, toughness and weldability accelerated the implementation of HSLA for automotive applications. Hence, effects during welding HSLA steel alloys have been extensively studies [34,35,36 37].

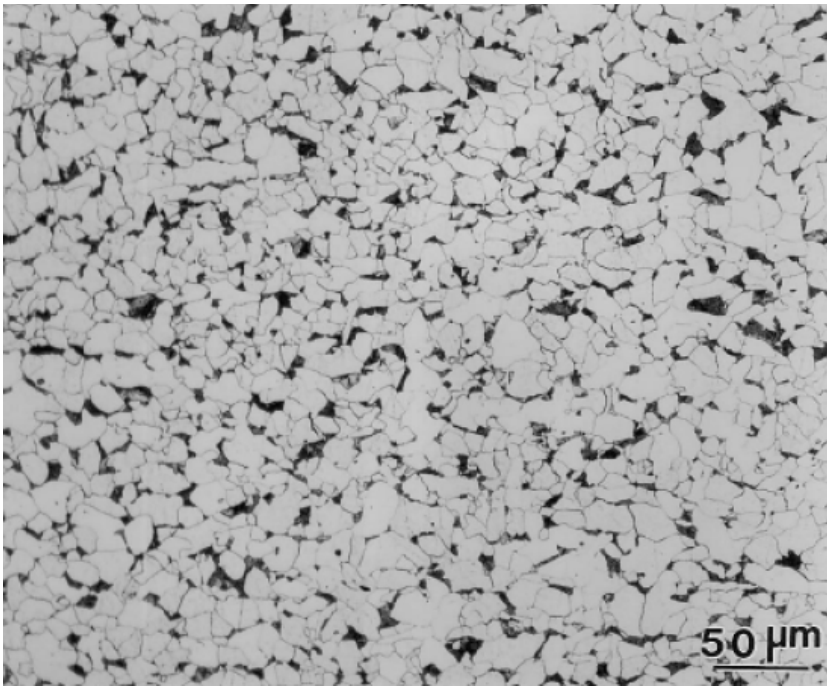

Figure 2.12: HSLA base metal microstructure

2.8.2 Dual Phase

Dual phase (DP) steels exhibit high strength to weight ratios ideal for automotive application. The naming convention of DP steel includes a numerical suffix which pertains to the tensile strength of that particular grade. For example DP600 has a tensile strength of 600MPa. Typical DP microstructure consists of hard martensite islands surrounded with a soft ferrite matrix as shown in Figure 2.13. The strength of DP steels is proportional to the volume fraction of martensite; increased volume fractions have shown to increase the strength of DP steels. Furthermore, improved formability and stretchability of certain DP grades makes them ideal for replacing thicker conventional HSS.

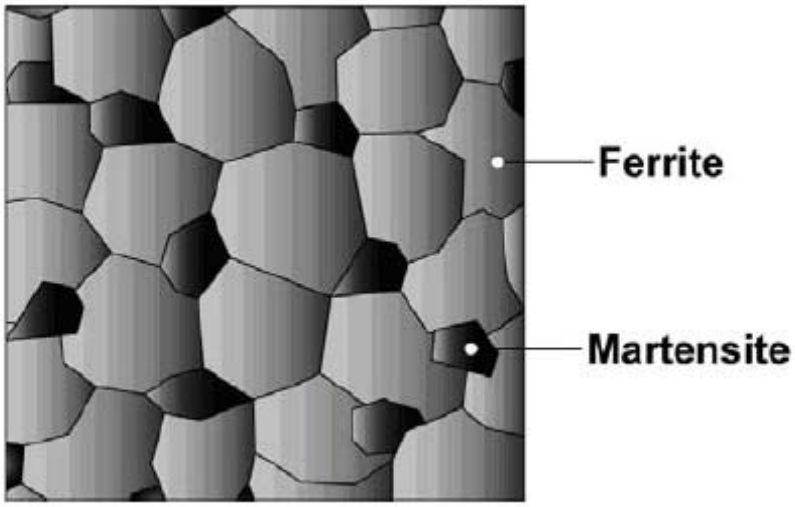

Figure 2.13: DP base metal microstructure [1]

During processing DP steels are hot rolled and intermediately cooled at temperatures below AC_1, allowing ferrite grains to nucleate and grow. This is followed by rapid cooling where the prior austenite grains transform into martensite producing the dual phase microstructure. Since strength is used to distinguish the various grades of DP, chemistries for similar strength DP can vary between steel manufacturers.

2.8.3 Ferrite-Bainite (590R)

Enhanced formability coupled with high strength of spot welds categorizes 590R as an AHSS. Development of this steel was based on achieving a stable weldable alloy with relatively low carbon levels and alloying elements [38]. Studies have shown potential in replacing conventional 440 MPa HSLA with thinner 590R that exhibit maximum energy absorption during impact [38,39]. Figure 2.14 shows the typical microstructure of 590R comprising of a ferrite matrix with bainite grain boundaries. During the processing of 590R hot rolling is used to cool at an intermediate temperature below Ac_1 promoting ferrite nucleation and growth. This is followed with a lower temperature aiding in the formation of bainite at ferrite grain boundaries.

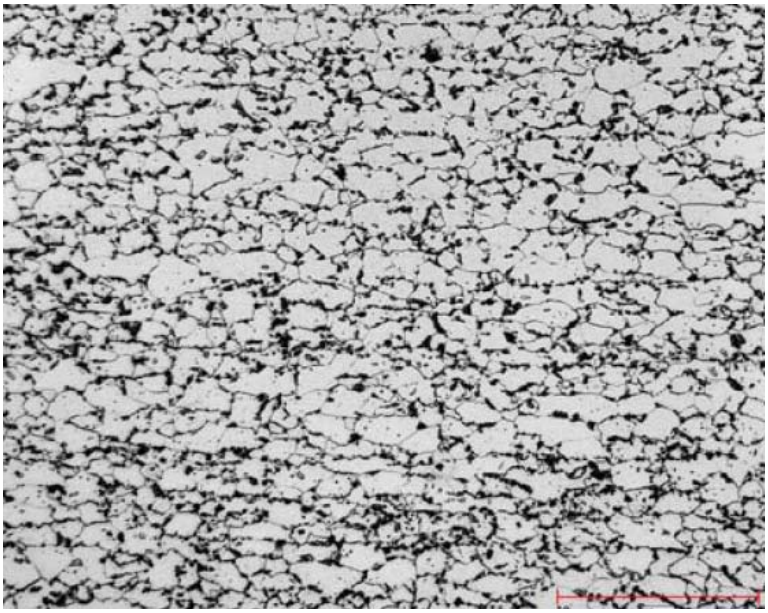

Figure 2.14: 590R base metal microstructure

2.8.4 Transformation Induced Plasticity

High strength combined with excellent formability makes Transformation Induced Plasticity (TRIP) steel ideal for automotive applications. Base metal microstructure, shown in Figure 2.15, consists of metastable retained austenite and dispersed bainite surrounded by a ferrite matrix. Transformation of metastable austenite into martensite during straining improves ductility of TRIP steels. During processing of TRIP steels the complex microstructure is obtained by cooling from an α+γ region to an isothermal holding temperature. Bainite forms as carbon is rejected to austenite bringing the martensite start temperature (Ms) down to below room temperature.

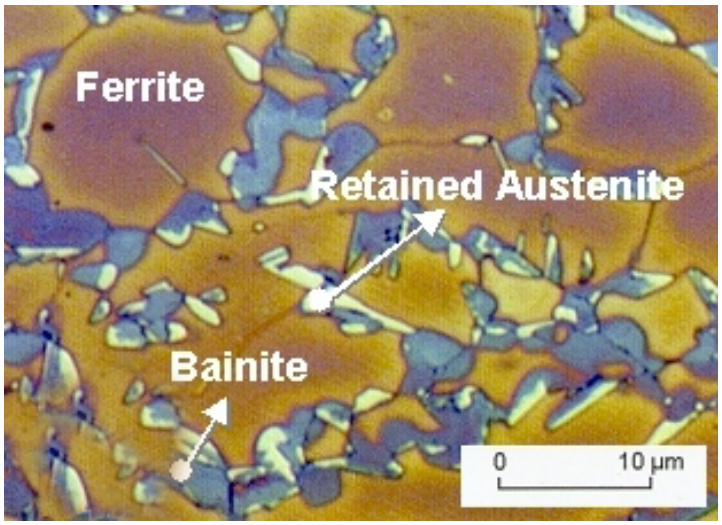

Figure 2.15: TRIP base metal microstructure

2.9 Friction Stir Spot Welding

Friction Stir Spot Welding (FSSW) is a relatively new process which has shown to effectively reduce energy cost when welding aluminium alloys [40]. Figure 2.16 shows schematic of the three main steps involved in the FSSW process. During the FSSW process a rotating pin tool plunges into the upper sheet of a lap joint. Heat generated by the rotating pin softens the surrounding material and facilitate further penetration of the tool. Severe plastic deformation of the surrounding material forms a bond along periphery of the pin. Finally the rotating pin tool is retracted, leaving the characteristic keyhole in the centre.

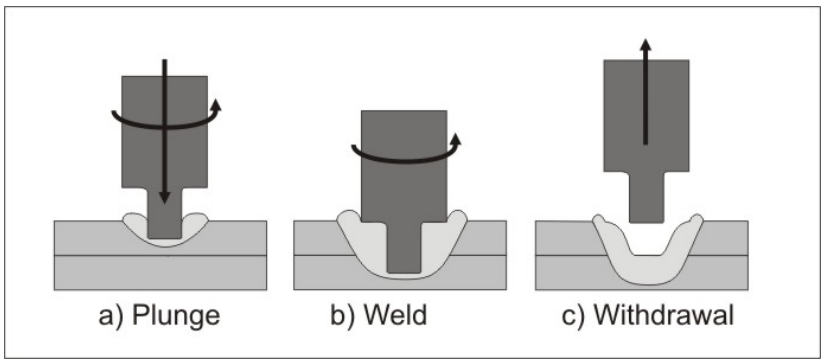

Figure 2.16 : Schematic of the FSSW process [41]

A typical FSSW weldment is composed of three distinct sub-regions. Similar to RSW, the HAZ is only affected by heat generated during welding. The thermo-mechanically affected zone (TMAZ) is located closer to the rotating pin and undergoes mechanical deformation and transformations induced by heat. Finally, the stir zone (SZ) region, located along the periphery of the keyhole, undergoes severe plastic deformation.

The final microstructure of the spot weld determines the mechanical properties and performance for the weldment. Key parameters measured during welding include the pin rotation speed, plunge depth, force, torque and temperature. Variations in each parameter can alter the size and microstructure of the weld region. The tools generally consist of a pin and shoulder component; however, different tool geometries can also modify the microstructure. Hence, detailed analysis of these parameters can aid in understanding the microstructural evolution during FSSW.

2.10 Spot Welding of AHSS

2.10.1 Weldability

Studies conducted on the weldability of AHSS are typically limited to process optimization focusing on maximizing process reliability. Industrial needs include large process windows which allows for reliable welds. Numerous welding parameters can affect the mechanical properties of weldments.

Using a two-dimension and three dimension weldability lobe Weber et al. examined the process reliability of resistance welding of uncoated and hot dip zinc coated high strength TRIP steels as well as complex phase steels [42]. It was concluded that the process reliability and weldability for RSW AHSS can be guaranteed. Furthermore it was shown that strength and fatigue properties of AHSS exceed that of conventional mild steel.

Kim et al. implemented the response surface methodology to determine optimal welding conditions for the weldability of AHSS [43]. Using a second order model, RSW of TRIP steel was investigated using welding current, force and time as input variables, and shear strength and indentation as output variables. Kim et al. showed that the surface method could be used to in determining optimal weld conditions which produced a satisfactory weld quality.

Pogio et al. examined the weldability of similar and dissimilar combinations of DP600 and AISI 304 [44]. It was determined that in both similar and dissimilar welding of DP600 a particular welding range with appropriate welding parameters can produce acceptable welds. Furthermore, he showed better mechanical properties using AHSS compared to conventional high strength steel.

Tawade et al. proposed a modified welding current profile by examining multiple pulsing and up sloping for current initiation [45]. They were able to attain a schedule which included an enhanced pulse developed for welding DP600 to itself and DP600 to the HSLA 350. This modified schedule improved the width of the lobe which can aid automobile assembly plants aiming for robust weld schedules. It was also shown that the removal of zinc on an initial weld pulse with an optimized second current resulted in improved weld lobe. Furthermore it was found that a welding pulse with an up-sloping schedule was not beneficial for welding DP600 to itself.

2.10.2 Mechanical Performance and Microstructure

Tumuluru examined the RSW behaviour of hot-dipped galvanized DP steel with tensile strengths of 590 MPa, 780 MPa and 980 MPa [46]. As shown in Figure 2.17 the hardness for the 590 MPa steel was 380 Hv, which was slightly higher then the 780 MPa and 980MPa. From this data it was deduced that rapid cooling, which results from the RSW process, causes the formation of untempered martensite in the weld metal shown in Figure 2.18. Furthermore he stated that

carbon content of this steel was the main factor which determined the hardness of martensite. Tumuluru concluded that since all three steels contained similar carbon contents they produced similar weld hardness; however, a slight difference can still be noted in the hardness data.

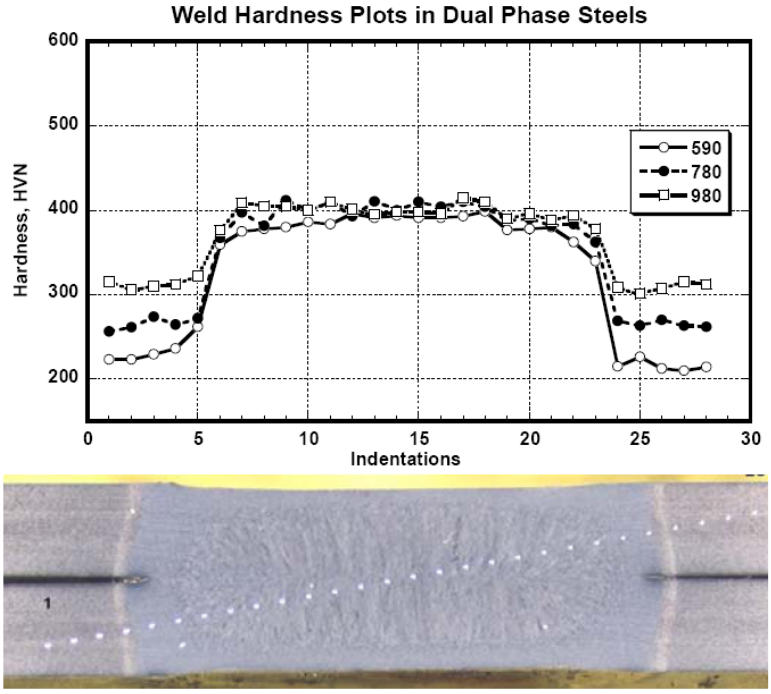

Figure 2.17: Hardness distribution across DP spot welds

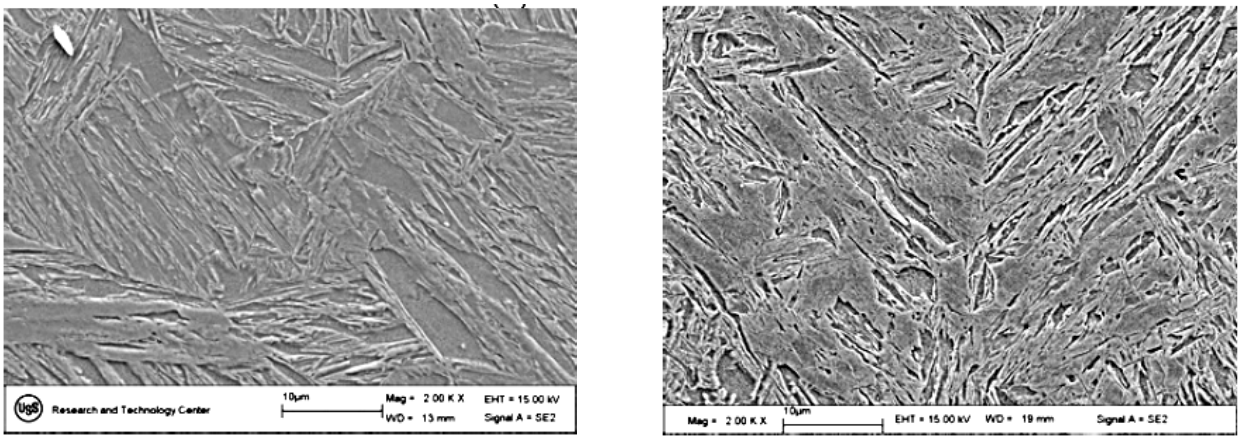

a) 780 MPa b) 980 MPa

Figure 2.18: Weld metal microstructure of RSW DP780 and DP980 [46]

Uijl et al. investigated RSW for TRIP and DP AHSS [47]. Single pulse welds were created using similar strength DP800 and TRIP800 alloys. During tensile testing the TRIP800 consistently produced partial interfacial failure while full button pull-out was observed in the DP780, as shown in Figure 2.19. It was speculated that the high phosphorus content of the TRIP800 resulted in segregation and provided a preferred path for crack propagation along the dendrite boundaries. Furthermore the absence of rich chemistries in the DP800 made it less susceptible to segregation during cooling.

a) TRIP800

b) DP800

Figure 2.19: Cross-section of different failure modes during cross tension testing of a) TRIP 800 and b) DP800 [47]

In order to avoid partial interfacial failure modes, Uijl et al. proposed a modified welding schedule shown schematically in Figure 2.20. The concept behind the modified schedule included a post-weld heat treatments which fully austenitized the weld to dissolve any segregated chemistries. This in turn resulted in the full button failure mode shown in Figure 2.21. However, effects of HAZ tempering on the modified weld schedule were not discussed.

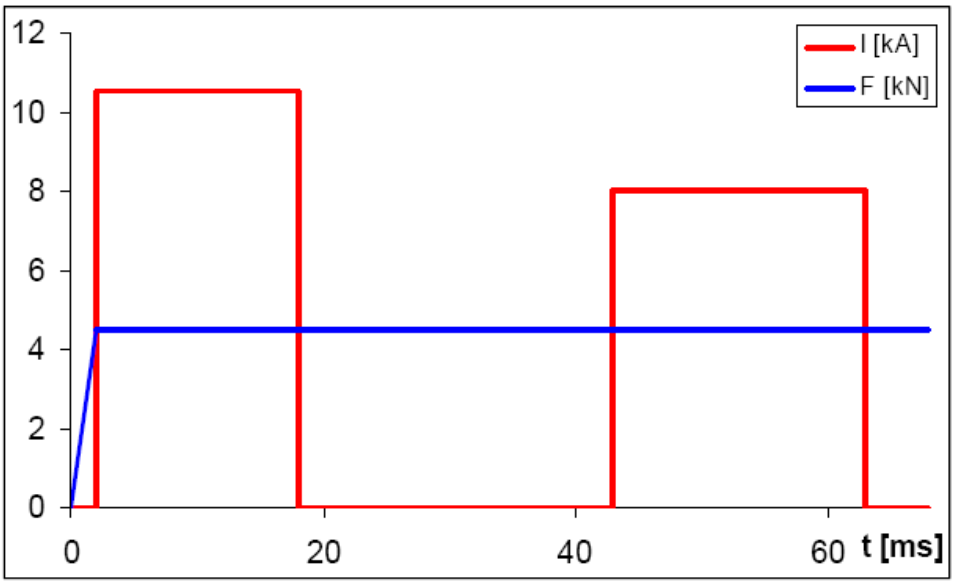

Figure 2.20: Modified welding scheme for TRIP800 [47]

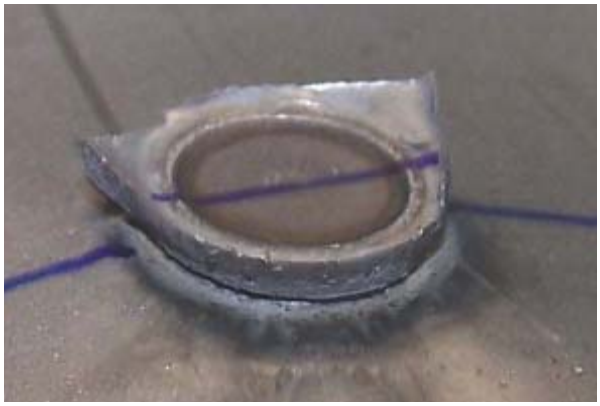

Figure 2.21: Button pull-out failure mode for TRIP800 [47]

Marya et al. investigated the weld fracture in relation to welding parameters for DP600 [48]. They used two grades of DP600 which contained different base metal chemistries including a richer 1.8 mm (DP18) and a lean 2.0 mm (DP20). Figure 2.22 shows the general trend where both materials exhibit an increase in weld diameter and failure load with increasing currents. Interfacial fracture was observed for the lower current levels while at higher currents produced button pull-outs. Causes for changes in failure modes were not detailed.

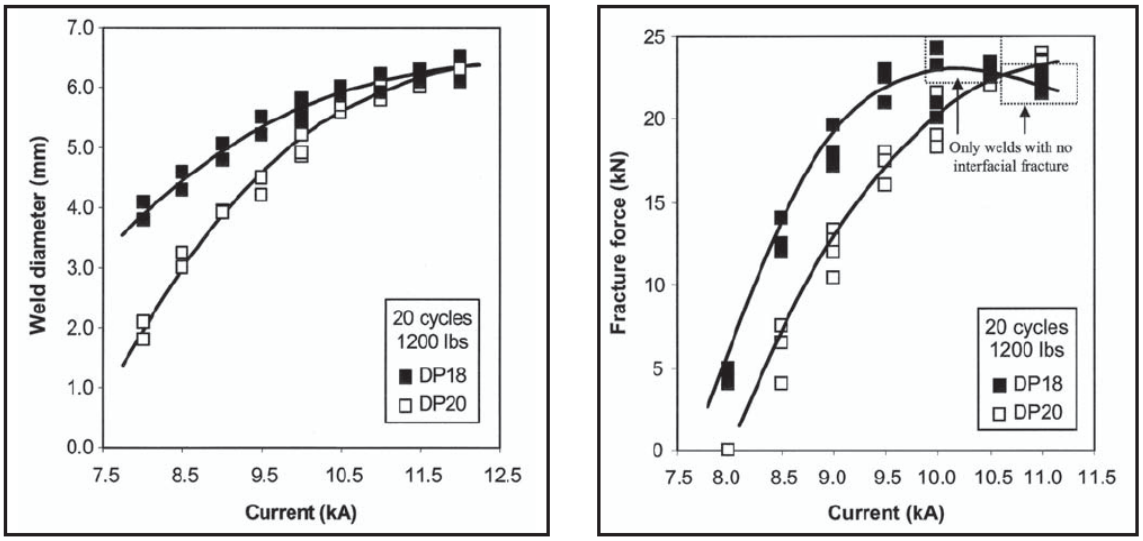

Figure 2.22: Weld diameter and failure load relative to current [48]

Microstructures observed for the DP20 are shown in Figure 2.23. In the outer-HAZ micro-constituents were observed to be considerably finer than in the base metal (Figure 2.23b). Further into the HAZ large aggregates of blocky phases were presumed to be ferrite (Figure 2.23c). In the fusion zone, (Figure 2.23c) small cracks were present within the predominately martensitic matrix. Dendrites shown in Figure 2.24 were located in large voids at the weld centerline. These voids were said to be caused by solidification shrinkage.

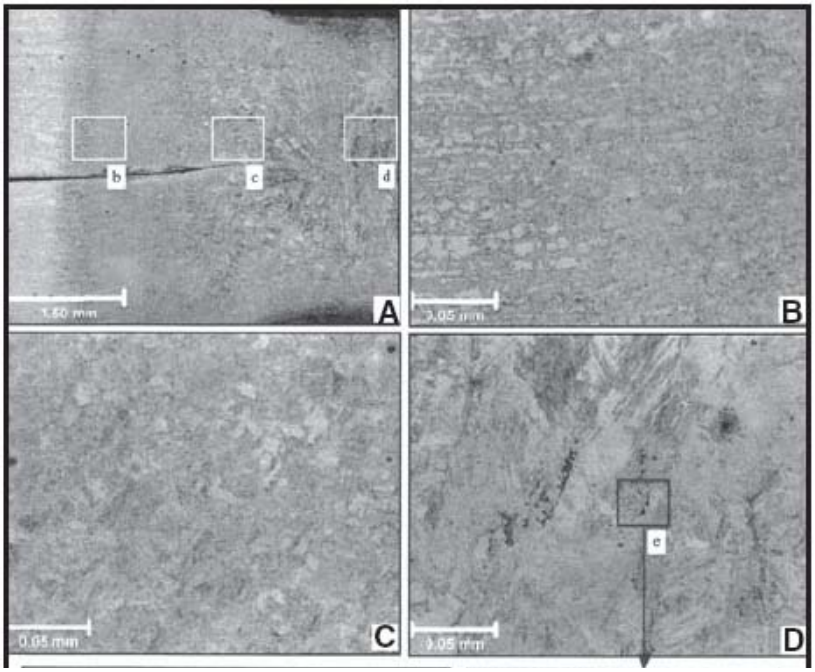

Figure 2.23: Microstructure of DP20 weld metal [48]

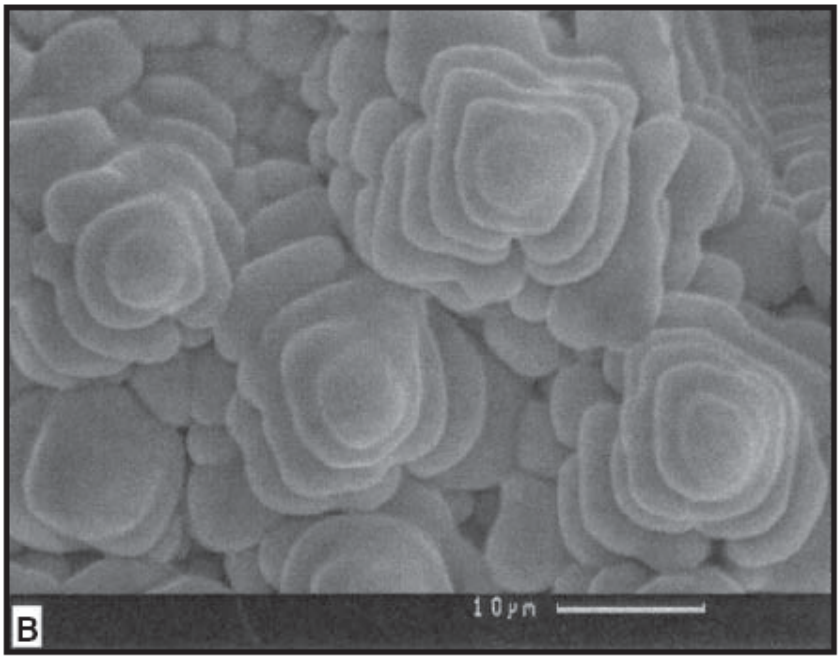

Figure 2.24: Dendrites in solidification voids [48]

2.10.3 Static and Impact testing of RSW AHSS

Understanding the impact performance of spot welded AHSS is critical for the safe integration of these steels into the automotive architecture. Weld failure induced by impact loading rates are common to automotive applications. This section will detail work done on examining the impact performance of HSS and AHSS.

Ewing et al. examined the tensile performance of resistance spot welded galvanised and bare HSLA produced using different welding schedules [49]. Tests were conducted using loading rate between 10^{-4} mph and 15 mph. Figure 2.25 shows the failure loads at the various test velocities for the bare and galvanised HSLA. It was concluded that the maximum loads increased with increasing test velocity for all weld schedules and the failure modes remained constant for all the tests. Finally, it was observed that the galvanizing did not appear to significantly affect the failure loads for the spot welded HSLA specimens.

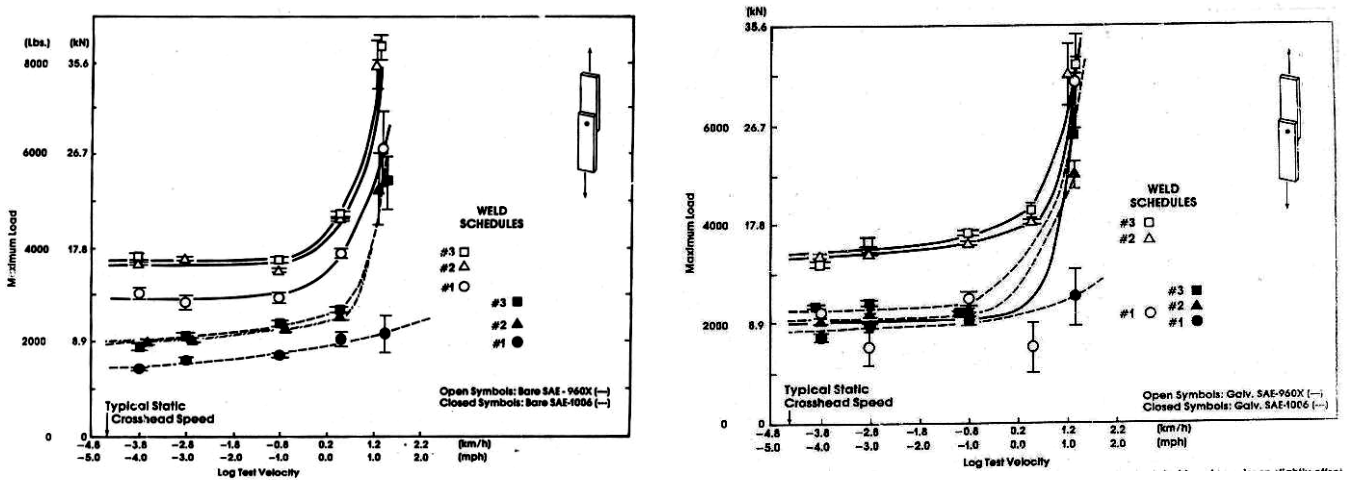

a) Bare HSLA b) Galvanized HSLA

Figure 2.25: Failure loads Vs loading rate for bare and galvanized HSLA

Peterson et al. studied the influence of temperature and test rate for spot welds made on a single grade of 1.8mm DP590 [50]. Test temperatures ranged from -75°C to 400°C and test rates from 0.005 to 500 in/sec.

Figure 2.26 shows the relationship between absorbed energy and test temperature for the various loading rates attained during testing. No distinct transition temperatures were observed for any loading rates. Figure 2.27 shows the peak load as a function of loading rate at 23 °C. A slight increase in peak loads was observed at higher loading rates, however scaling on the graph shows little change in peak loads. It was concluded that the reduction in absorbed energy at high test rates was due to the reduction in material ductility at these rates. No detailed explanation was provided which explained reasons for reduced ductility.

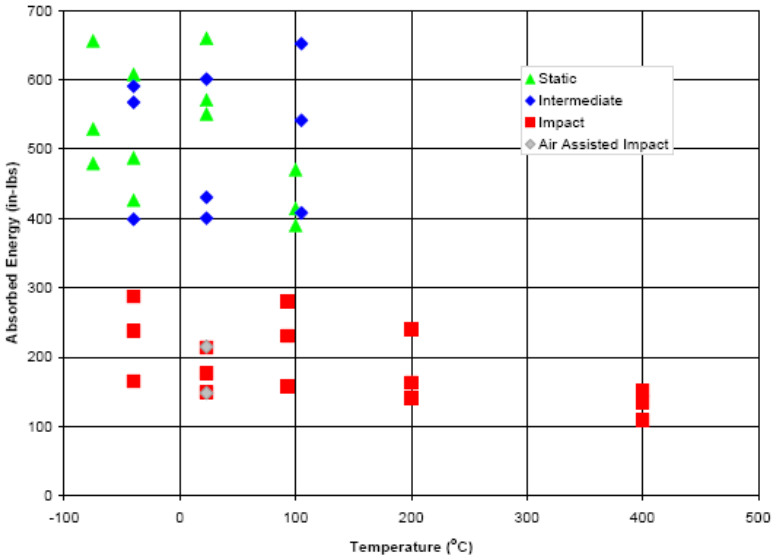

Figure 2.26: Absorbed energy as a function of test temperature for various loading rates [50]

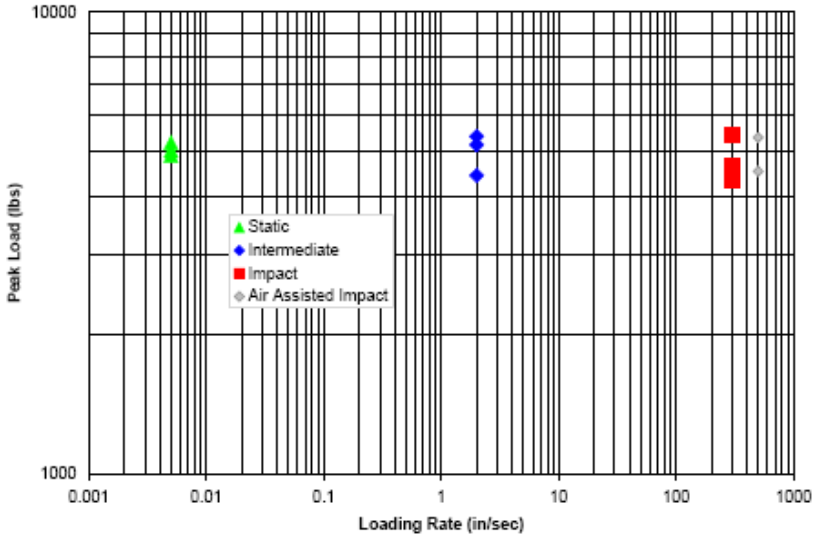

Figure 2.27: Peak load as a function of loading rate at 23 ^{o}C [50]

Currently, there is limited literature on the impact performance of spot welded material. In particular there are no comparative studies which details the impact performance of spot welded HSS and AHSS. Temperature effects have thus far shown little correlation to impact energy absorption and peak loads when testing DP spot welds. Furthermore detailed analysis of fracture paths during loading is yet to be examined.

2.11 Summary

Mechanical properties of AHSS sheet metal promises improved crash performance and reductions in weight for automotive applications. The RSW process provides a quick and effective method for spot welding sheet steel and has been largely adapted in the automotive industry. The various parameters involved in RSW can influence the weldability and mechanical performance of weldments. Some key parameters include:

1) Welding Force
2) Welding Time
3) Welding Current

Much of the literature can explain the effects of zinc coatings, electrode degradation and the weldability of traditional HSS. In depth examination and comparison of RSW AHSS has yet to be conducted.

The majority of studies conducted on AHSS are limited to process optimization. In turn, minimal work has been done to understand the metallurgical aspect of RSW AHSS. This thesis examines the metallurgical and mechanical properties of RSW AHSS. Detailed analysis of microstructure and mechanical performance of welded AHSS is conducted to attain an in depth understanding of phase transformation caused by weld thermal cycles. In addition, the impact performance of spot welded AHSS was evaluated. Finally, a comparative study was done on spot welded DP600 using the FSSW and RSW process.

CHAPTER 3: EXPERIMENTAL METHODS

3.1 Welding Equipment

3.1.1 Resistance Spot Welding Set-up

The RSW samples were produced using a Centerline 250-kVA pneumatically operated single phase RSW machine with constant current control and a frequency of 60 Hz. Figure 3.1 shows the RSW machine equipped with the DAQ system. A truncated class 2 electrode with 6.0 mm face diameter was used as per AWS standards for 0.9 mm to 1.29 mm thick sheet [14]. Electrode stabilization was conducted using endurance coupon procedures, which was conducted for each new set of electrodes. Total number of welds per electrode was monitored to stay below the electrode degradation limits. Cooling water flow rate and hold time also followed AWS recommendations of 4 l/min and 5 cycles, respectively.

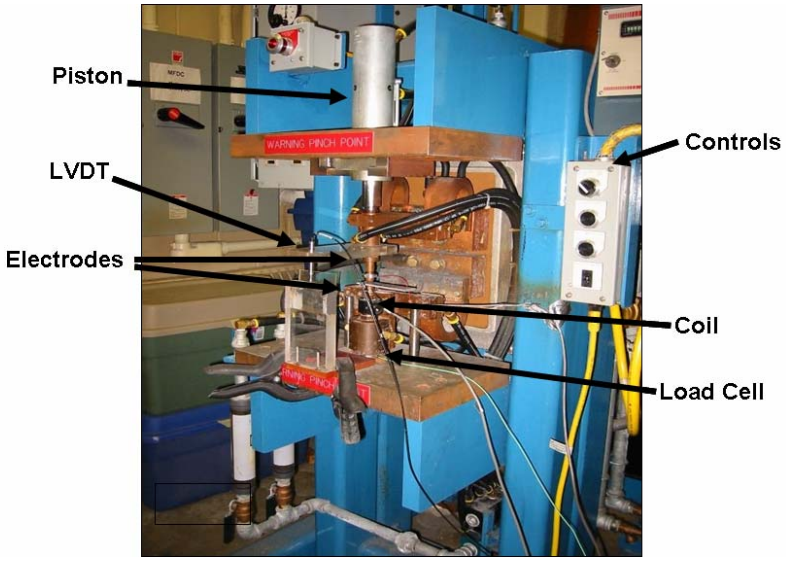

Figure 3.1: Centerline AC RSW apparatus

3.1.2 Data Acquisition System

The RSW machine was fully equipped with a data acquisition (DAQ) system capable of recording load (±0.01 kN), displacement (±0.01 mm), current (±0.1 kA) and voltage (± 0.001 V) simultaneously as a function of time. Figure 3.2 shows a schematic of the DAQ setup on the AC welder. A linear transducer mounted to the top electrode measures the displacement while a calibrated coil collects the dI/dT, which is conditioned to attain current as a function of time. The load cell located under the bottom electrode measures the force applied by the overhead cylinder. The data acquisition rate was 25,000 points per second (pps). Figure 3.3 shows the typical DAQ output for a typical single pulse weld which includes the initial force, welding force, welding time and hold time.

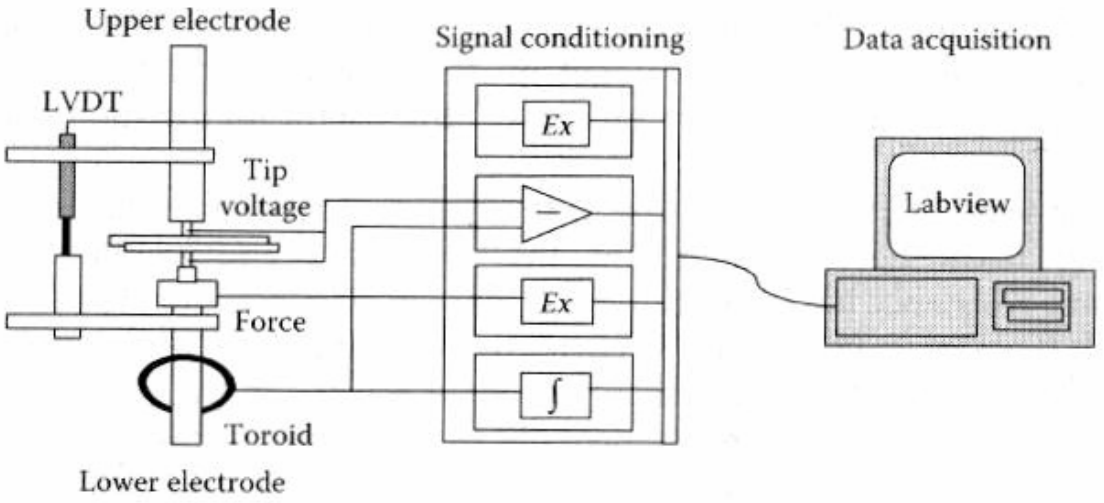

Figure 3.2: Data acquisition system set-up for resistance spot welding

The energy supplied (Q_{RSW}) during RSW is a product of the weld power and time, where the weld power is a product of the measured current (I) and voltage (V). In this work, Q_{RSW} was calculated using Equation 3.1 where $1 \leq n \leq N$ and Δt is the sampling time [51].

$$Q_{RSW} = \sum_{n=1}^{N} |I(n)| \cdot |V(n)| \Delta t \qquad 3.1$$

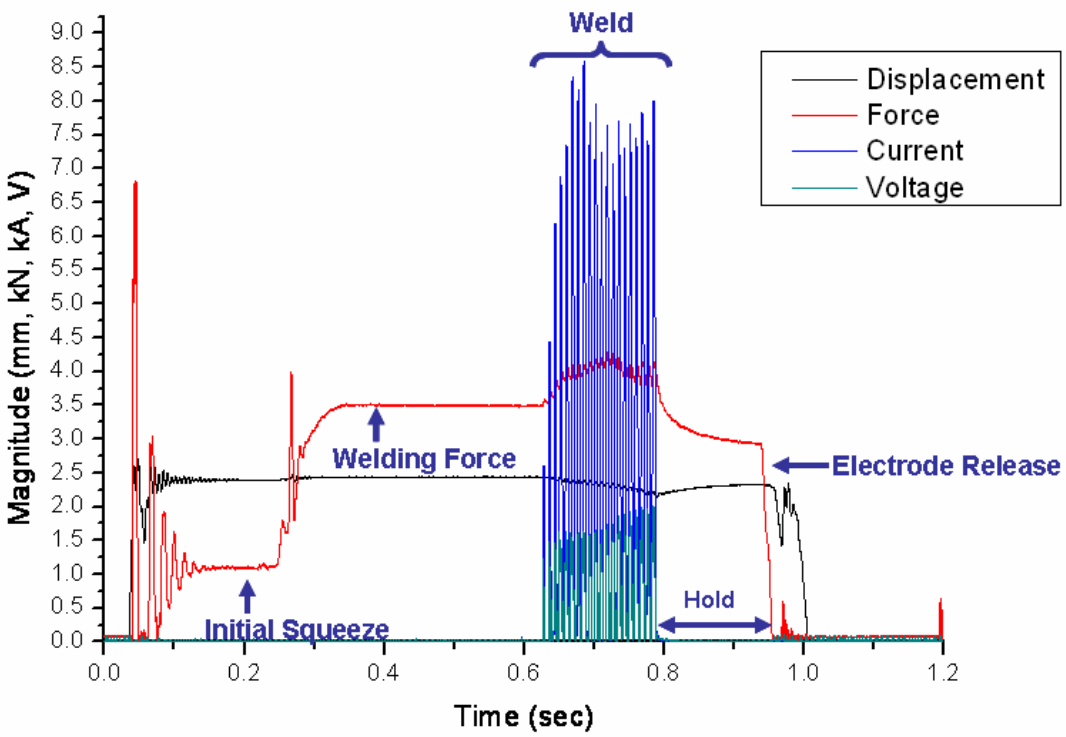

a) Full weld schedule

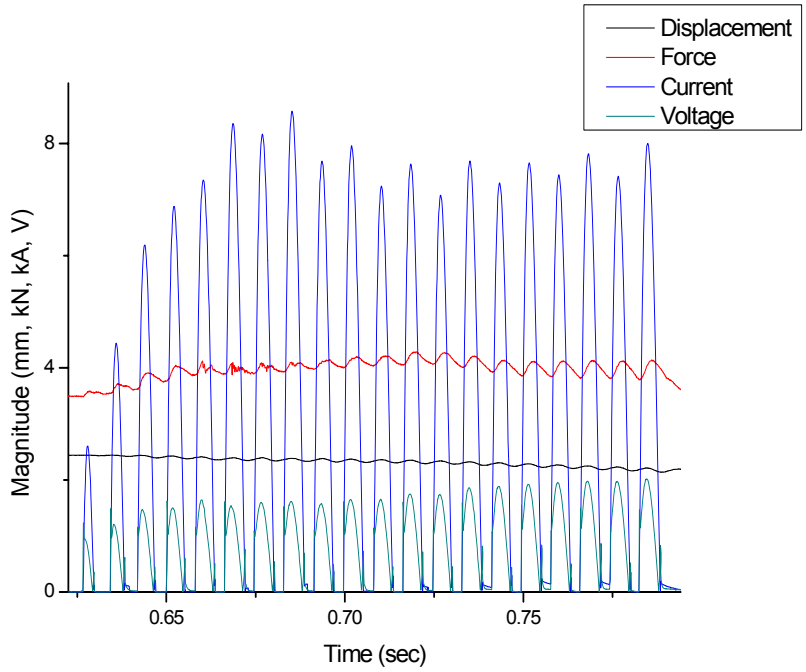

b) During welding

Figure 3.3: Typical DAQ output for a single pulse weld

3.1.3 Friction Stir Spot Welding

As part of this thesis a comparative study between RSW and friction stir spot welding (FSSW) was conducted. FSSW welds were produced using a Friction Stir Link Inc. StirSpot welder shown in Figure 3.4. Capabilities of this particular machine includes tool rotational speed of up to 3000 RPM, an axial load of 14 kN and plunge rates (tool displacement rate) from 0.1 to 25 mm/s. The W - 25 wt. % Re tool used for the spot welds had a truncated cone geometry, a pin diameter of 4 to 5.1 mm, a pin length of 1.7 mm, and a shoulder diameter of 10 mm.

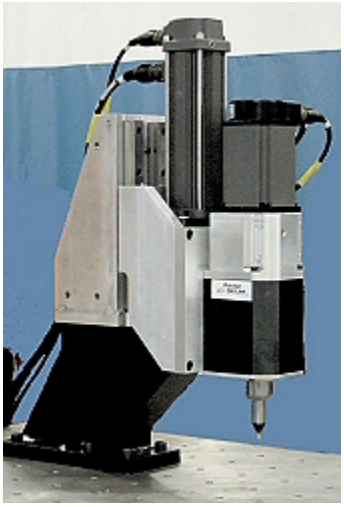

Figure 3.4: StirSpot welding apparatus

Samples were produced for mechanical testing using a range of plunge rate and plunge depth settings. The plunge rates were 0.5 mm/s and 1 mm/s while the plunge depths varied from 1.7 mm to 2.1 mm. In all cases the tool penetration depth was measured using a linear transducer having an accuracy of ±0.01 mm while the spindle RPM was measured using a shaft encoder, which had an accuracy of ±30 RPM. The axial load and the torque values were measured using a six-axis load cell, which was coupled with a data acquisition system so that the axial force, torque and penetration depth values were recorded simultaneously during each spot welding operation. Figure 3.5 shows the typical output produced during friction stir spot welding of the DP600 sheet. For a explanation of the observed changes in axial force and torque during the friction stir spot welding operation the literature should be referenced [52,53].

During linear friction stir welding, where the rotating tool is traversed across the joint, inert gas is required to shield the weld. Experimental results have shown that shielding gas is not required for spot welds where the tool is stationary (i.e. does not traverse parallel to the sheet). There was no difference between welds with and without Ar gas shielding, except for minor oxidation of the keyhole and upper surface of the weld occurring after tool retraction upon completion of the weld. Following this, no gas shielding was used for the samples prepared for metallographic inspection and mechanical testing.

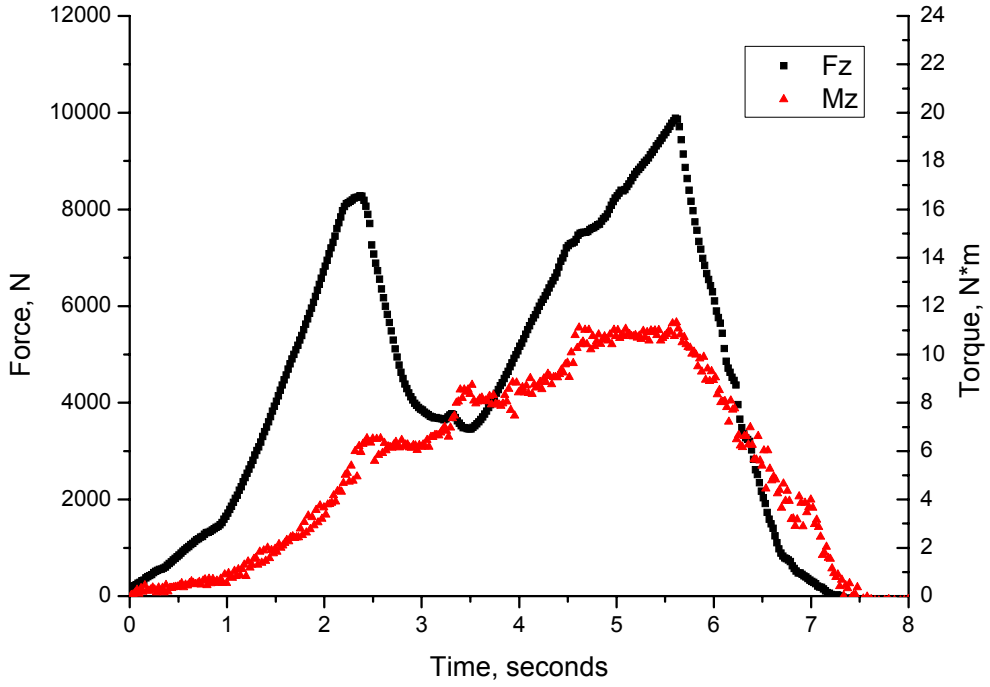

Figure 3.5: Typical FSSW DAQ output

The energy applied during FSW (Q_{FSW}) is the sum of the normal and vertical components. Equation 2 was used along with the experimentally measured normal force (F) and displacement (x); and, the axial torque (T) and angular velocity (Δ) [20]. The sampling time was Δt and $1 \leq n \leq N$.

$$Q_{FSW} = \sum_{n=1}^{N} F(n) \cdot \left(x(n) - x(n-1)\right) + \sum_{n=1}^{N} T(n) \cdot \omega(n) \cdot \Delta t \qquad 3.2$$

3.2 Material Selection

Table 3-1 shows the grade and chemical composition of the materials used in this study. The available material include, two grades of DP: DP600 and DP780; a TRIP steel: TRIP780; a ferrite-bainite steel: 590R. In this particular TRIP steel, Si is the dominant constituent aiding in the formation of bainite, however Al is also a commonly used additive. HSLA material is also included to represent conventional high strength steels and benchmark AHSS performance. Table 3-1 also shows the coating details and Yurioka carbon equivalence.

Table 3-1: Material Properties

Steel Grade	Thickness (mm)	Coating		Alloying elements (wt %)					CE_Y
		Type	Ave. Wt. (g/m^2)	C	Mn	Mo	Cr	Si	
HSLA	1.0	GI	73.9	0.060	0.640	0.010	0.050	0.240	0.139
590R	1.2	GA	43.4	0.130	1.599	0.013	0.029	0.120	0.363
DP600	1.2	HDGI	55.1	0.100	1.523	0.196	0.197	0.157	0.326
DP780	1.15	GA	58.8	0.113	2.082	0.181	0.239	0.036	0.427
TRIP800	1.0	HDGI	62.5	0.188	1.631	0.012	0.023	1.618	0.527

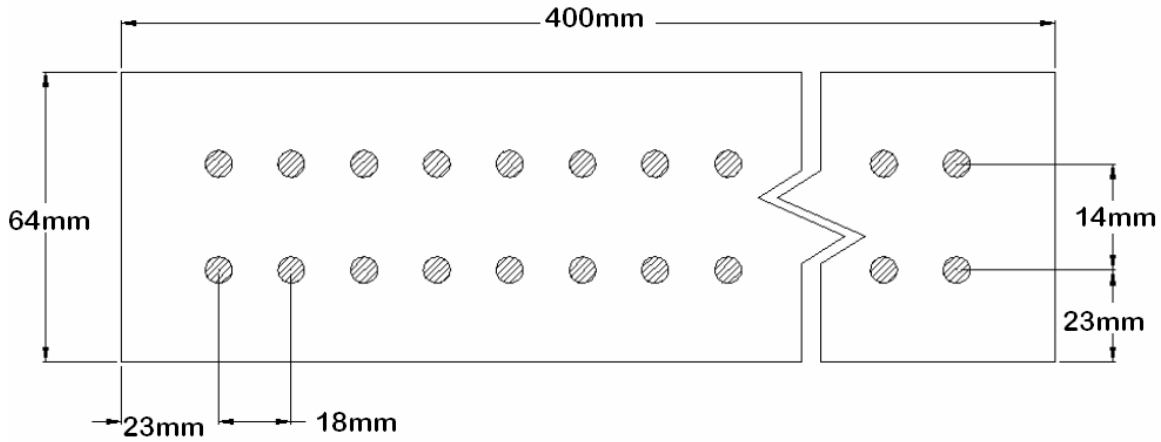

a) Endurance test coupon

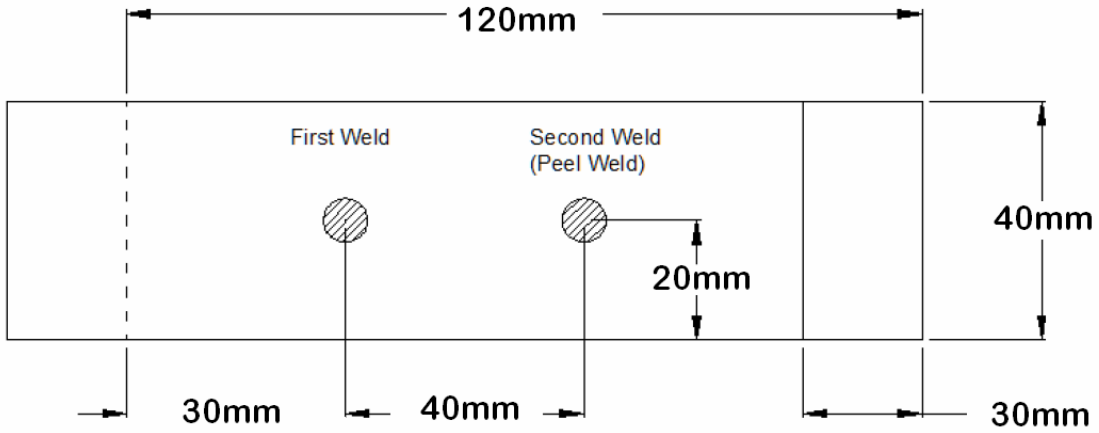

b) Peel Test coupon

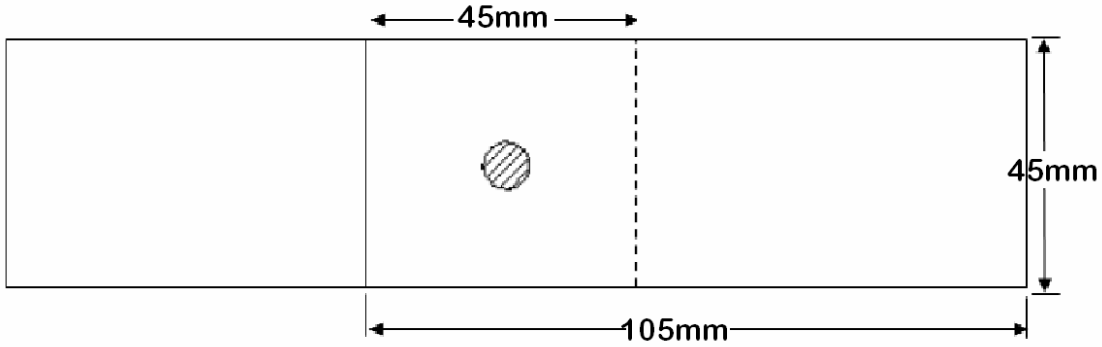

c) Tensile shear test coupon

Figure 3.6: Standard 0.9mm – 1.29mm thick sheet steel test coupon dimension [14]

3.2.1 Specimen Dimensions

Material thickness ranged between 1.0 mm-1.2 mm as shown in Table 3-1. Test coupons were cut as per guidelines specified for this range of thickness in the "Recommended Practices for Test Methods for Evaluating the Resistance Spot Welding Behavior of Automotive Sheet Steel Materials" (ANSI/AWS/SAE/D8.9-97) [14]. All of the steel sheets were of the same batch for their respective thickness. Details of the coupon dimensions for tensile, peel and endurance testing are shown in Figure 3.6 [14].

3.3 Mechanical Testing

3.3.1 Tensile Shear Testing

Joint mechanical properties were evaluated by measuring the peak load to failure during overlap tensile shear testing. Care was taken to maintain co-planar alignment during mechanical testing. The fracture surfaces of broken overlapped shear test specimens were examined using SEM fractography. Detailed examination of failure mechanism was also facilitated by interrupting the loading cycle during overlap shear testing, i.e., by halting the tensile testing machine when the welded section had only partially failed. This technique allowed detailed examination of the nature of failure propagation during failure of particular joints. Finally, the projected cross-sectional area of the bonded region was measured by digital image analysis.

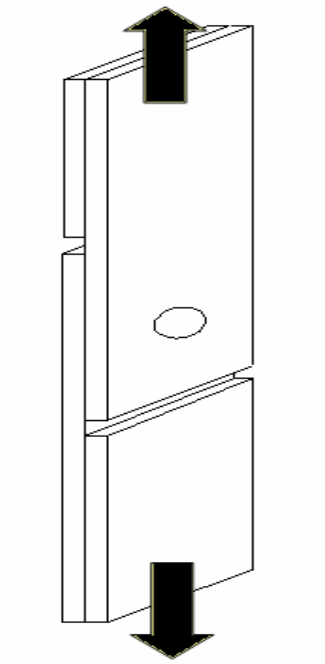

Figure 3.7: Tensile shear test

3.4 Impact Testing

Three test rates were selected for overlap shear testing which included quasi-static, intermediate and impact test velocities, see Table 3-2. Static and intermediate test rates were performed using a standard Instron #4411 universal testing machine machine. Care was taken to maintain co-planar alignment during mechanical testing by using shims in the grips. Detailed examination of failure mechanism was facilitated by monitoring load-displacement outputs and interrupting the loading cycle during overlap shear testing at static strain rates.

Table 3-2: Equipment and test velocity

Equipment	Test Type	Test Velocity
Instron	Static	8.3×10^{-7} m/s
	Intermediate	1.7×10^{-3} m/s
Drop Tower	Impact	5.36 m/s

For Impact testing, an instrumented falling weight impact tester (IFWI) was used. The IFIW tester is capable of compression, biaxial tension, toughness and uniaxial tension testing. A schematic diagram showing testing set-up is shown in Figure 3.8. Fixturing allows for a coplanar geometry to be maintained without the use of shims. A load cell located above the upper grip monitors the force while a magnetic displacement sensors measure relative displacement. Interpretation of the load-displacement data is detailed in Chapter 5.

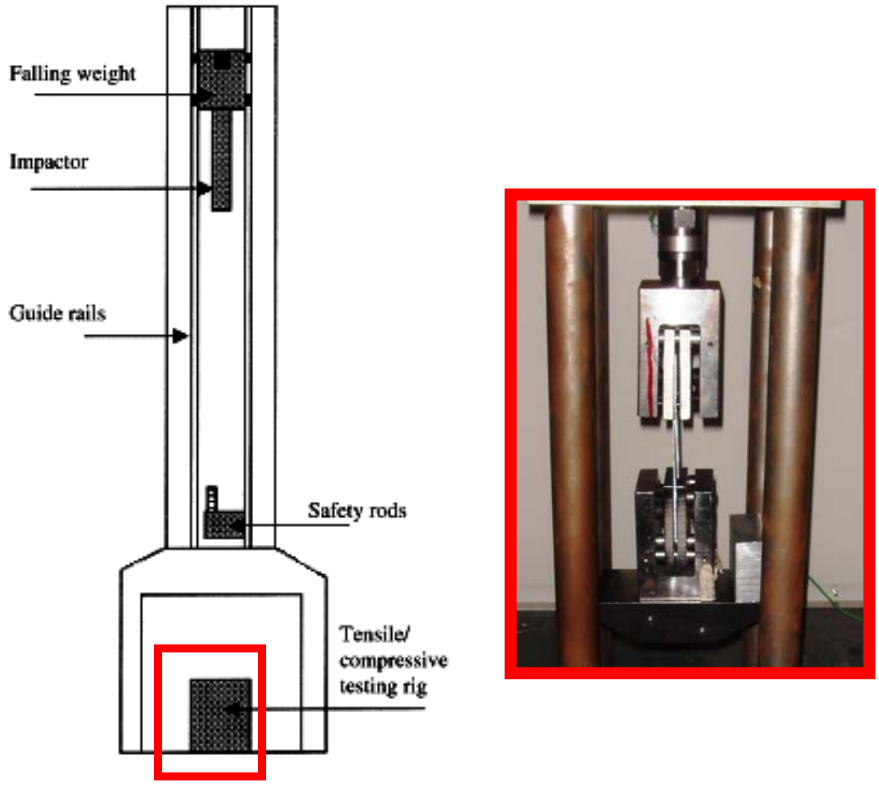

Figure 3.8: Schematic of falling weight test [54]

3.4.1 Peel Testing

Coach peel testing was facilitated by using a manual roller similar to the one shown in Figure 3.9 a). After peeling the sample the major and minor button diameter were measured to attain an average button diameter as shown in Figure 3.9 b).

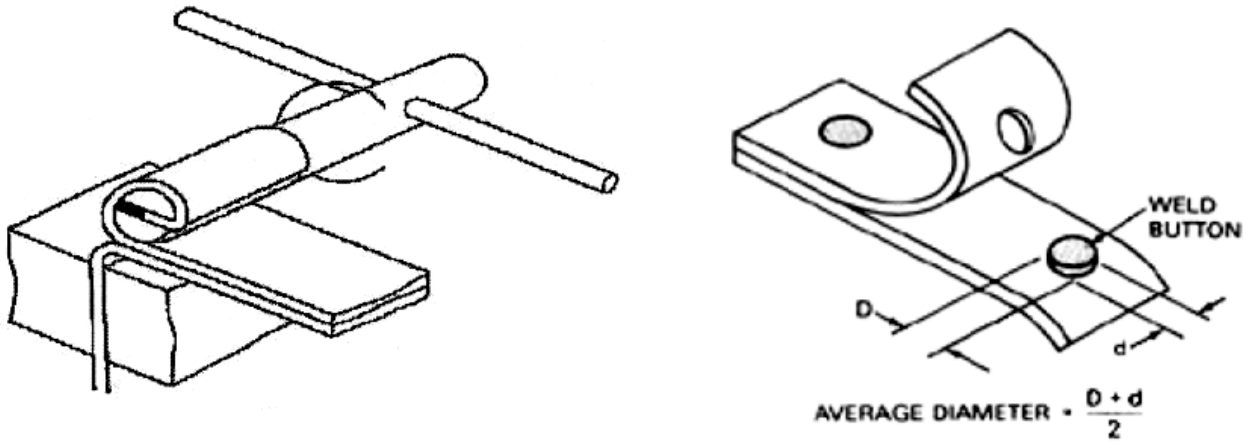

a) Test Method b) Quantitative analysis

Figure 3.9: Coach-peel testing

Microhardness testing was conducted using a Clemex MT-2001 Vickers microhardness testing machine with a 200 g load and holding time of 15 sec. Microhardness mapping using 0.2 mm grid spacing revealed the hardness distribution and the individual hardness values in selected regions of welded joints.

3.5 Parameter Optimisation

RSW samples were produced over a range of force, current, and time parameters. Optimisation testing was conducted to determine weld conditions which produced acceptable weld qualities as determined by AWS standards [14]. The weld current was varied from 7 to 10 kA, the weld force ranged from 3.5 to 5.5 kN, and the weld time was between 10 and 20 cycles for each material.

The weld samples were subjected to overlap tensile shear testing, coach peel testing, and metallographic examination. A total of 11 tests were conducted per condition including 5 tensile tests, 5 peel tests and 1 sample for metallographic preparation. Optimal welding parameters were attained for tensile shear strength. Acceptable button diameters were determined by using the AWS relationship for material thickness which is as follows:

$$M_W = 4\sqrt{t} \quad (3.3)$$

Where M_w is the minimum nugget diameter and t is the sheet thickness.

3.6 Metallographic Examination

3.6.1 Sample Preparation

During metallographic examination all test sections were etched using Lepera's reagent (4% picric acid and 1% sodium metabisulfite) to distinguish the different phases in the fusion zone, heat affected zone, stir zone and thermo-mechanically affected zone for both RSW and FSSW processes [55]. When this particular etchant is used, martensite is etched white, α-ferrite is grey and bainite is black.

3.6.2 Microscopy

Optical Scanning electron microscopy was used to observe metallographic samples and fracture surfaces, respectively. An Olympus optical microscope was used to obtain micrographs. SEM was performed on a *Jeol JSM 6460* with an attached *Oxford Instruments INCA-350* for energy dispersive spectroscopy (EDS) analysis.

3.6.3 XRD Analysis

XRD analysis was facilitated using a Rigaku MSC micro-XRD. For this particular XRD the Cu k-alpha x-ray source is generated consisting of a 1.54 angstrom wavelength. A 0.8 mm collimater was used to focus on the different welding region of TRIP780. Data conditioning was conducted using the JADE software which accompanies the XRD equipment.

CHAPTER 4: RESISTANCE SPOT WELDING OF ADVANCED HIGH STRENGTH STEEL

4.1 Parameter Optimization and Mechanical Properties

Figure 4.1 shows the representative data for tensile and peel tests conducted on the DP600 alloy. Results for the other materials tested in this study are available in Appendix A. From this data the optimal weld schedule for a particular material can be determined. Trends show that failure loads and button diameter increase with weld time and current. However, increasing the welding force generally results in a reduction of failure loads and button diameter. As mentioned in Chapter 2, welds within the upper and lower limits are produced within acceptable current, force and time parameter ranges. Welds below the lower limits have insufficient button diameters, while welds exceeding the upper limit produce expulsion. The optimal welding schedule required for DP600 to produce the maximum failure load (15.9 kN) consists of 8 kA current, 3.5 kN force and a 20 cycle weld time.

Increasing current and time coupled with decreasing weld force results in higher heat generation at the faying interface. From Equation 1.1 it can be shown that both current and time are proportional to the amount of heat generated during welding. As mentioned in Chapter 2, increasing weld force can reduce contact resistance and hence adversely affect the amount of heat generated. As a result, decreasing welding force increases contact resistance, which generates more heat at the interface. Furthermore, this promotes the formation of larger nuggets and increases bonded area which is reflected in the higher failure loads. Failure loads increase until optimal welding conditions are achieved, after which expulsion can occur. Expulsion typically introduces defects into the weld metal which can include excessive indentation and loss of material.

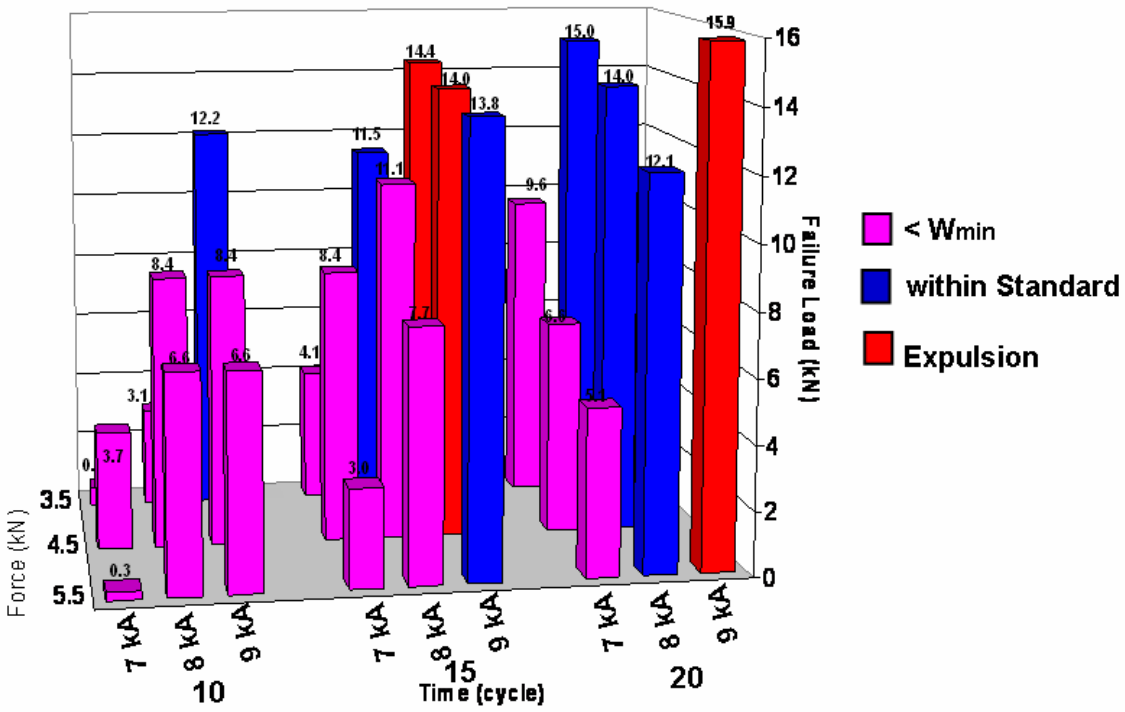

a) Tensile Testing

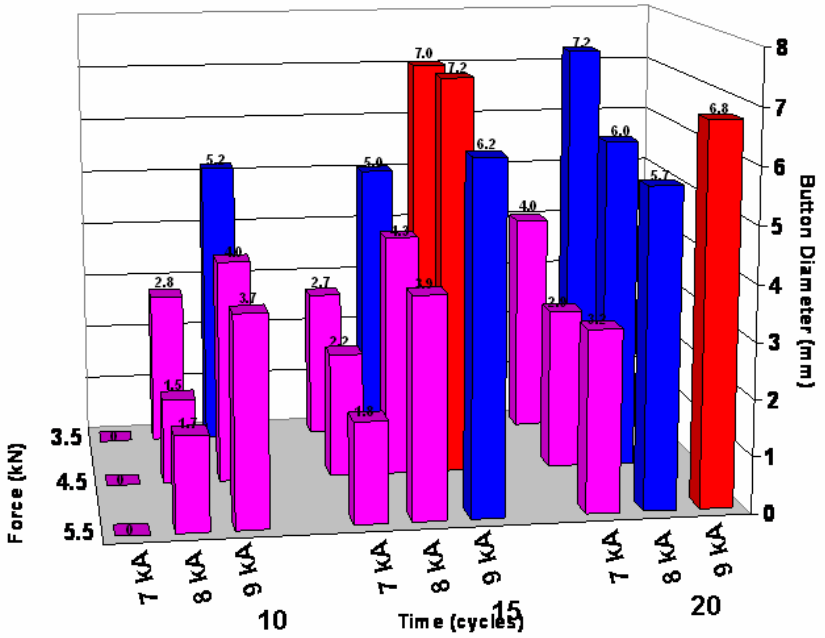

b) Coach Peel Testing

Figure 4.1: Representative weld lobe data for DP600

Table 4-1 displays the optimal welding condition attained from weld lobe testing using welding force, current and time as variables. These conditions produced weldments with the highest tensile shear properties within the lobe domain. Mechanical properties of welds are displayed in Figure 4.2. Highest and lowest tensile strengths were attained by DP780 and HSLA, respectively. Comparable failure loads were achieved for DP600, 590R and TRIP780. Trends mainly reflect those observed with button diameters; failure loads increase with button diameter. However, the TRIP780 produced a notably reduced button size compared to the other welded AHSS. It is also noted that the relatively lean chemistry HSLA required the highest current and time at a relatively low force to attain the optimal weld. This reflects results shown in Chapter 2, which state the lower resistivity of HLSA demands increased time and current compared to AHSS.

Table 4-1: Optimal welding parameters

	Welding condition		
	Force (kN)	**Current (kA)**	**Time (cycles)**
HSLA	3.5	9	20
DP600	3.5	8	20
590R	5.5	9	20
DP780	5.5	9	15
TRIP 780	4.5	8	20

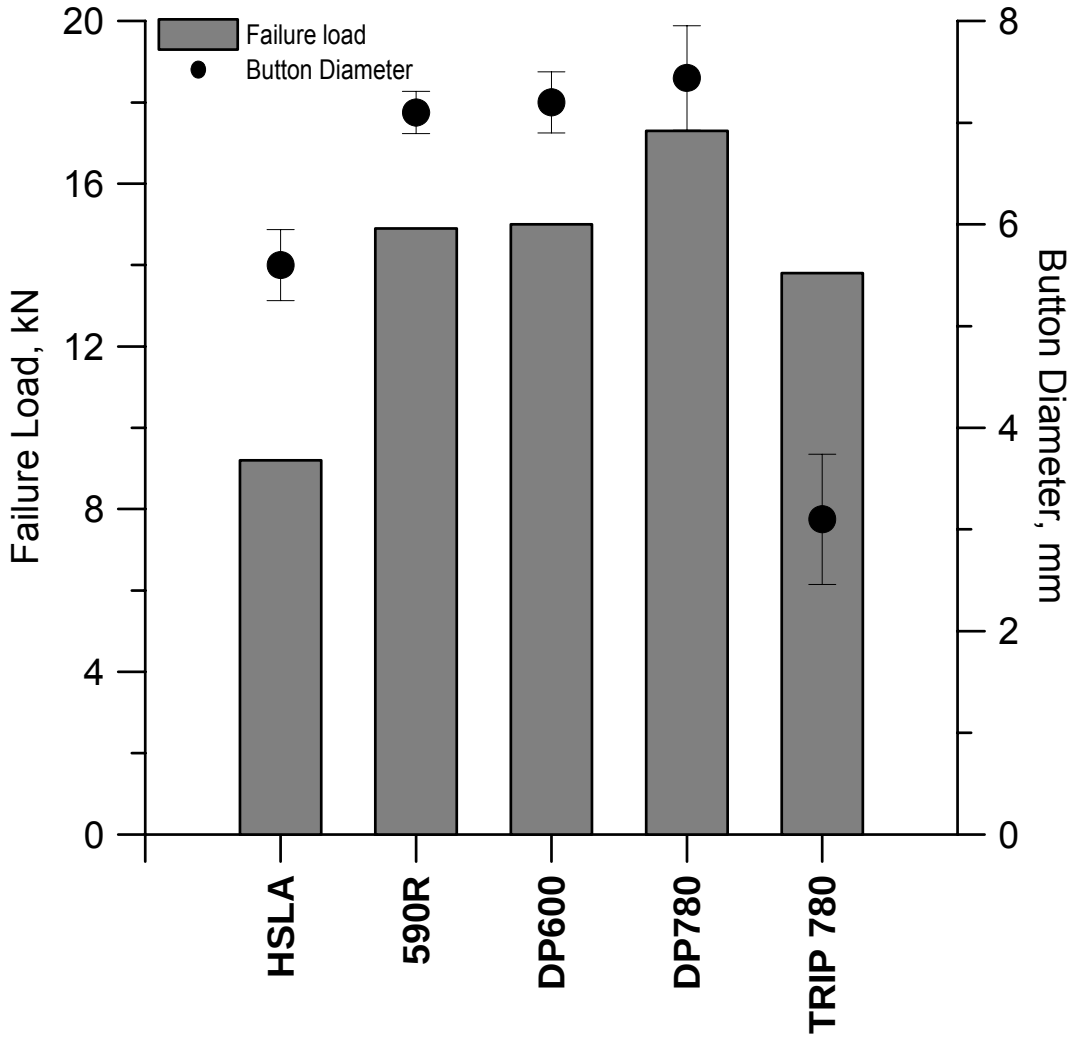

Figure 4.2: Mechanical Properties of weldment

4.2 Microstructural Observations

By examining weld cross-sections the different regions including base metal (BM), heat affected zone (HAZ) and fusion zone (FZ) are revealed. Detailed microstructural observations of these regions are shown for each material in Figure 4.3 to 4.8. Welding parameters used for each material correspond to optimal welding conditions shown in Table 4-1.

4.2.1 HSLA

Figure 4.3 (a to d) shows the weld microstructure for HSLA steel. The BM microstructure consists of ferrite grains (grey) ranging from 5 to 10 μm in

diameter with carbides (dark colored) situated at grain boundaries (Figure 4.3 a). The IC HAZ consists of finely dispersed martensite (white) particles and carbides (black) within the ferrite matrix (grey). The fine structure in the FG HAZ results from peak temperatures slightly surpassing Ac_3, which promotes austenite nucleation while rapid cooling limits grain growth, forming the fine grained structure. The CG HAZ shown in Figure 4.1 c) consists of blocky grains ranging 5 μm to 10 μm in size. The needle like structure consists of island and sideplate ferrite with stripes of grain boundary ferrite. The FZ consists of a columnar structure composed mainly of martensite, which is shown in Figure 4.3d).

4.2.2 590R

Microstructural observations for 590R are shown in Figure 4.4. BM microstructure consists of non-uniformly sized ferrite grains (grey) with grain boundary bainite (black), shown in Figure 4.4 a). The IC HAZ contains islands of martensite as shown in Figure 4.9 b). Microstructure in the CG HAZ, Figure 4.9 c), appears to be predominantly martensitic consisting of large blocky grains ranging 20 μm to 25 μm in diameter. The FZ contains a directional columnar structure growing towards the centerline. A needle like martensitic structure within the FZ is shown in Figure 4.9 d).

4.2.3 DP600

A representative RSW weld cross-section for DP600 is shown in Figure 4.5. BM microstructure in Figure 4.5 a) shows the typical finely dispersed martensite particles (white) surrounded by a ferrite matrix (grey), which are characteristic of dual-phase steels. Volume fraction of martensite increases in the IC HAZ, Figure 4.5c). The CG HAZ microstructure consists of blocky martensite grains about 10 to 15 μm in diameter as shown in Figure 4.5c). The FZ shown in Figure 4.5d) is characterized by the columnar nature of solidification mainly consisting of martensite.

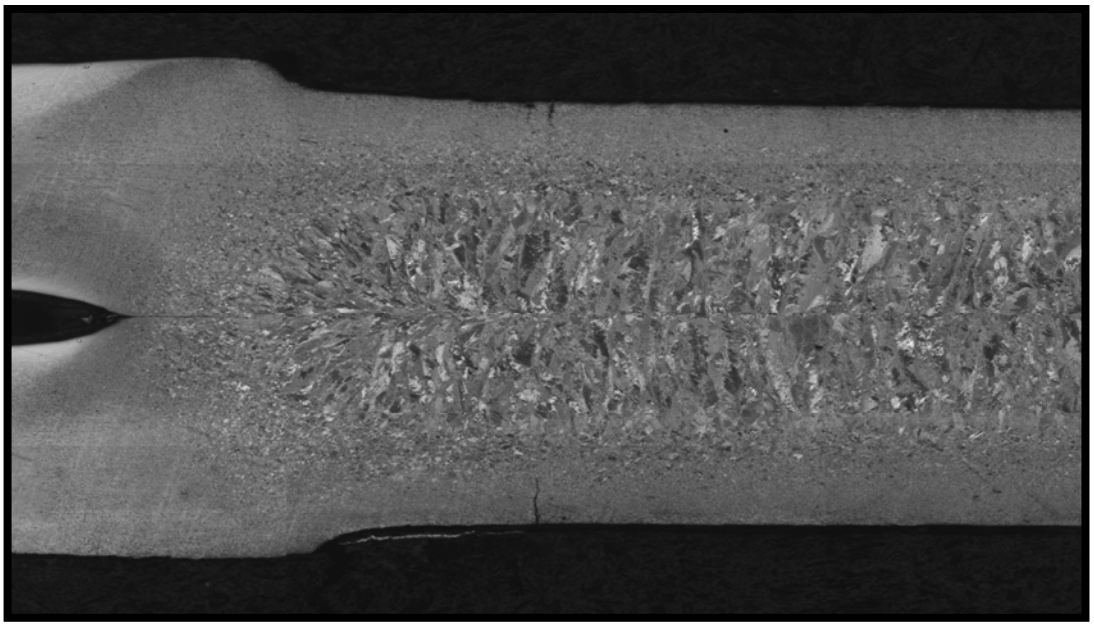

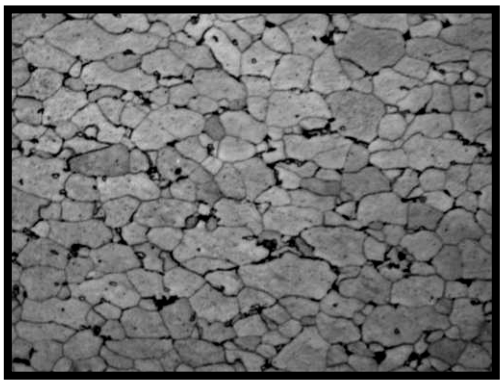

a) Base metal

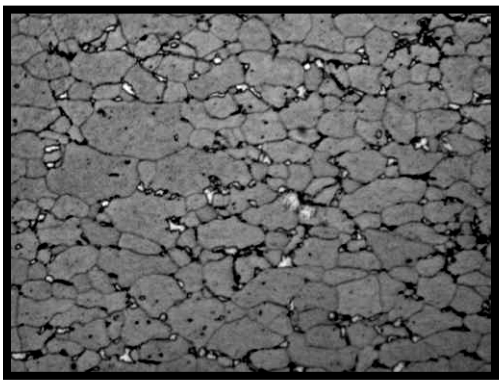

b) Intercritical HAZ

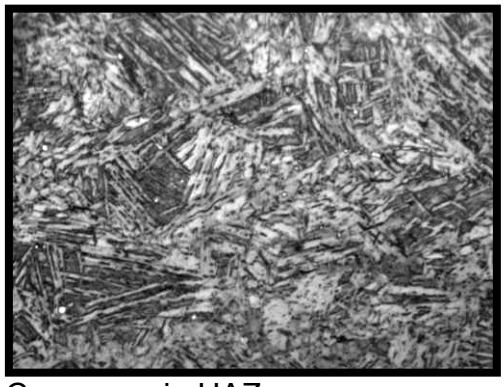

c) Coarse grain HAZ

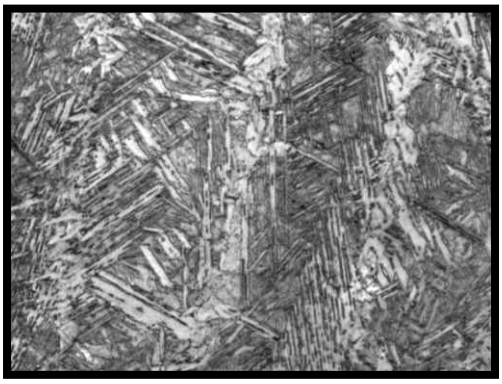

d) Fusion zone

Figure 4.3: Microstructure for HSLA

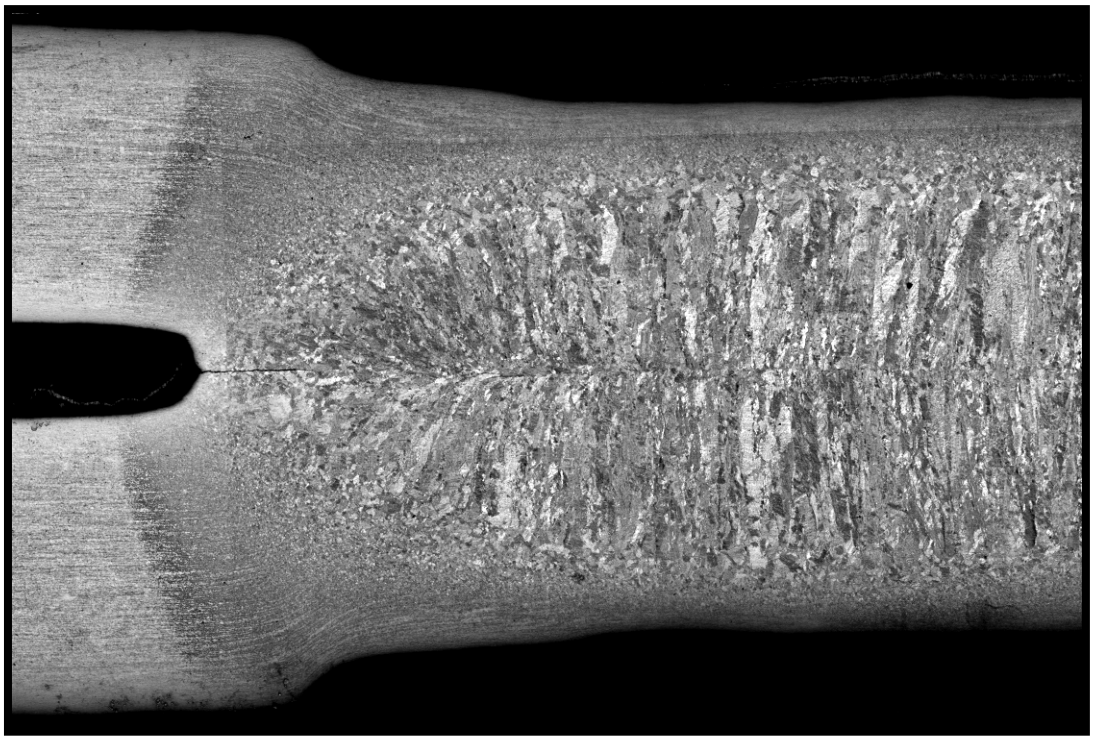

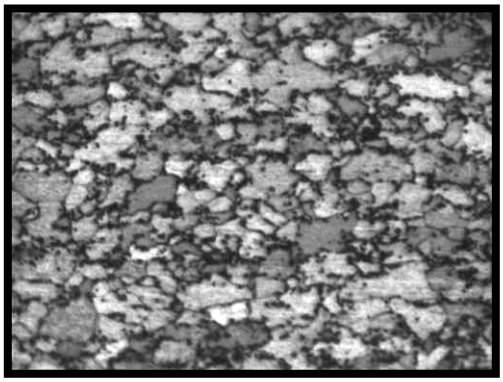

a) Base metal

b) Intercritical HAZ

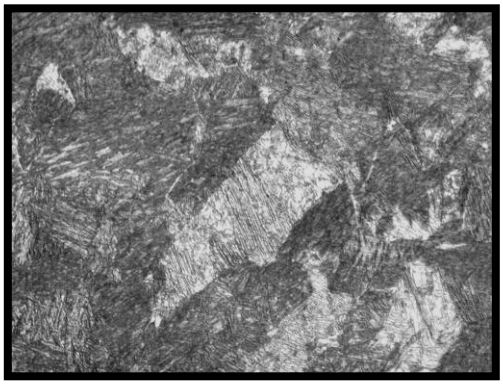

c) Coarse grain HAZ

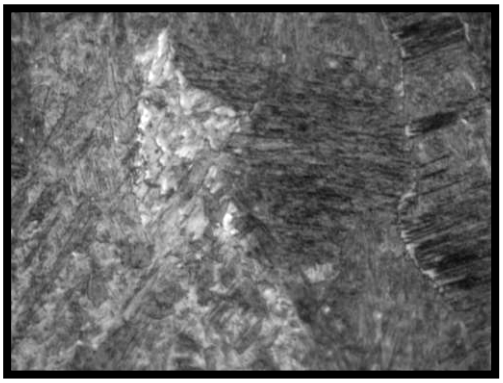

d) Fusion zone

Figure 4.4: Microstructure for 590R

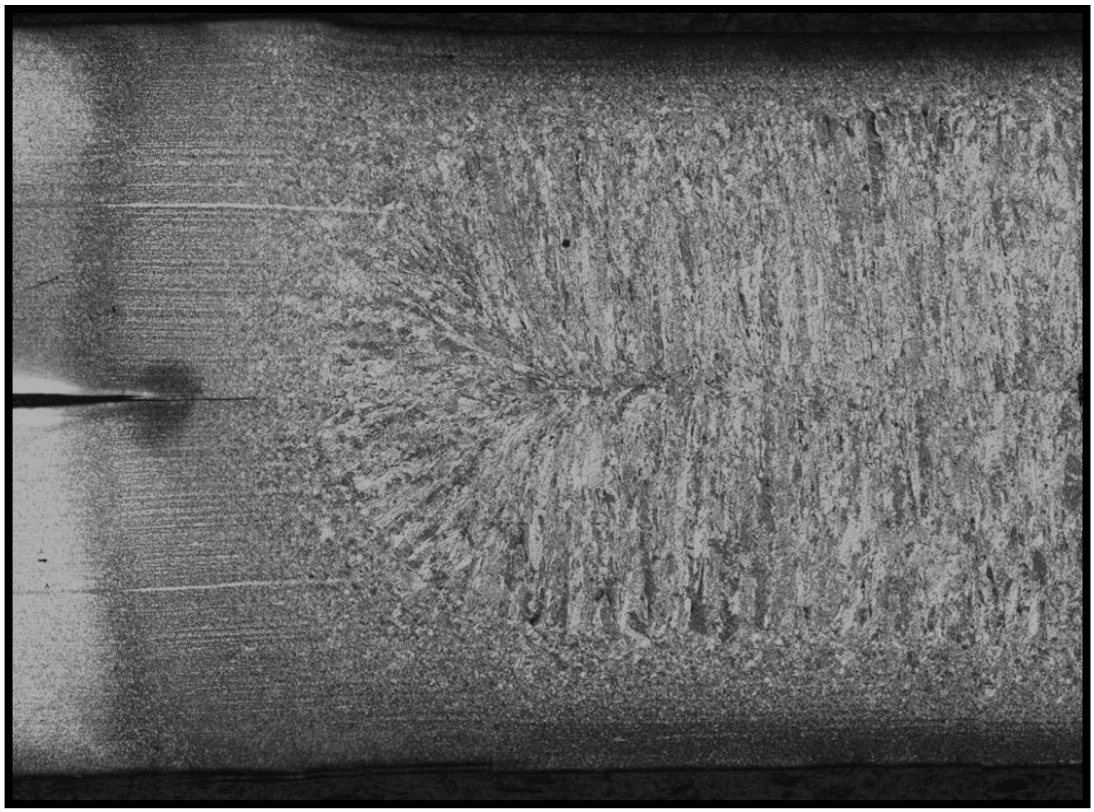

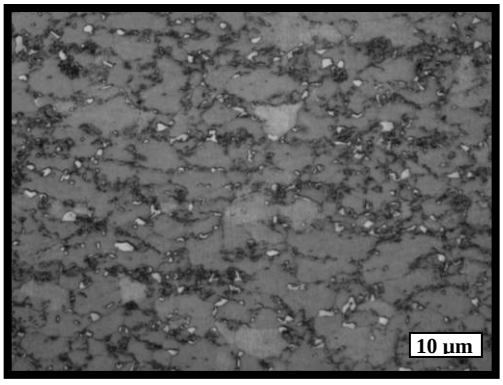

a) Base metal

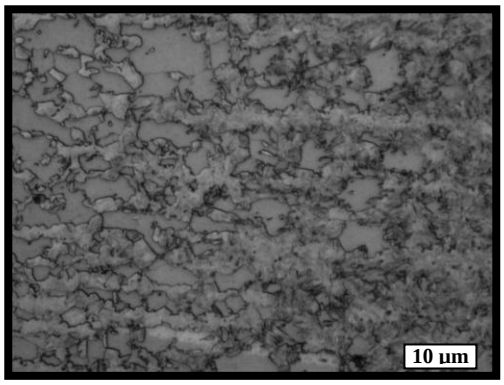

b) Intercritical HAZ

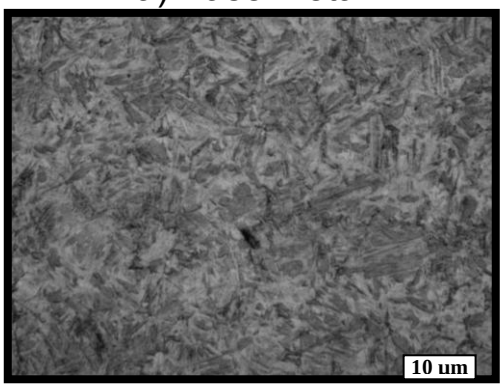

c) Coarse grain HAZ

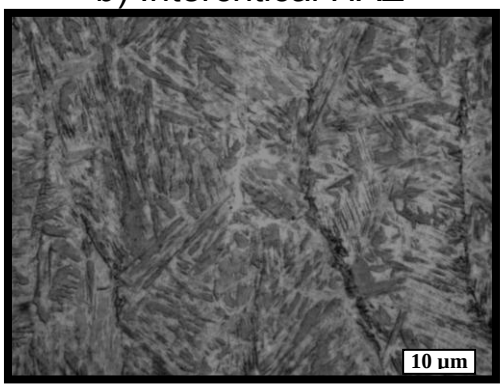

d) Fusion zone

Figure 4.5: Microstructure of DP600 Weld

4.2.4 DP780

Figure 4.6 (a to d) shows the cross-section microstructure for DP780. The BM consists of dispersed martensite in a ferrite matrix (Figure 4.6a). Compared to DP600, the base metal microstructure contains larger martensite particles with a banded formation. The IC HAZ shown in Figure 4.6 b) consists of larger martensite particles (left) which begin to decompose approaching the FG HAZ (right). Figure 4.6 c) shows a large blocky structure in the CG HAZ where prior austenite grains ranged 20 to 30 μm in diameter. The FZ consists of a large columnar martensitic structure shown in Figure 4.6 d).

4.2.5 TRIP780

Microstructures of TRIP780 weld regions are shown in Figure 4.7 a to d. BM microstructure consisting of retained austenite (white) and dispersed bainite (black) within a ferrite matrix (grey) can bee seen in Figure 4.7a).The IC HAZ shown in Figure 4.7b) contains partially dissolved ferrite grains which become increasing in smaller approaching the fine grained HAZ (right). The fine grained structure is shown approaching the right side of Figure 4.7b). Figure 4.7c) shows the CG, which contains a predominately martensitic structure with large blocky grains approximately 20 to 30 μm diameter in size. FZ for this material also contains the large columnar martensitic structure exhibiting centerline growth, as shown in Figure 4.7 d).

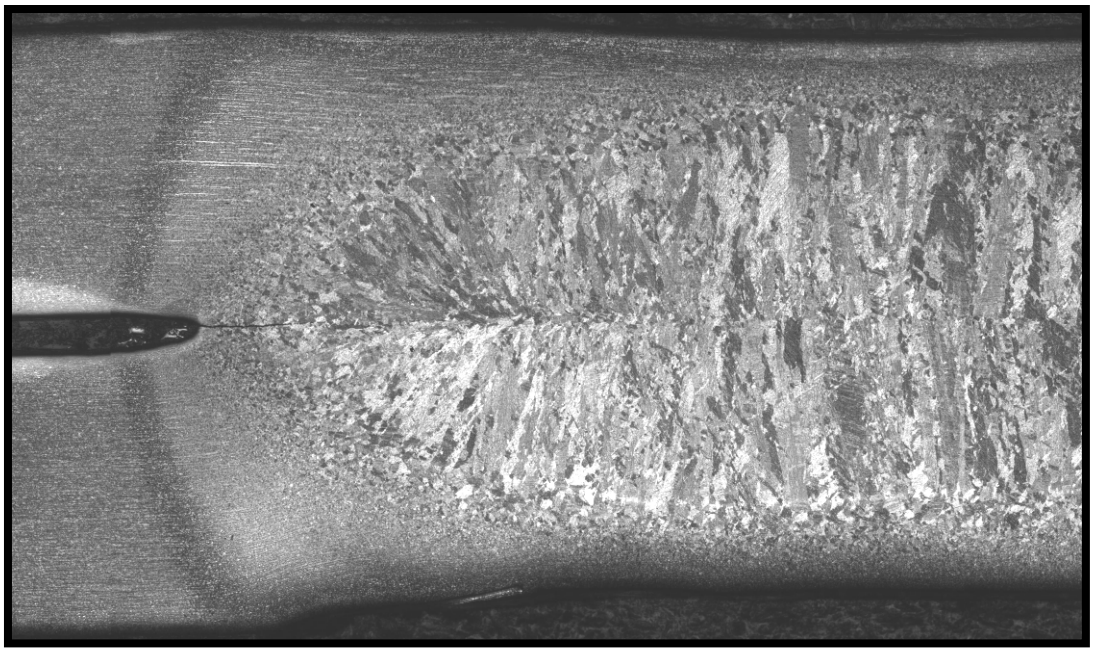

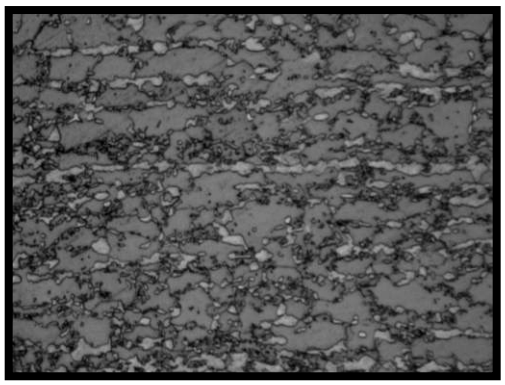

a) Base metal

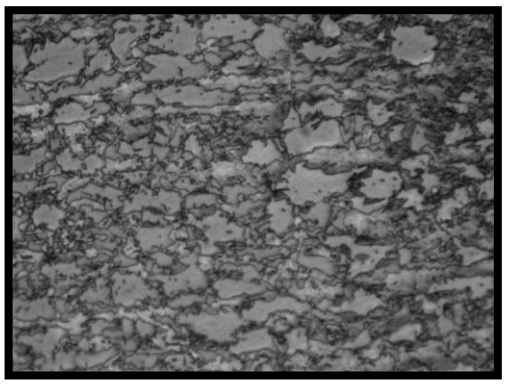

b) Intercritical HAZ

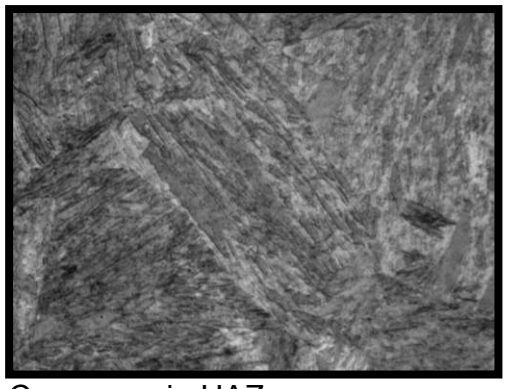

c) Coarse grain HAZ

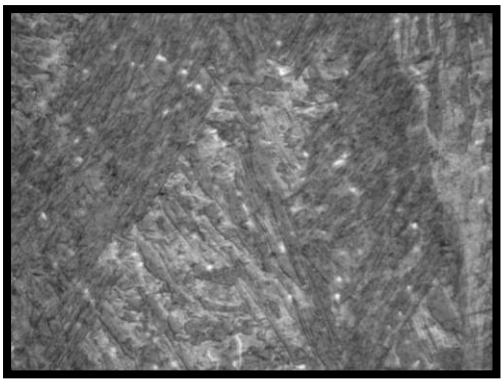

d) Fusion zone

Figure 4.6: Microstructure for DP780 spot weld

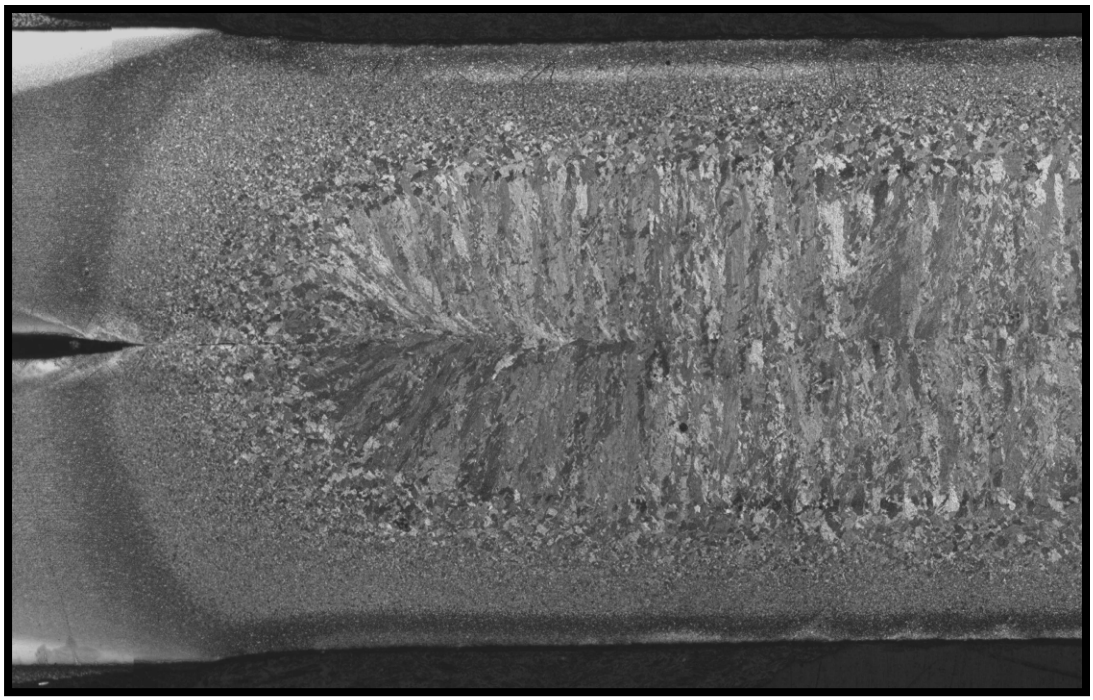

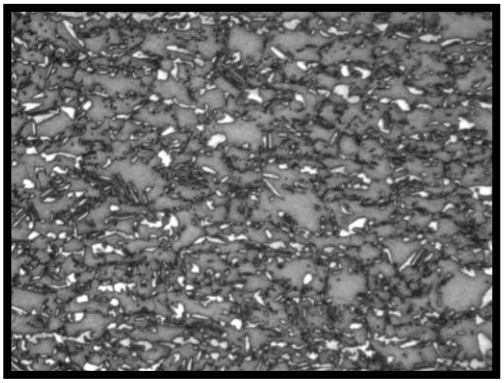

a) Base metal

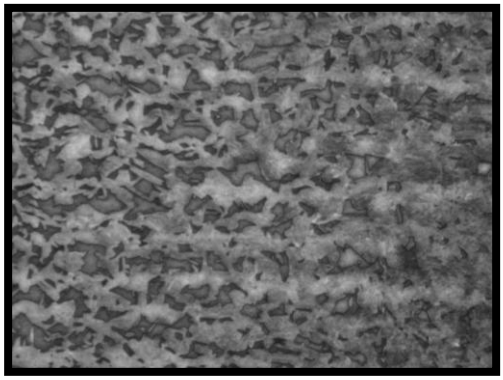

b) Intercritical HAZ

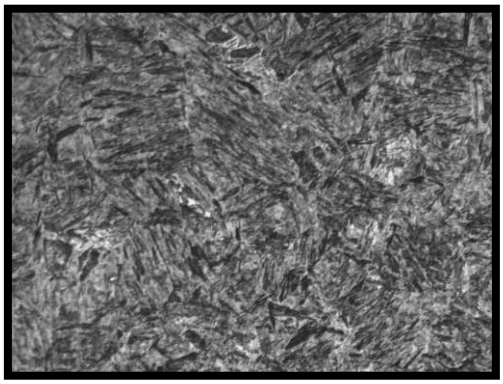

c) Coarse grain HAZ

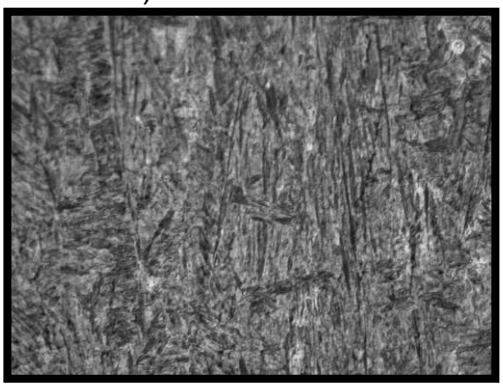

d) Fusion zone

Figure 4.7: Microstructure for TRIP780 spot weld

4.3 Hardness observations

Hardness mapping results for the weld regions including BM, HAZ and FZ are shown in Figure 4.8 to 12. Each material shows an increased FZ hardness relative to BM values. All AHSS produce FZ hardness values exceeding 350Hv compared to the HSLA which exhibits values ranging about 300Hv. Detailed analyses of hardness values and microstructural constituents in these regions are detailed in the following sections.

4.4 Discussion

4.4.1 Base Metal

To understand microstructural effects on the mechanical performance of welds, it is important to develop differences in microstructure between different types of AHSS. The weld and surrounding material consists of several regions with differing microstructure which results from the thermal history during welding. In some of these regions post-weld microstructure depends heavily on the BM structure, while in other regions effects of the BM is less clear because peak temperatures are well above those which produce fully homogeneous austenized microstructures. Thus, it is critical to first develop a clear understanding of the base metal microstructure.

BM temperatures during welding typically remain below 200^{o}C without activating any transformations, leaving microstructural constituents unaffected. Hardness values in the base metal depend mainly on alloying chemistries and processing methods used during the production of high strength steel. For all materials used for this study the matrix is ferritic; however different chemistries and processing result in different strengthening phases between the various AHSS; including carbides, bainite, martensite and austenite.

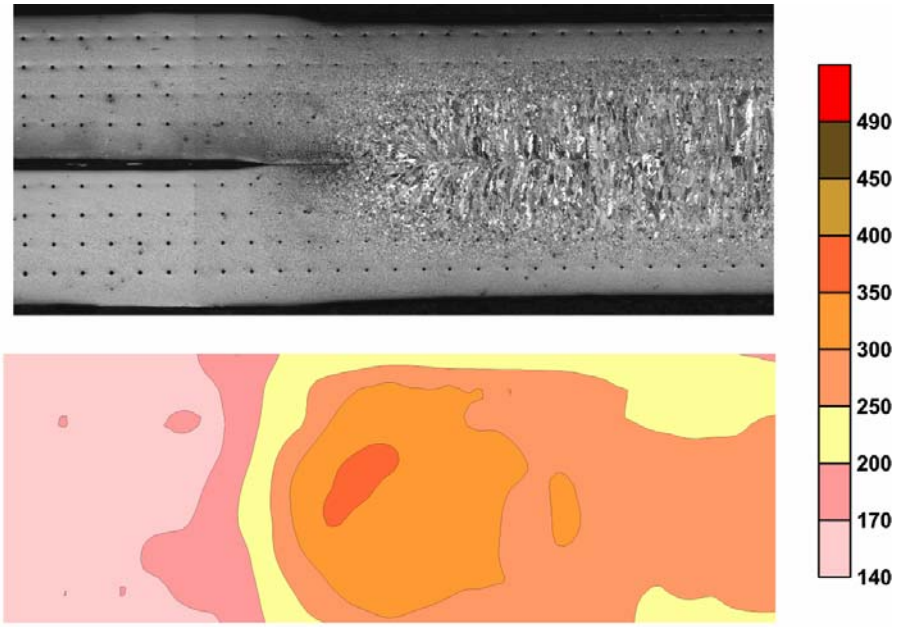

Figure 4.8: Hardness mapping of HSLA RSW weld

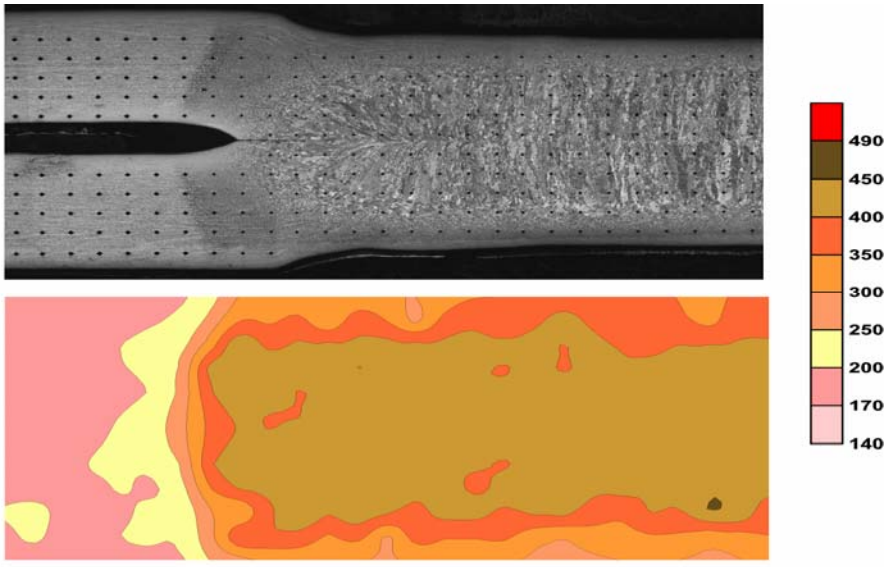

Figure 4.9: Hardness mapping for 590R RSW weld

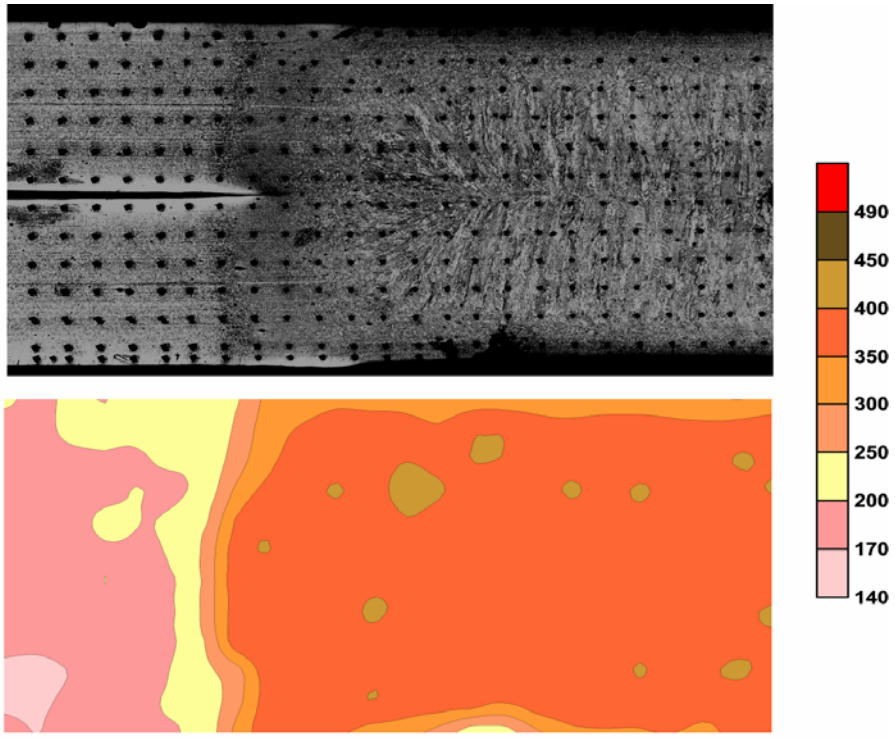

Figure 4.10: Hardness mapping of DP600 RSW weld

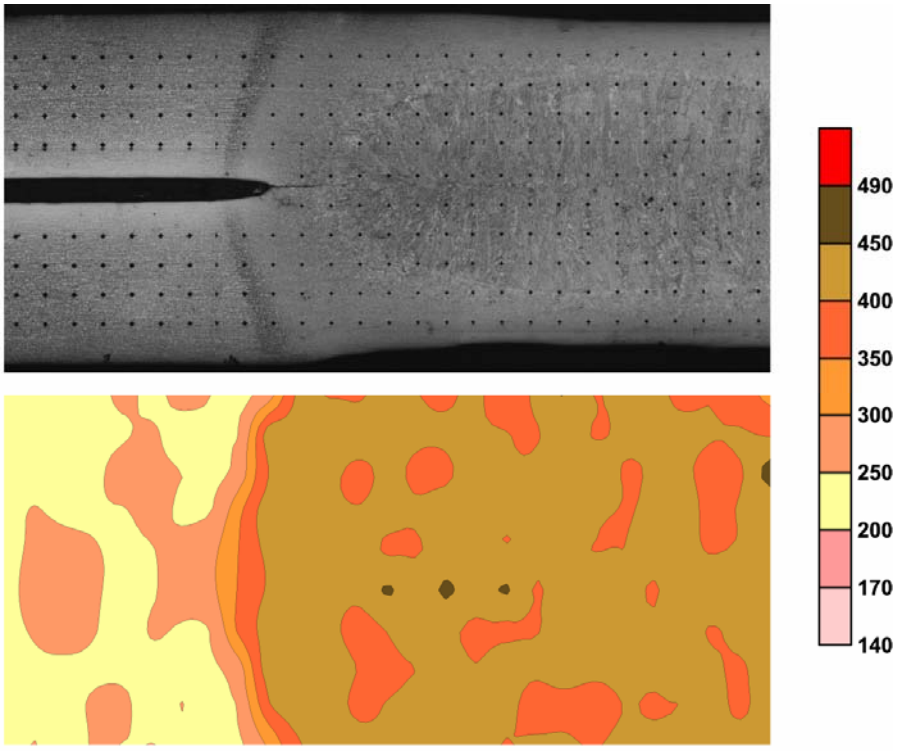

Figure 4.11: Hardness Mapping for DP780 RSW weld

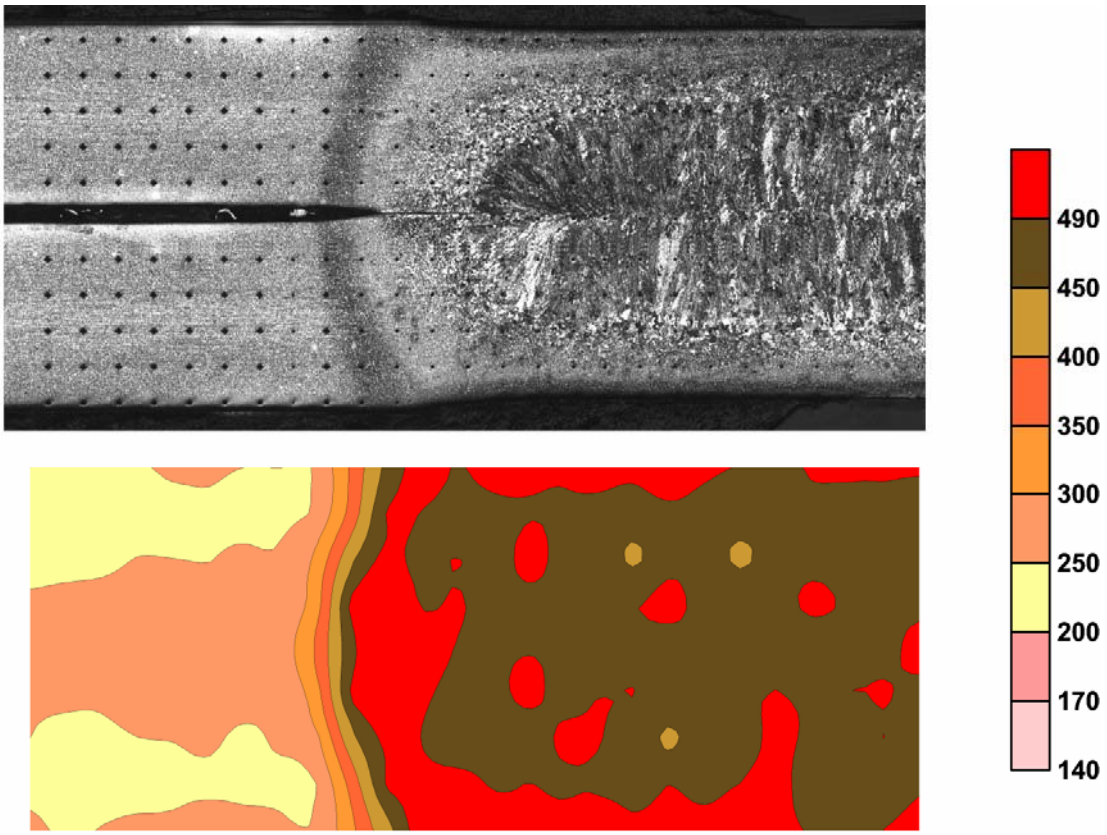

Figure 4.12: Hardness Mapping of TRIP780 RSW weld

The HSLA microstructure is shown in Figure 4.1 a) which consists of ferrite and dispersed carbides at the grain boundaries. The resulting hardness is about 150 Hv. Figure 4.4a) shows the 590R microstructure also comprising of a ferrite matrix, however embedded islands of bainite act as the strengthening phase. Hardness values for the richer chemistry 590R are slightly higher then HSLA, ranging from 170 to 200Hv.

The DP steel, as shown in Figure 4.5 and 4.6 for DP600 and DP780, respectively, shows a ferritic matrix with dispersed martensite at grain boundaries. The volume fraction of martensite increases from DP600 to DP800, resulting in an increase in hardness, from 170 to 250Hv. The DP780 base metal shows a banded structure of martensite within the base metal. This banding is aligned with the rolling

direction; compared to the uniformly dispersed martensite observed in the DP600 base metal. The difference in martensite volume fraction and dispersion in the DP base metal is due to varying chemistries and processing techniques used during manufacturing [56]. Increased chemistries tend to facilitate the formation of martensite, which ultimately increases the martensite volume fraction.

TRIP780 BM consists of a relatively complex microstructure, Figure 4.7 a), containing a ferrite matrix with retained austenite and finely dispersed bainite. Hardness distributions revealed a slightly harder center along the BM profile. The outer edge hardness was below 200Hv while the center values are slightly higher, which can be attributed to production methods used during processing [57]. The TRIP780 had the highest BM hardness values of all the steels tested in this study.

4.4.2 Fusion Zone

Temperatures in the FZ surpass the liquidus temperature resulting in molten metal during welding. This is followed by rapid cooling which promotes the epitaxial solidification of dendrites with directional growth towards the centerline. After welding the water cooled electrodes remove heat from the weld. This causes rapid cooling in the solidified weld metal. It has been reported that RSW cooling rates are on the order of 10^5 ^{o}C/s [58,59,60]. Since the alloying levels in AHSS are relatively high, transformation of austenite at high cooling rates typically results in martensite or bainite. The characteristic features of epitaxial columnar grains growing towards the centerline and a bainite-martensitic microstructure are common to all the steel types shown in Figure 4.1d) – 4.6d).

FZ hardness values varied for each material. HSLA FZ hardness values were the lowest out of all the materials tested, ranging 250-350Hv as shown in Figure 4.8. 590R and DP600 exhibited similar strength and BM hardness values; however FZ hardness values were considerably different, 400-450Hv and 350-400Hv respectively. For the DP780 FZ hardness was similar to 590R ranging between 400-450Hv. Maximum hardness values were attained from TRIP780 which

exhibited values above 450 Hv. Martensite hardness ranges above 350 Hv for carbon contents in excess of 0.05 wt % [61]. Hence, FZ hardness values for AHSS are well within the expected martensite hardness range.

During RSW, melting in the FZ removes the processed BM microstructure while continuously cooled copper electrodes promote rapid post-weld cooling. This typically results in transformation of fully austenitic regions into predominately martensitic structures. Results have shown the FZ for rich chemistry steels (DP and TRIP) to consist mainly of martensite. Leaner chemistry HSLA showed a mixed FZ microstructure (martensite and bainite), which is likely due to differences in the HSLA CCT diagram compared to the AHSS. CCT diagrams for leaner HSLA are usually shifted towards to the left, which can bring the bainite nose within the transformation time to start bainite nucleation in the FZ during RSW. However, since all of the AHSS showed a fully martensitic FZ microstructure then the FZ hardness mainly is a function of alloy levels within the steel.

As was shown in Chapter 2, carbon can influence the ability to form martensite, also referred as hardenability, and increase the overall hardness of martensite. Using carbon content to predict martensite hardness was viable for traditional lean chemistry steels, which mainly contained only iron and carbon and low levels of other alloying elements. Yurioka et al. measured martensite hardness of various basic oxygen converter (BOC) steels produced using high cooling rates achieved from arc welding [62]. Using this experimental data the following relationship was derived:

$$H_M = 884(1 - 0.03C^2) + 294 \qquad 4.1$$

Where H_M is martensite hardness and C is wt% carbon content.

Figure 4.13 shows the FZ hardness as a function of carbon content for experimental data of various AHSS. Calculated fusion zone martensite hardness attained from Equation 4.1 is also plotted. There were 5 steels studied in this work with a carbon range from 0.06 to 0.188 wt%. This figure can be further populated using experimental data from several sources including Gould et al. [63], Marya et al. [64] and Uijl et al. [65] who have also done work in this area.

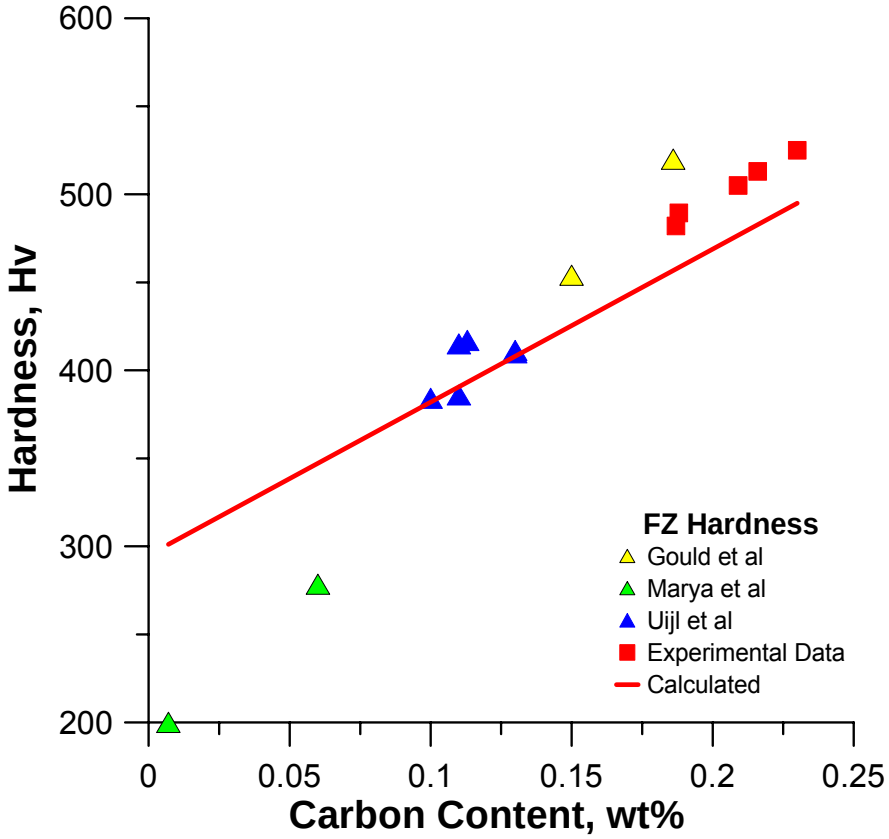

Figure 4.13: Carbon Equivalence Vs Vickers Hardness

Examination of Figure 4.13 shows an over-prediction of hardness values for lower carbon steels, which includes an interstitial free (IF) steel alloy and the tested HSLA. Deviation from predicted values can be attributed to a mixed martensite-bainite microstructure in the FZ of these steels. Since Equation 4.1 was developed for martensitic structures, an over-prediction can occur when applied to lower carbon steels which do not form a fully martensitic structure. However the intermediate chemistry steels show a relatively good agreement to Equation 4.1.

Higher carbon steels, including AHSS, show higher FZ hardness than the predicted values. These steels also contain higher concentrations of alloying elements such as Mn, Mo, Si and Al. The addition of some alloying elements can enhance the effectiveness of carbon in martensite which results in a harder structure after rapid solidification. Hence, inaccuracies may be due to the sole use of carbon content as a measure for predicting FZ hardness. The effects of other alloying elements are not considered in Equation 4.1. Other studies have suggested secondary hardening caused by tempering results in increased material hardness[66].

As mentioned in Chapter 2, alloying elements can aid the formation of martensite by increasing required transformation times and hence the CE provides an effective means of measuring the effects of alloying elements in the formation of martensite. Figure 4.14 shows the relationship between FZ hardness and carbon equivalence calculated using CE(IIW) and P_{cm} for the appropriate carbon range. Considerable scatter is observed for the CE (IIW) and P_{cm} equation. Using a linear regression fit, an attempt was made to find correlation between carbon equivalence and FZ hardness. However there is minimal agreement and the scatter is reflected in the relatively low linear correlation coefficient value (r = 59.36%). Yurioka et al. also realized some difficulties when applying the CE (IIW) and P_{cm} in determining preheat temperatures and proposed an improved CE equation [62].

Alloying elements and CE_Y for each material are shown in Table 3-2. Carbon equivalence values calculated using the equation developed by Yurioka et al. [67] are also tabulated. The HSLA alloy exhibiting the leanest chemistries produced the lowest CE value while the heavily alloyed TRIP780 resulted in the highest CE value.

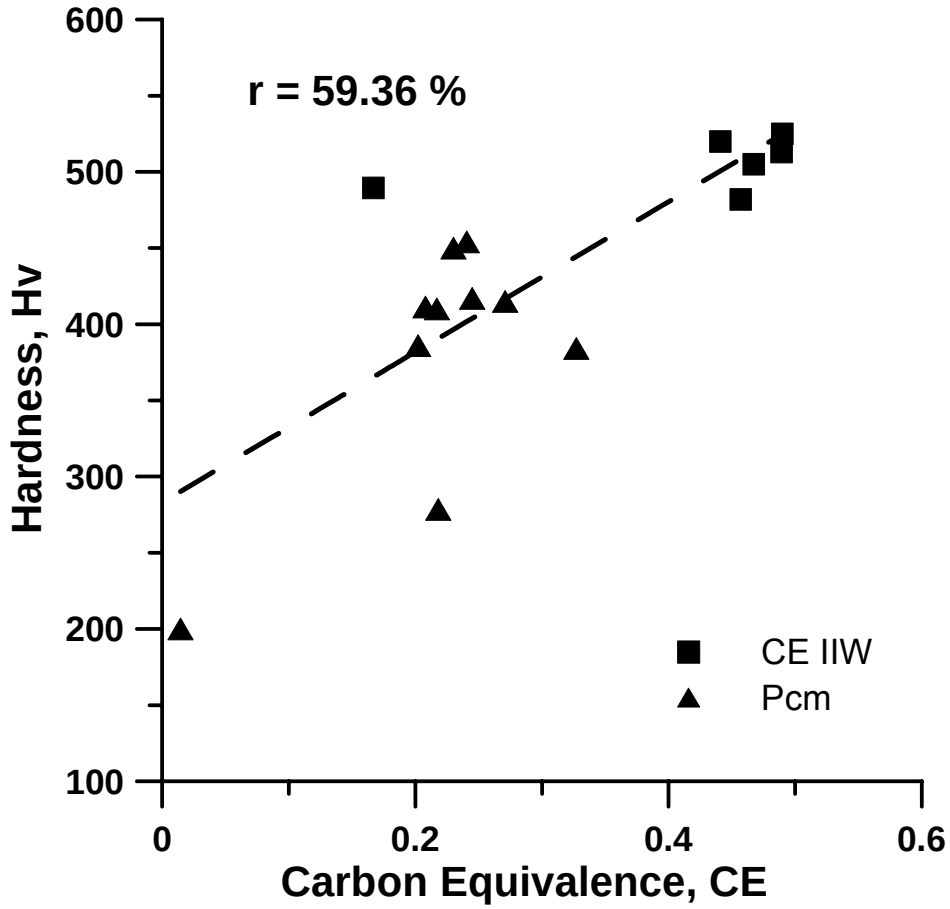

Figure 4.14: Fusion zone hardness Vs P_{cm} and CE(IIW)

CE and average FZ hardness are plotted in Figure 4.15 CE_Y for each steel alloy. Trends show FZ hardness increases with richer chemistries that produce higher CE values. CE_Y shows an improved linear relationship between fusion zone hardness and base material chemistry. Extracting the linear relationship between FZ hardness and CE gives the following equation:

$$Hv_{FZ} = 630 * CE_Y + 188 \qquad 4.2$$

Where Hv_{FZ} is fusion zone hardness and CE_Y is carbon equivalence calculated using Equation 2.3.

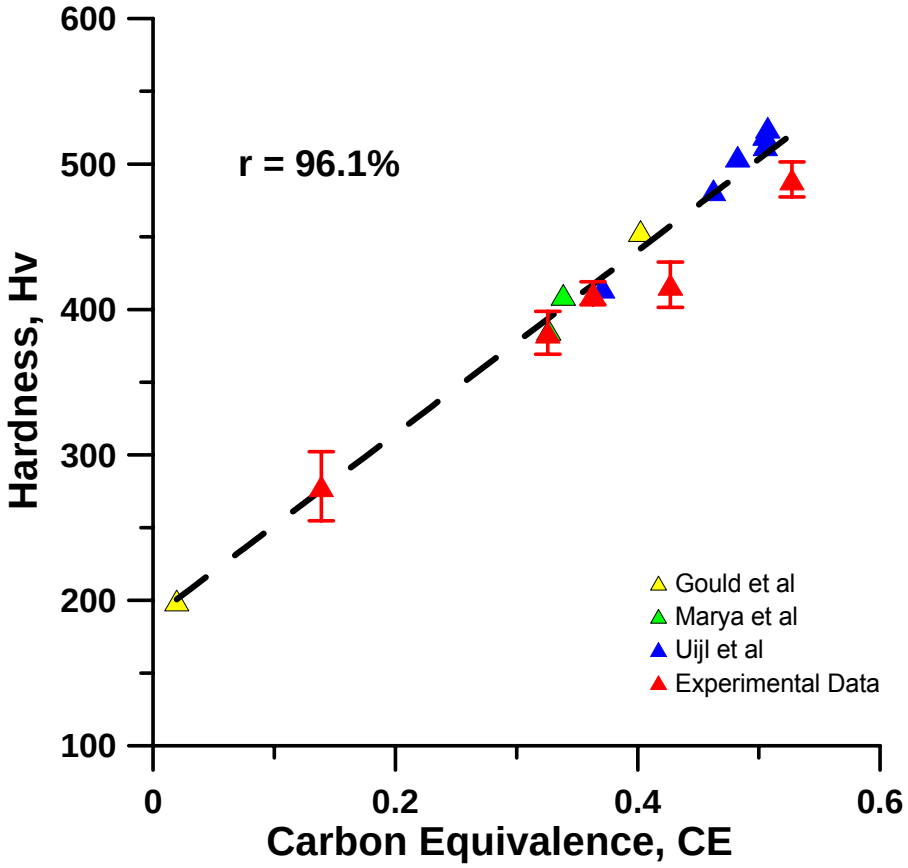

Figure 4.15: CE vs fusion zone hardness

Equation 4.2 provides an improved method for determining the RSW FZ hardness of steels. Compared to Equation 4.1, Equation 4.2 accounts for various alloying elements used in the production of AHSS. By using the Yurioka CE equation, which includes an accommodation factor for a wide range of chemistries, a more reliable relationship between RSW FZ hardness and chemistries can be made.

4.4.3 Heat Affected Zone

Peak temperatures in the CG HAZ are well above Ac_3, transforming all pre-existing constituents into 100% austenite. Growth of austenite grains is facilitated with the extended time spent at elevated temperatures. Subsequent rapid cooling can transform the austenite into a martensitic microstructure and the remanence of prior austenite grains is outlined. Hardness ranges in this region are similar to

FZ hardness values, for example hardness values for DP600 ranged between 350-400 Hv for the FZ and CG HAZ.

The fine grained HAZ exists further from the fusion boundary, the peak temperatures still exceed Ac_3; however they are not so high that grain growth of austenite occurs. The short time above Ac_3 facilitates nucleation of austenite and limits grain growth, producing an ultra fine structure. For most materials, hardness values in this region are similar to CG HAZ and FZ. However peak hardness values for TRIP780 within the FG HAZ surpassed 490Hv. Excess hardness in the FG HAZ can be concerning if fracture initiates or propagates within its domain. However, high hardness values in this region for TRIP780 can be attributed to grain size effects, which can increase strength and hardness in this sub-region.

Peak temperatures in the IC HAZ range between Ac_1 and Ac_3. Typically during welding these temperatures do not fully austenitize the ferrite structure; however dissolution of other micro constituents into austenite can occur. Rapid post-weld cooling aided by continuously cooled electrodes can result in the transformation of these prior austenite grains into martensite.

In the HSLA IC HAZ, carbides situated at the ferrite grain boundaries austenitize during heating and rapidly cool after current is applied. The resultant microstructure forms martensite islands (white) as observed in Figure 4.8 b). This causes the increase in hardness values which exceed 170 Hv. 590R also experiences a similar thermal cycle with the austenatized bainite transforming into martensite island (Figure 4.4 b) bringing hardness values above 200 Hv (Figure 4.9).

The IC HAZ of dual phase alloys undergoes a coarsening of the martensite phase. Peak temperatures slightly exceeding Ac_1 initiate dissolution of martensite and some ferrite into austenite, which is then rapidly cooled. This increases the

volume fraction of martensite bringing hardness values above 200Hv and 250Hv for DP600 and DP780 respectively (Figure 4.10-13). Approaching the fusion boundary, peak temperatures approach Ac_3 and result in almost all of the ferrite being dissolved into austenite. Post-weld rapid cooling subsequently forms nearly a 100% martensitic structure.

Figure 4.7 b shows the banded structure within the TRIP780 IC HAZ which undergoes the dissolution and coalescence of retained austenite and bainite. Hardness values for TRIP exceed 300Hv. XRD results suggest the coexistence of both austenite and martensite phases within this region (Figure 4.16). Intercritical annealing of Si rich TRIP steel has shown decomposition of austenite [68, 8]. Furthermore, the increase in martensite start time with decreases C concentration has been reported [69]. This inhomogenuety in chemistries coupled with the rapid cooling rates can result in the austenite and martensite.

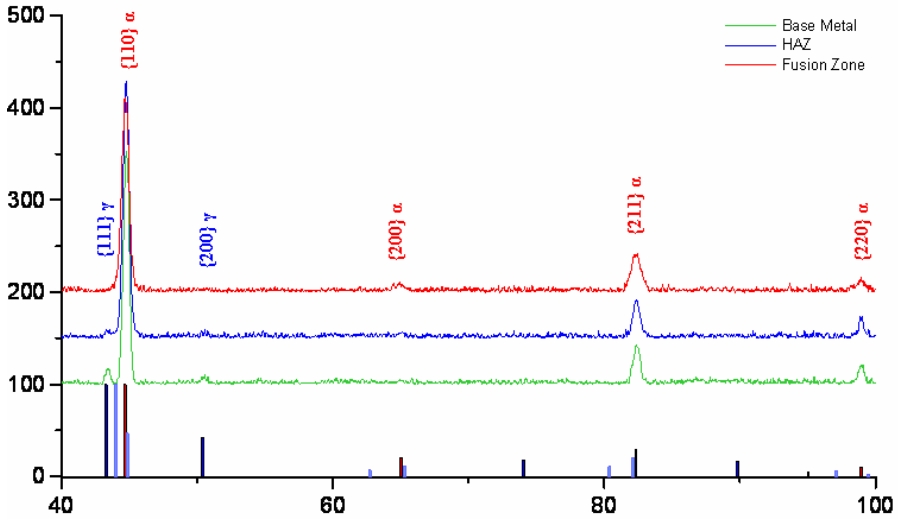

Figure 4.16: XRD results for BM, IC HAZ and FZ of TRIP spot weld

Observed microstructure in the IC HAZ contained evidence of ferrite and a white banded structure. Variations of shading within the banded structure suggests an inhomogeneous composition resulting in differing intensities of chemical attack by enchants. Results from XRD analysis of BM, HAZ and FZ of TRIP780 are

shown in Figure 4.16. BM analysis show peaks for austenite and ferrite which are the main constituents observed using metallographic examinations. Within the HAZ a reduction in intensity for the austenite peaks and a slight increase in BCT martensite is observed. This transition can pertain to a combination of austenite and martensite in the HAZ. XRD readings of the FZ produced no evidence of austenite peaks hence the predominately martensitic structure in this region as observed via optical microscopy.

4.5 Summary

In this chapter the microstructure and mechanical properties of RSW AHSS were examined. Using standard optimization methods, weldments made using the optimal weld conditions were compared. The AHSS consistently achieved high tensile strength compared to the conventional HSS. Microstructural observations were presented for the different weld region of each spot welded AHSS and HSS. Furthermore, the microstructural observations and hardness testing revealed predominately harder martensite within the FZ of the AHSS, which increased with richer chemistry steels. Finally, an equation to determine RSW FZ hardness was proposed.

CHAPTER 5: FRACTURE SURFACES AND IMPACT TESTING

5.1 Fracture Surfaces and Energy Input

Representative specimens from coach peel and tensile shear tests for each material tested during schedule optimization are shown in Figure 5.1 and Figure 5.2, respectively. Peel testing resulted in a full button failure mode for all material except TRIP780, which exhibited a partial interfacial failure. During tensile testing TRIP780 and DP600 produce Interfacial fractures while the HSLA, DP780 and 590R show button pull-out. Summarized results for failure are shown in Table 5-1 .

Table 5-1: Summary of Fracture Modes

Material	Tensile Failure Mode	Peel Failure Mode
HSLA	Button pull-out	Button pull-out
590R	Button pull-out	Button pull-out
DP600	Interfacial Failure	Button pull-out
DP780	Button pull-out	Button pull-out
TRIP780	Interfacial Failure	Partial Interfacial

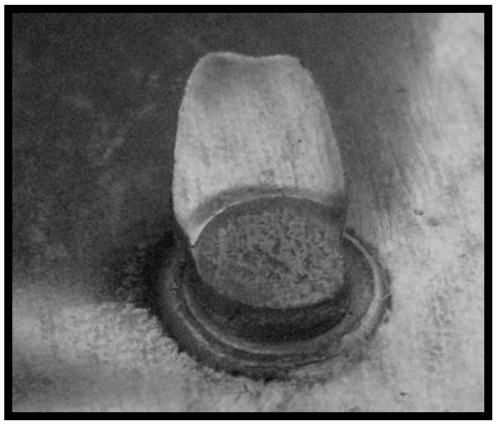

a) HSLA

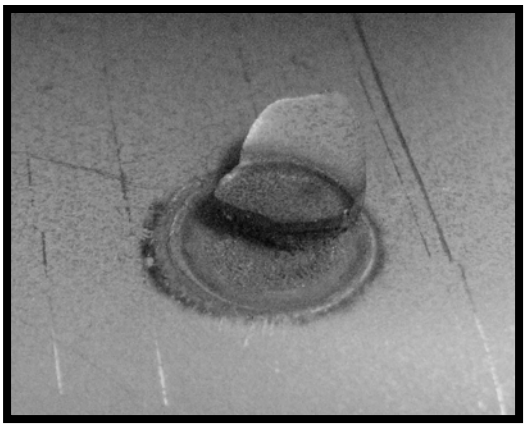

b) TRIP780

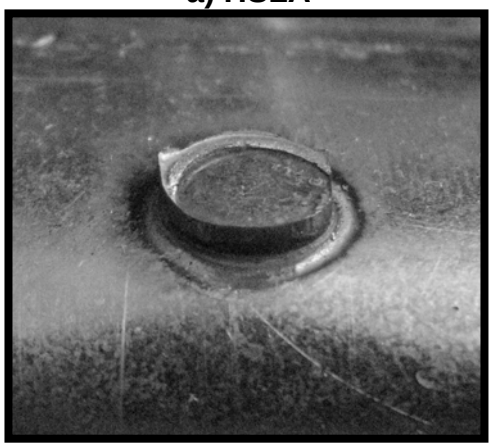

c) DP600

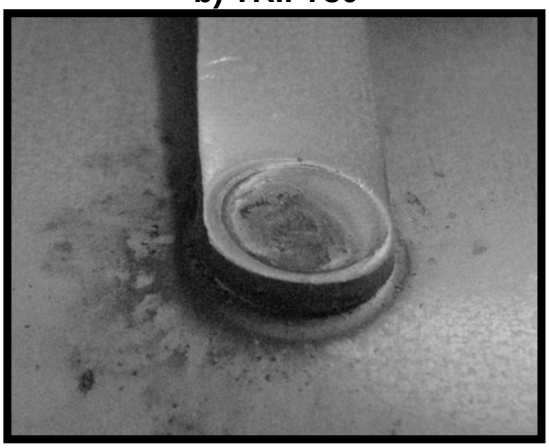

d) DP780

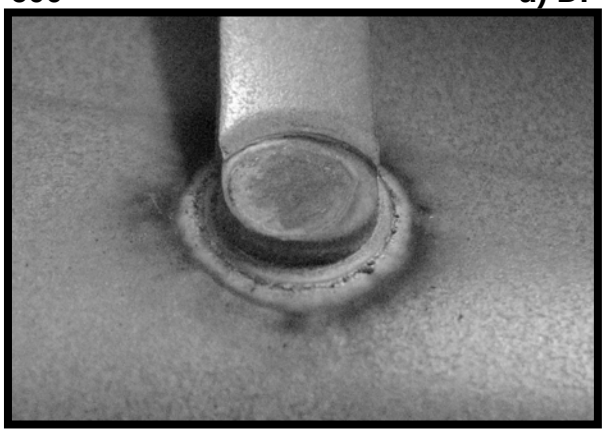

e) 590R

Figure 5.1: Fracture surface for coach peel testing of weldments produced using optimal welding conditions.

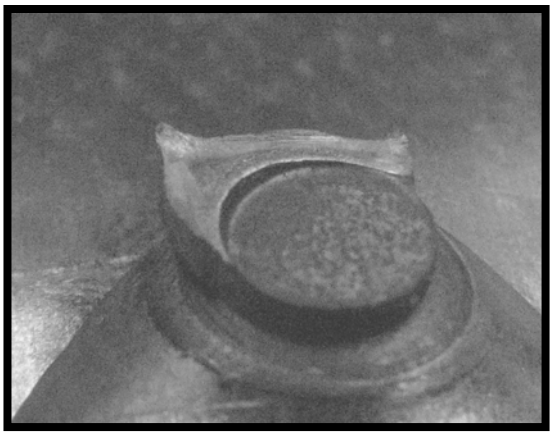

a) HSLA

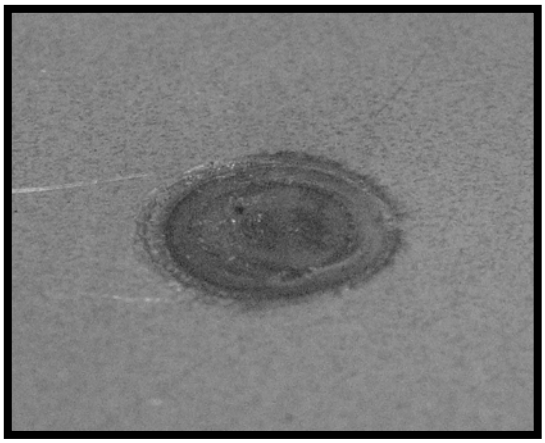

b) TRIP780

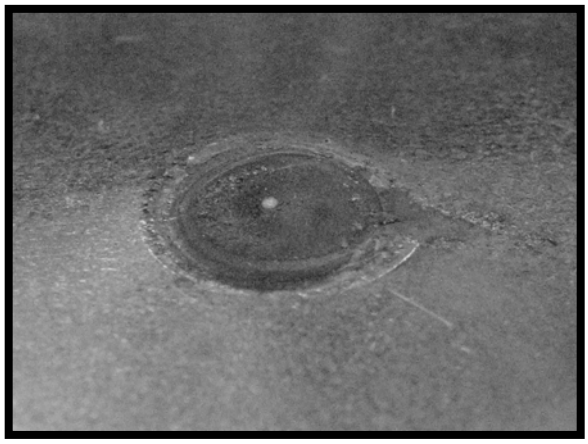

c) DP600

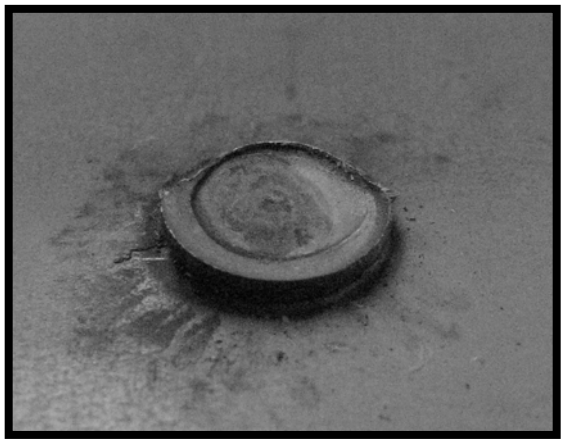

d) DP780

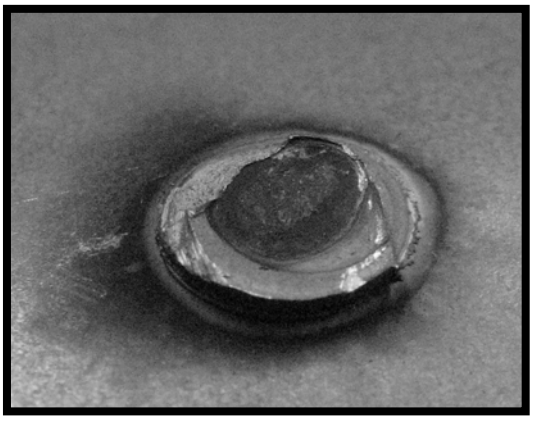

e) 590R

Figure 5.2: Fracture surface for tensile shear testing of weldments produced using optimal welding conditions.

Coach peel testing resulted in full button failure for all tested materials with the exception of TRIP780, which exhibited partial interfacial failure. Closer examination shows crescent shaped HAZ remnance from the joined sheet. Studies have shown inhomogeneity of alloying elements within the fusion zone [70], mainly evident for rich chemistry steels such as TRIP. Segregation of alloying elements during solidification can provide a path for fracture propagation that follows along dendrite boundaries. Partial interfacial failure can occur, leading to significantly reduced button diameters during coach peel testing.

Fracture surfaces for tensile shear test results revealed a combination of interfacial and button pull-out failure modes as shown in Figure 5.2. Button pull-out failure modes occurred for HSLA, DP780 and 590R indicating fracture initiation and propagation occurring either in the BM or within the HAZ. TRIP780 and DP600 produced brittle interfacial failure, indicating fracture initiation at the interface and propagation through the centerline. Khan et al showed the relationship between bonded area and failure loads with occurrence of interfacial fracture [71]. However during button pull-out, material properties and FZ diameter are the main determining factors of spot weld strength.

Figure 5.3 shows failure load as a function of energy input during welding. A second degree polynomial fit was used in order to better display scattered data sets. During lower energy inputs' bonding was nearly achieved while expulsion is narrowly avoided at higher energy values. Failure loads increase with larger energy inputs during welding. HSLA produced the lowest failure loads at a given energy input while DP780 exhibited the highest. Furthermore, DP780 and 590R tend towards a horizontal asymptote with increase in energy input, other material maintains some linearity. This is also reflected in the asymptotic relationship shown in Figure 5.3 for DP780 and 590R. As the energy inputs increase the failure load–energy curve reaches an asymptote where the material surrounding the FZ begins to fail.

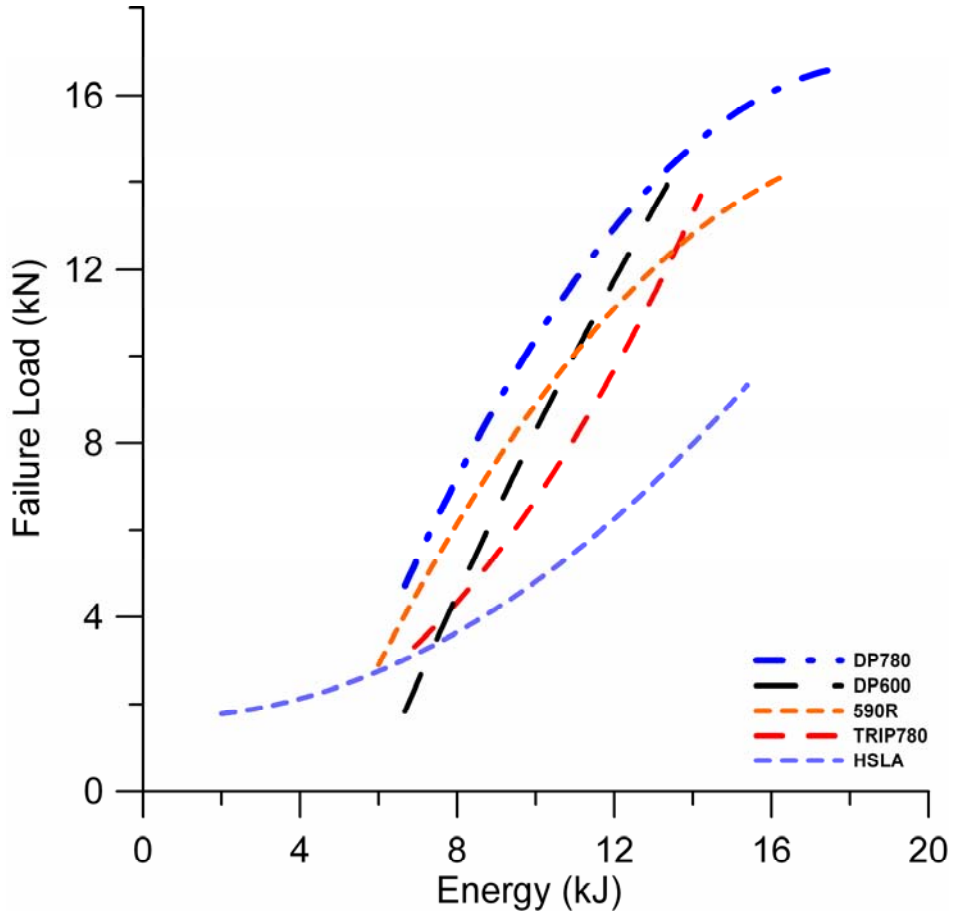

Figure 5.3: Failure Load Vs Energy Input for RSW AHSS

Significant differences in failure modes were observed for the two dual phase alloys tested. DP600 underwent interfacial fracture while DP780 produced a full button. Xia et al shows the effects of HAZ softening occurring for various DP alloys due to post-weld tempering [72]. Higher grade DP exhibit greater potential for HAZ softening due to larger volume fraction of martensite which experiences post-weld tempering. In the current study failure showed to occur near the HAZ for the higher grade DP780 compared to interfacial failure occurring for DP600. BM microstructure for the Dual phase alloys in Figure 4.5 a) and Figure 4.6 a) showed a higher volume fraction of martensite in the DP780 making it more susceptible to HAZ softening. A detailed hardness traces from BM to FZ for the dual phase alloys is shown in Figure 5.4. DP780 exhibited HAZ softening compared to the DP600. Hence tempering of martensite within DP780 resulted

in HAZ failure while the lack of softening in DP600 may have cause brittle interfacial failure to occur.

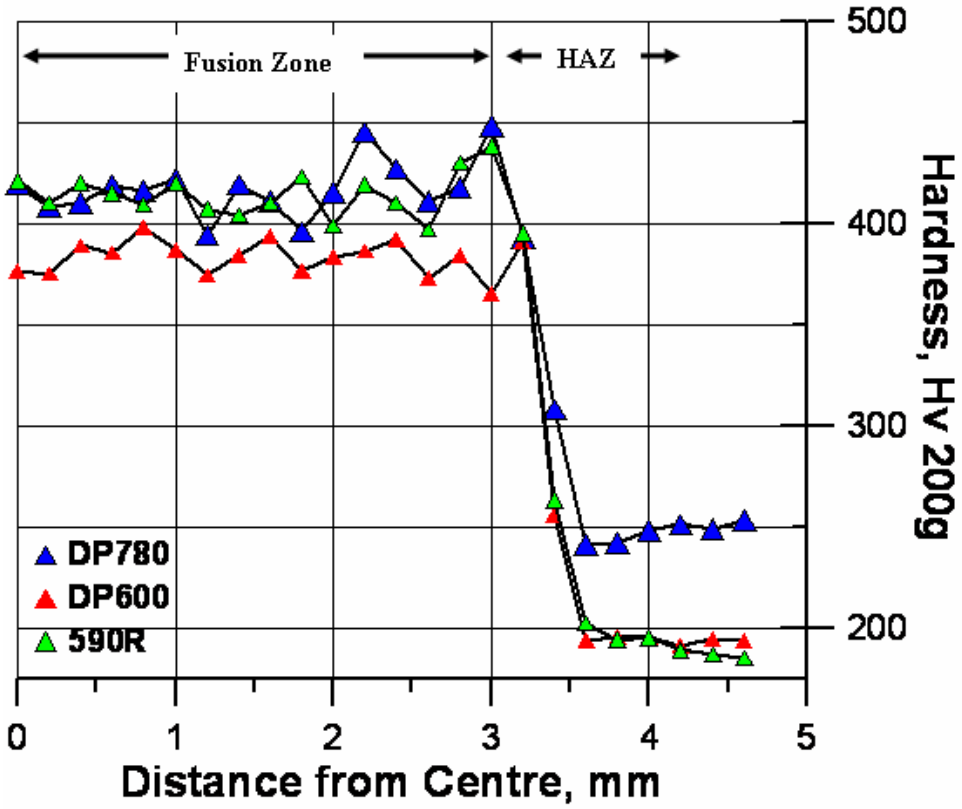

Figure 5.4: Hardness Trace from BM to FZ for DP780, DP600 and 590R

5.2 Impact Testing

5.2.1 Data Analysis

Figure 5.5 shows a representative load vs. displacement curve for DP600 attained at static, intermediate and impact test velocities. An energy trace for the static testing velocities is also plotted. Key parameters from these curves include failure load, displacement at failure and energy absorbed. The amount of energy absorption was digitally calculated by measuring the area under the load-displacement curve up to failure using the following equation.

$$Q = \sum_{n=1}^{N} F(n) \cdot \left(x(n) - x(n-1)\right) \qquad 5.1$$

Where in Equation 5.1, F is Force, x is the displacement, n is the sampled data and N is the peak failure load. Also shown in Figure 5.5 is an increase in failure loads at higher test velocities. Displacement at failure increases between static to intermediate test rates, however there is a considerable drop when transitioning from intermediate to impact velocities. It has been shown that the increase in test rates results in increased flow stress [73]. In turn this would limit deformation of the material surrounding the spot weld. Furthermore it has been speculated that this can increase the peak load of the weldment [74]. Thus, fracture will result at higher peak load with lower overall deformation which can reduce the energy absorbed by the weld.

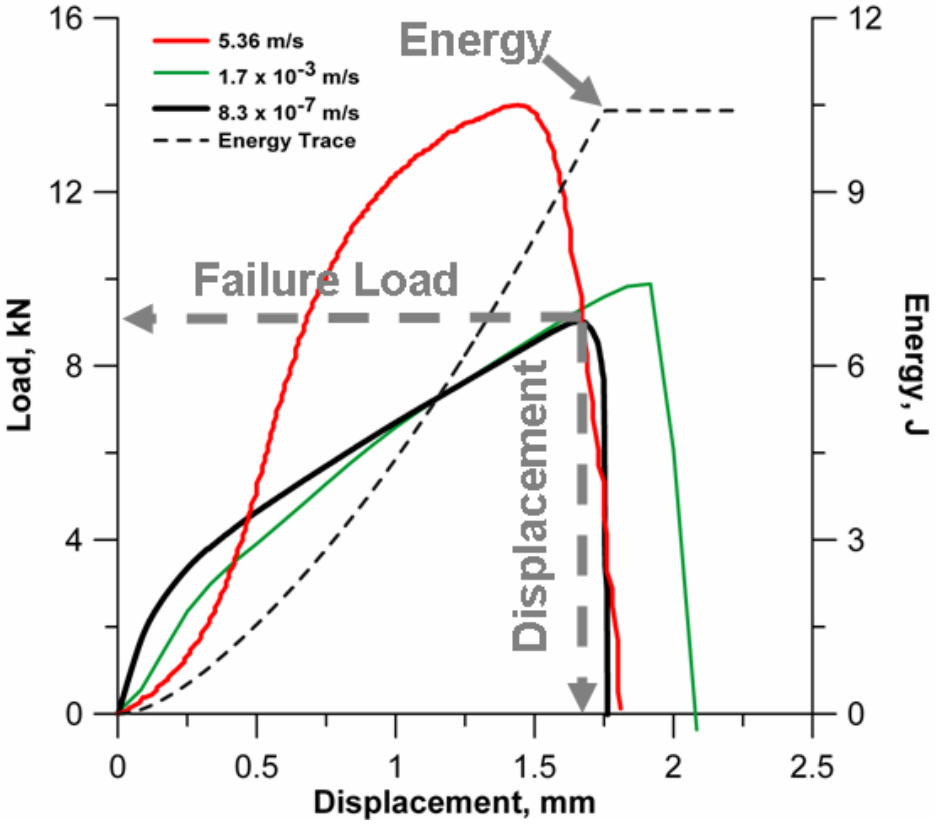

Figure 5.5: Representative load-displacement curve for DP600

5.2.2 Displacement

Elongation to failure load during tensile testing at the different test velocities are shown in Figure 5.6. During the static testing DP600 exhibited the least

displacement while all other materials had relatively similar values. Each material experienced an increase when transitioning from static to intermediate test velocities. TRIP780 shows the greatest change with an increase of about 25% while the DP600 consistently maintains the lowest elongation to failure.

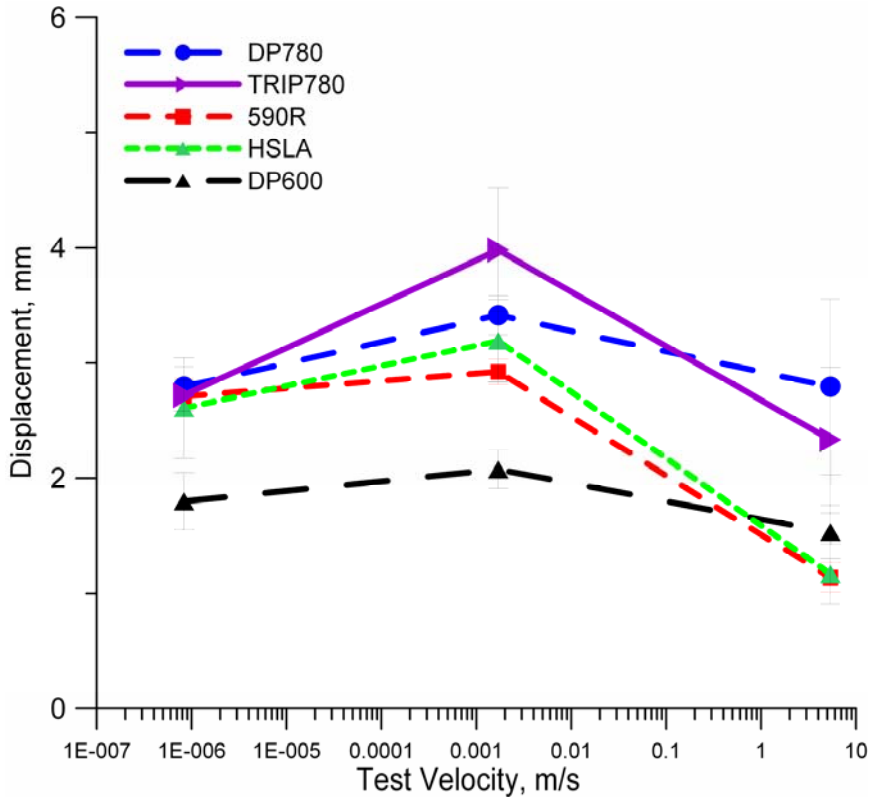

Figure 5.6: Elongation Vs Test Velocity

Results for Impact velocities show a relative decrease in displacement. HSLA and 590R maintain comparable values which reduced about 50% from the intermediate velocity, dropping below the DP600. However displacement values for the DP600 continue to be relatively low. DP780 performs slightly better then TRIP780, attaining the highest values for Impact test velocities.

5.2.3 Energy absorption

Figure 5.7 shows the energy absorption of each material for static, intermediate and impact test velocities. General trends show an increase in energy absorptions when transitioning from static to intermediate test velocities.

However, there is a decrease in energy absorption when changing from intermediate to impact test velocities.

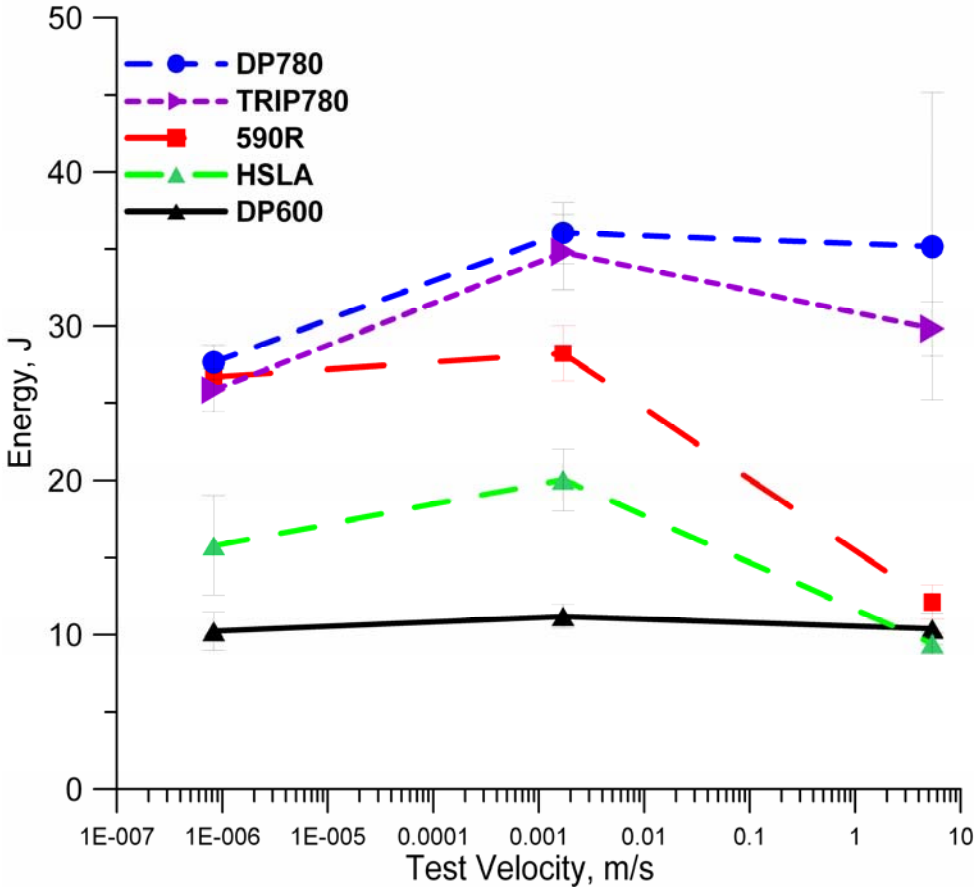

Figure 5.7: Energy Vs Test Velocity

Similar energy absorption values were attained during static testing for TRIP780, 590R and DP780 which are near 27J. HSLA performed relatively poorly with only 15J of energy absorbed. Relative to other materials, the DP600 consistently performed poorly with about 10J of absorbed energy during all three test rates.

Energy absorption values decreased for each material during impact testing. 590R and HSLA showed a considerable decrease. This reflects results observed in Figure 5.6, since a decrease in displacement can adversely affect energy absorption. Both materials attained similar values which were close to the poorly performing DP600. DP780 achieved highest energy absorption at impact, followed by TRIP780.

5.2.4 Failure Loads

Each material tested produced higher failure load with increasing test velocity. Similar results have been reported for spot welded HSLA [75]. TRIP780, 590R and DP780 perform relatively well and maintain comparable failure loads through all three test rates. During static and intermediate test velocities the DP600 and HSLA have similar failure loads which are near 9kN. At impact velocities failure loads for HSLA are around 18kN, slightly outperforming the DP600. Furthermore it should be noted that failure loads produced by 590R do not reflect the poor performance from energy absorption and displacement results which were observed in Figure 5.6 and Figure 5.7

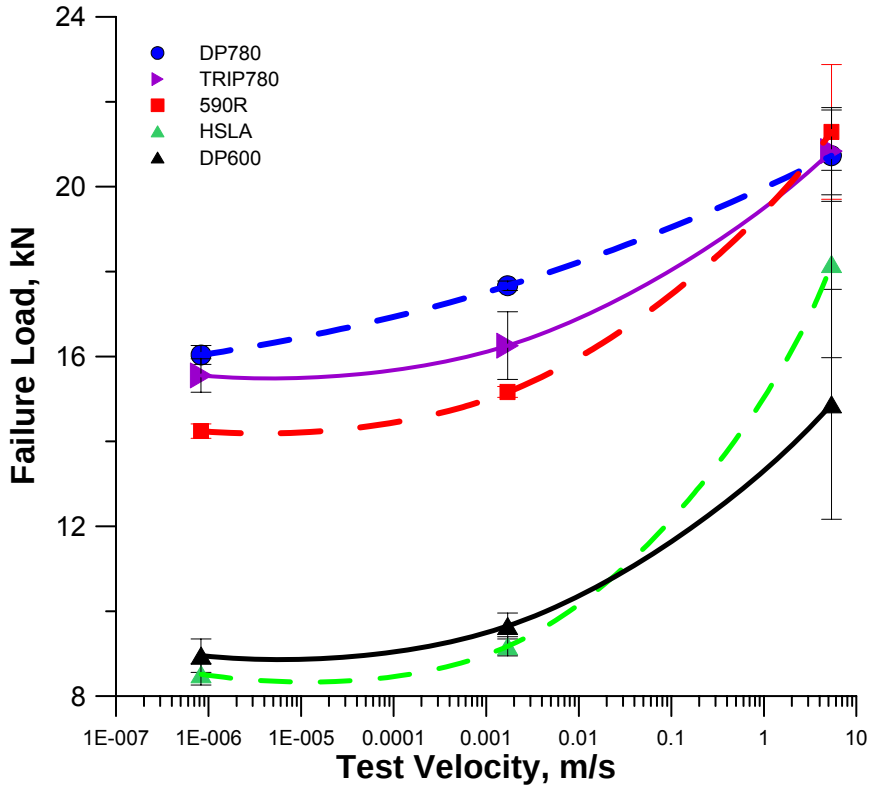

Figure 5.8: Failure Load Vs Test Velocity

5.3 Impact Fracture Surfaces and Detailed Examination

5.3.1 HSLA

Fracture surfaces for the HSLA are shown in Figure 5.9. Partial interfacial failure modes can observed for all three test velocities shown in Figure 5.9 a)-c). Figure 5.9d) shows the cross-section for the static partial tensile test. Fracture initiates at interface of the two materials and propagates towards the FZ. By observing the detached upper sheet, remains of the fusion can be seen, suggesting fracture propagated through the fusion zone material. The base metal material shows little evidence of plastic deformation.

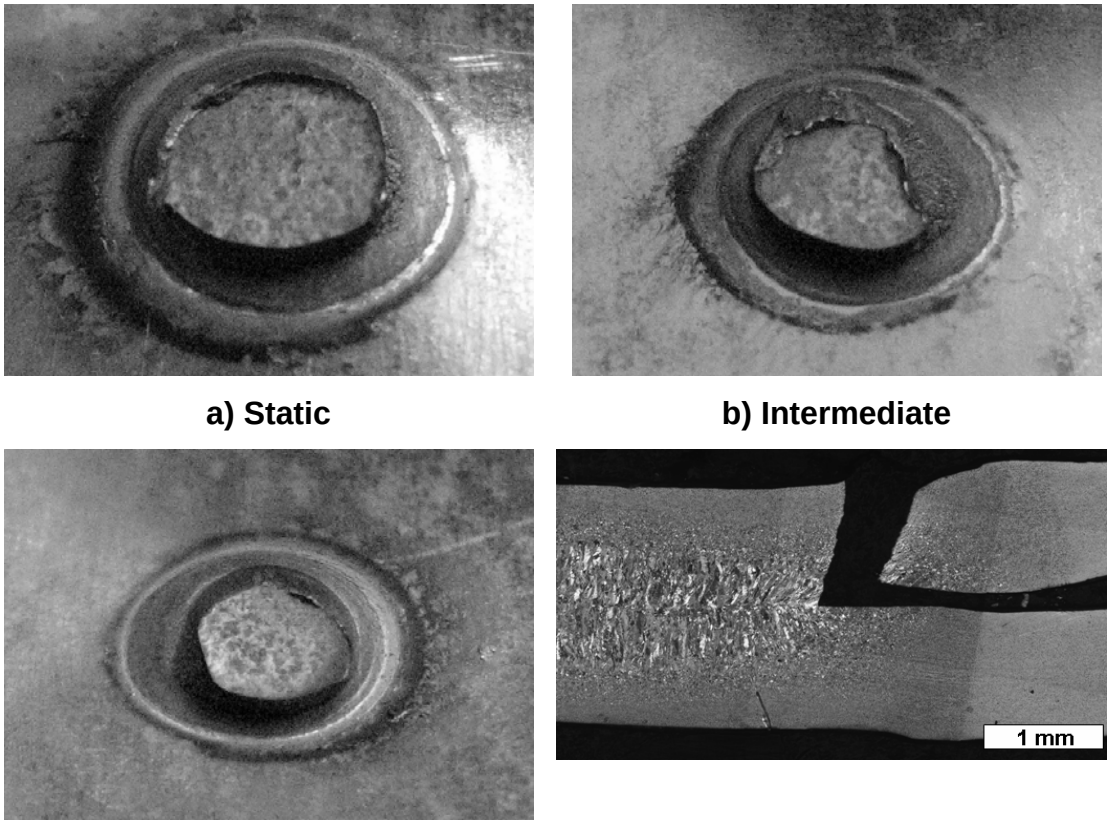

a) Static **b) Intermediate**

c) Impact **d) Static partial-tensile**

Figure 5.9: Fracture Surface of HSLA

5.3.2 590R

Figure 5.10 a) and b) show button pull-out fracture modes during static and intermediate test velocities of 590R. Crescent-shaped remains of the upper sheet material remain around the weld. Tearing of the surrounding material can be observed when the weld is subjected to impact test velocities. Cross-section of interrupted static tensile testing is shown in Figure 5.10d). Failure occurring outside of the HAZ, in the BM. Necking due to plastic deformation is also evident near the fracture.

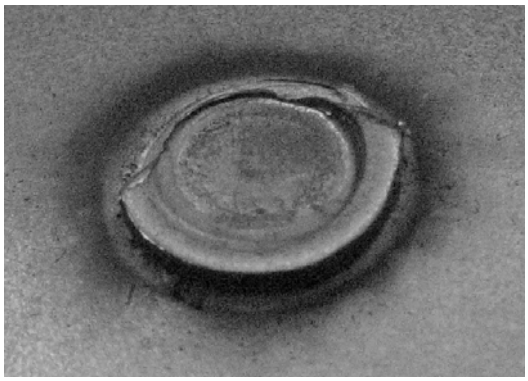

a) Static

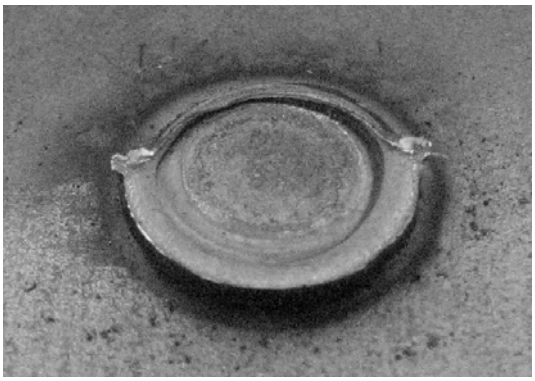

b) Intermediate

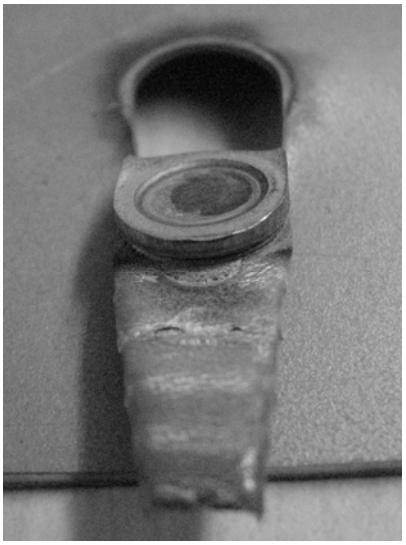

c) Impact

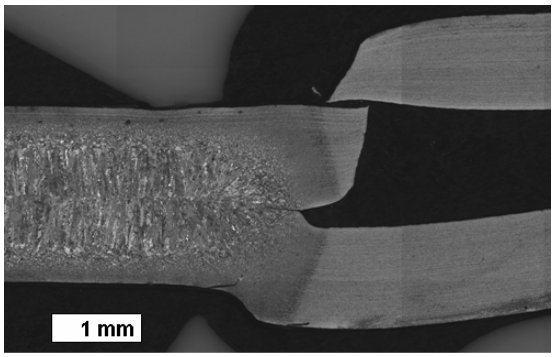

d) Fracture Cross-section

Figure 5.10: Fracture surface for 590R

Tearing observed during fracture analysis is reflected in the load displacement curve beyond the peak load shown in Figure 5.11. Methods used to attain energy absorption and displacements only account for loading until failure. However, it can be clearly shown that after surpassing the peak load there is some fluctuation in load which is caused by tearing of the surrounding material. An increase in energy absorbed can be attained if the total area under the load displacement curve is calculated for the impact test velocity. Furthermore the 590R achieved comparable failure loads to DP780 and TRIP780, which consistently outperformed the other materials.

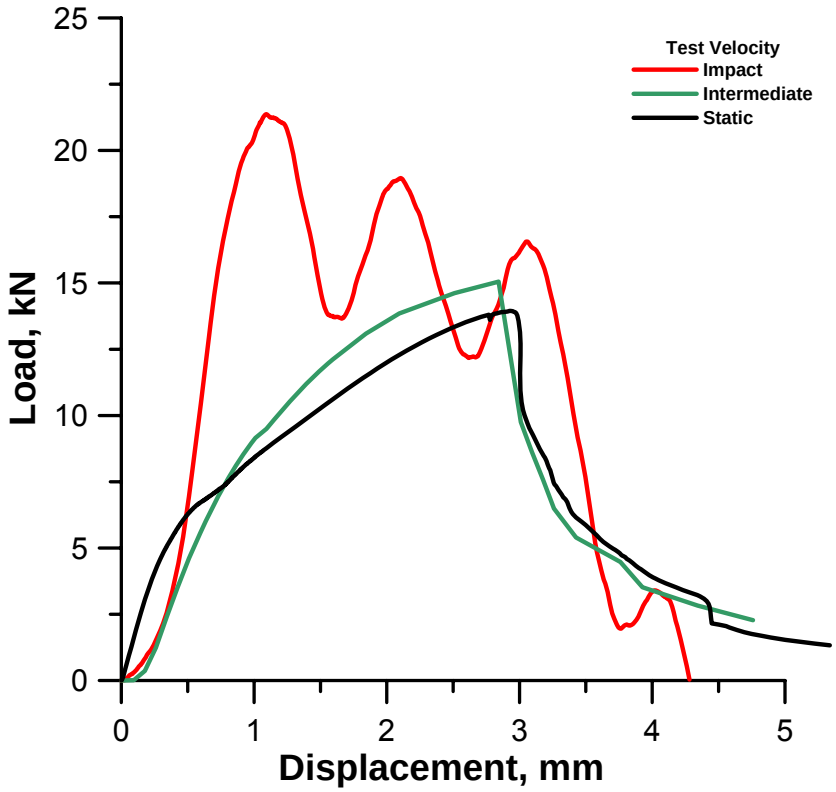

Figure 5.11: Load-displacement curve for 590R

5.3.3 DP600

Figure 5.12 a)-c) shows the fracture surfaces of spot welded DP600. Brittle interfacial failure can be observed for all three test velocities. Figure 5.12 d) shows the cross-section for the partial tensile sample tested at the static test

velocity. Fracture initiates at the interface of the two materials and propagated through the HAZ towards the FZ. Further loading would propagate the fracture through the FZ centerline, resulting in full interfacial failure.

The consistently poor results observed with DP600 can potentially be avoided with the use of pulsing [76]. It has shown that pulsing can be used for in-situ heat treatment of the weld material. This can modify the microstructure within the weldments and possibly improved mechanical properties including impact performance.

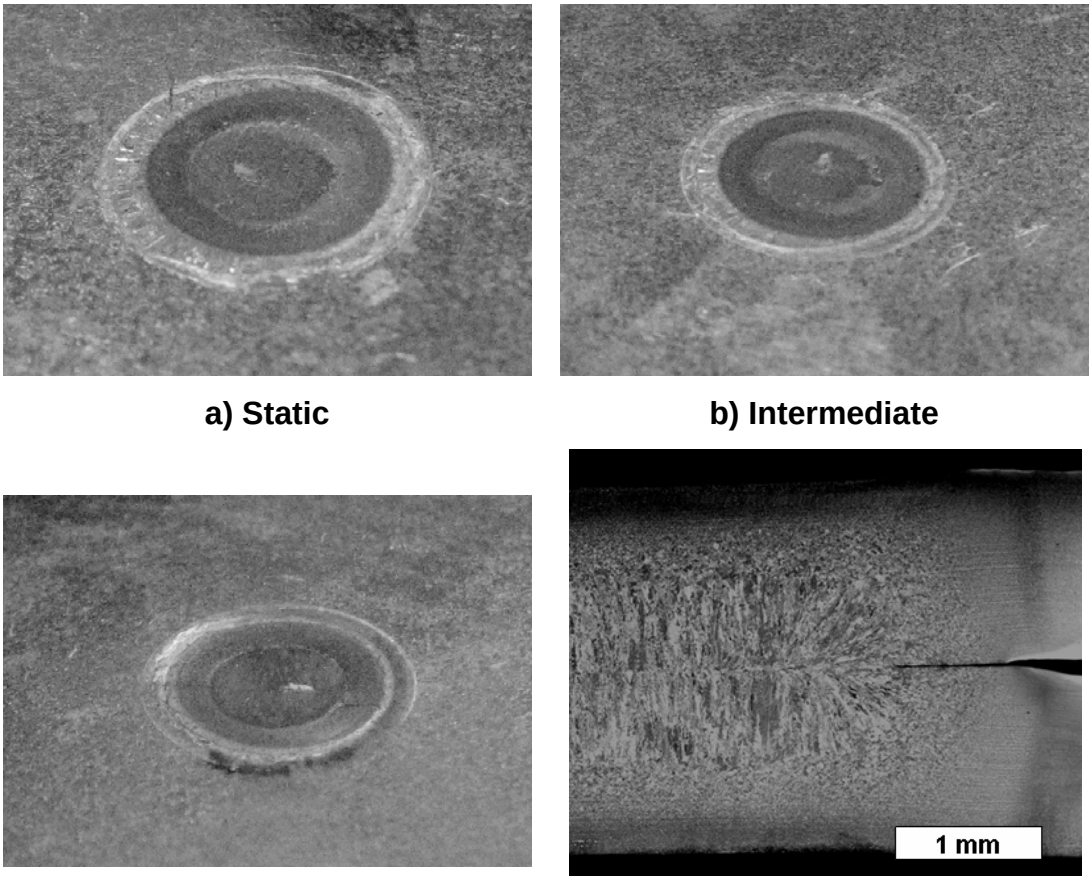

a) Static **b) Intermediate**

c) Impact **d) Fracture Cross-section**

Figure 5.12: Fracture surface for DP600

5.3.4 DP780

Figure 5.13 a)-c) shows the fracture surfaces of DP780 for all three test velocities. Button pull-out failure modes were observed during static and intermediate test rates with remains of HAZ material surrounding the FZ. However during impact testing there is full separation of the nugget from the welded sheets. After each impact test three components would remain in the drop-chamber including the two welded coupons and a fully separated nugget.

By examining the cross-section for a partial tensile sample, Figure 5.13 d), it can seen that fracture occurs near the HAZ and propagated through the base metal. Furthermore localized necking occurs in BM of the upper sheet which indicated localized plastic deformation.

a) Static

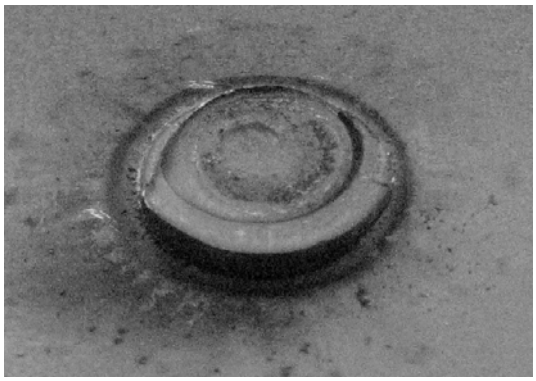

b) Intermediate

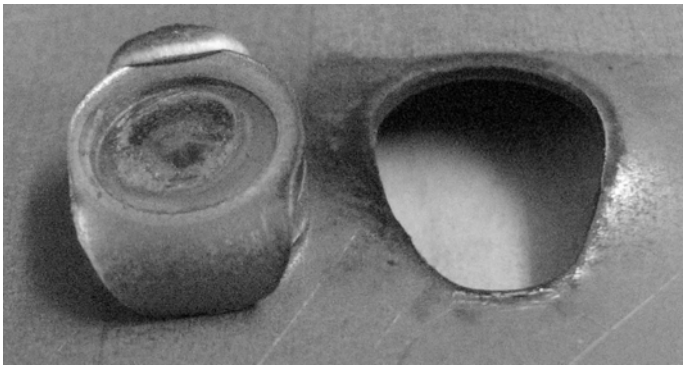

c) Impact

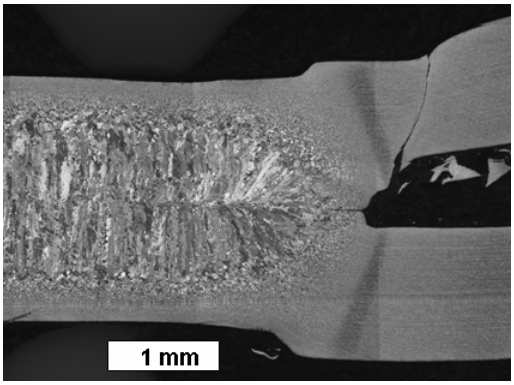

d) Fracture Cross-section

Figure 5.13: Fracture surface for DP780

HAZ softening is a long noted issue when welding DP steels and has been cited for early failure in DP steels [77]. It has been shown that post weld tempering of martensite near the HAZ results in the local softened region. Materials which exhibit higher concentration of martensite are relatively more susceptible to HAZ softening. As mentioned earlier, compared to the DP600, the base material of this particular DP780 contained larger volume fractions of BM martensite and richer chemistries making it more susceptible to HAZ softening Figure 5.4. The DP600 consistently produced brittle interfacial failure resulting in poor impact performance. DP780 on the other hand consistently produced full button failure modes and achieved one of the best impact performance results. Hence, the inherent nature of DP softening, in particular for material containing higher volume fraction of martensite, can possibly aid in improving Impact performance.

5.3.5 TRIP

Fracture surfaces for the TRIP780 spot welds are shown in Figure 5.14 a)-d). Partial interfacial failure can be observed for all three test velocities with no evidence of HAZ remains around the FZ. Figure 5.14 d) shows the cross-section for the static partial tensile shear test. Fracture initiates near the sheet interface and propagated through the FZ going through the HAZ.

It has been shown that rich chemistries inherent to TRIP780 production can result in segregation of some alloying elements during weld solidification [78]. During loading segregation provides preferred paths for fracture propagation within the FZ. Since the TRIP tested in this particular study consisted of relatively high chemistries, it is possible that segregation may have occurred during solidification which resulted in fracture propagating through the FZ. Furthermore Uijl et al. suggested using a second current pulse which can heat treat the weld metal, resulting in a more ductile button failure mode. However, TRIP780 and DP780 exhibited the best impact performance relative to all other materials tested.

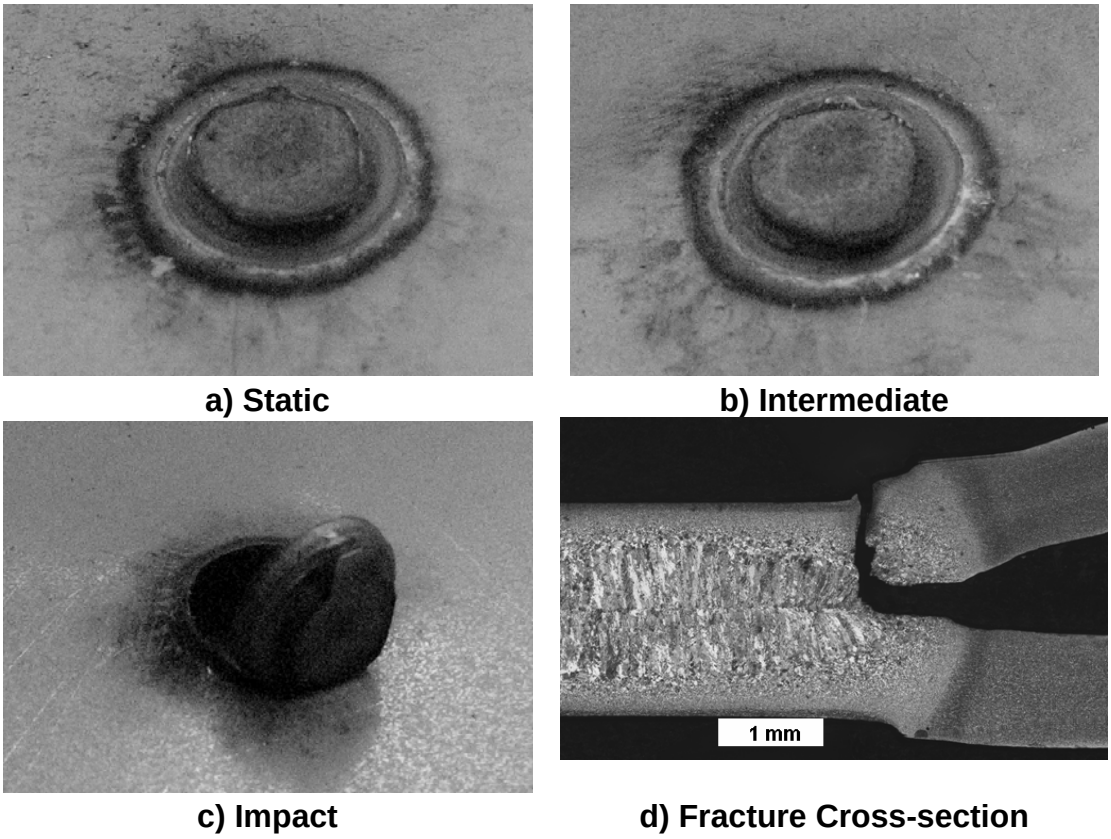

Figure 5.14: Fracture surface of TRIP 780

5.3.6 Summary

In this chapter the fracture surface and impact performance of spot welded AHSS and HSS were examined. Quasi-static and impact tests were conducted using a typical tensile tester and an instrumented drop tower, respectively. Results for elongation, failure load and energy absorption for each material are presented. Failure modes are detailed by observing weld fracture surfaces. Cross-sections of partially fractured weldments were examined to detail fracture paths during static loading. It was possible to develop a correlation between the fracture path and mechanical properties using observed microstructures in the fusion zone and heat-affected-zone.

CHAPTER 6: COMPARISON OF RESISTANCE AND FRICTION STIR SPOT WELDING

6.1 Resistance Spot Welding

A representative RSW weld cross-section is shown in Figure 1.1(8kA, 3.5kN, 20cycles). The fusion zone (FZ), heat affected zone (HAZ) and base metal (BM) can be clearly observed. Microstructural observations of these regions are shown in Figure 1.1 a) to d). A hardness profile of the weld region is shown in Figure 4.10. This profile shows the hardness in the BM, HAZ, and FZ regions.

The BM in Figure 1.1a) shows the typical finely dispersed martensite particles (white) surrounded by a ferrite matrix (fawn) that are characteristic of the automotive dual-phase steels. Peak temperatures during welding in this region are typically below the martensite tempering temperature (i.e. less than 200°C). Hardness values in the BM range from 150-200 HV, which is an indication of the mainly ferritic nature of the microstructure.

In the HAZ, the volume fraction of martensite increased. The peak temperature during welding in this region ranges from martensite tempering temperatures to just below the liquidus. Figure 1.1 b) shows a transitional region from the intercritical (IC) to the fine grained region (FG) within the HAZ. Peak temperatures in the IC region are between the Ac1 and Ac3, resulting in a coarsening of the martensite phase. Within the FG region, temperatures exceed the Ac_3 resulting in complete austenitization. The austenite is inhomogenous due to the nature of segregation within the DP microstructure and short time above Ac_3; resulting in the banding nature of martensite and the formation of fine grained ferrite. Hardness values in this area exceed that of the BM, 230 to 280 HV, which indicates an increase in the volume fraction of martensite with a ferrite matrix.

Within the HAZ, the peak temperature is well above Ac_3, resulting in complete austenitization and grain growth. The grain coarsened (GC) region consists of prior austenite grains about 10-15 μm in diameter. The microstructure in the GC region is blocky martensite, as shown in Figure 1.1c), with a hardness in excess of 350 HV (Figure 4.10).

The FZ shown in Figure 1.1d) is characterized by the columnar nature of solidification. The microstructure consists of large equiaxed columnar martensite grains. From figure 5 we can see hardness values similar to the HAZ region, ranging above 350 HV.

6.2 Friction Stir Spot Welding

Figure 6.1 shows the microstructural features observed at different locations relative to the keyhole centerline in a FSSW spot weld in DP600 sheet. The BM was similar to the RSW case, with martensite islands in a ferrite matrix with a hardness up to 200 HV. The IC region of the HAZ, shown in Figure 6.1 b) is significantly wider than the RSW case due to the longer weld times. The hardness in this region was about 220 HV, as shown in Figure 6.2.

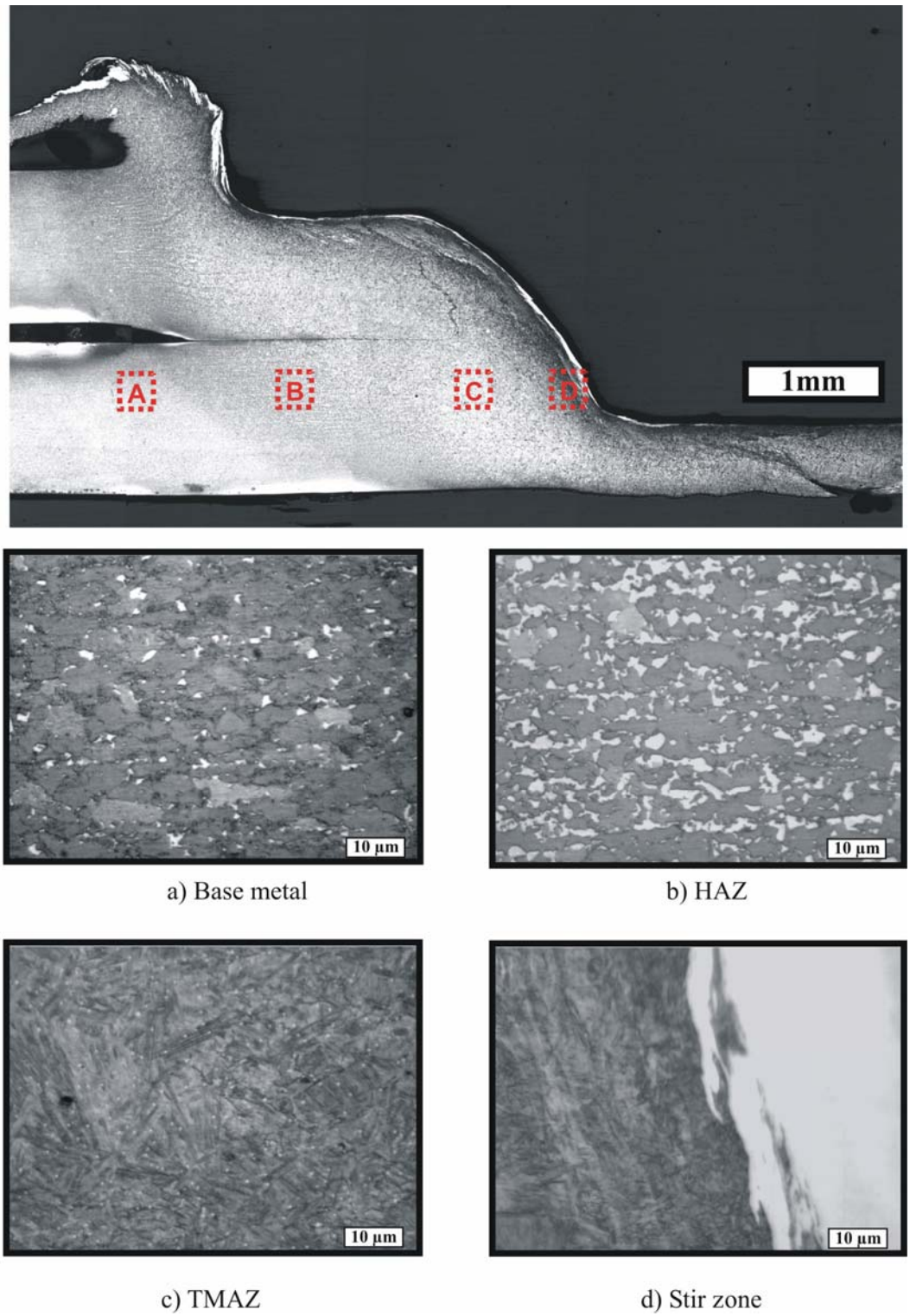

a) Base metal

b) HAZ

c) TMAZ

d) Stir zone

Figure 6.1: Microstructure for different weld sites in FSSW

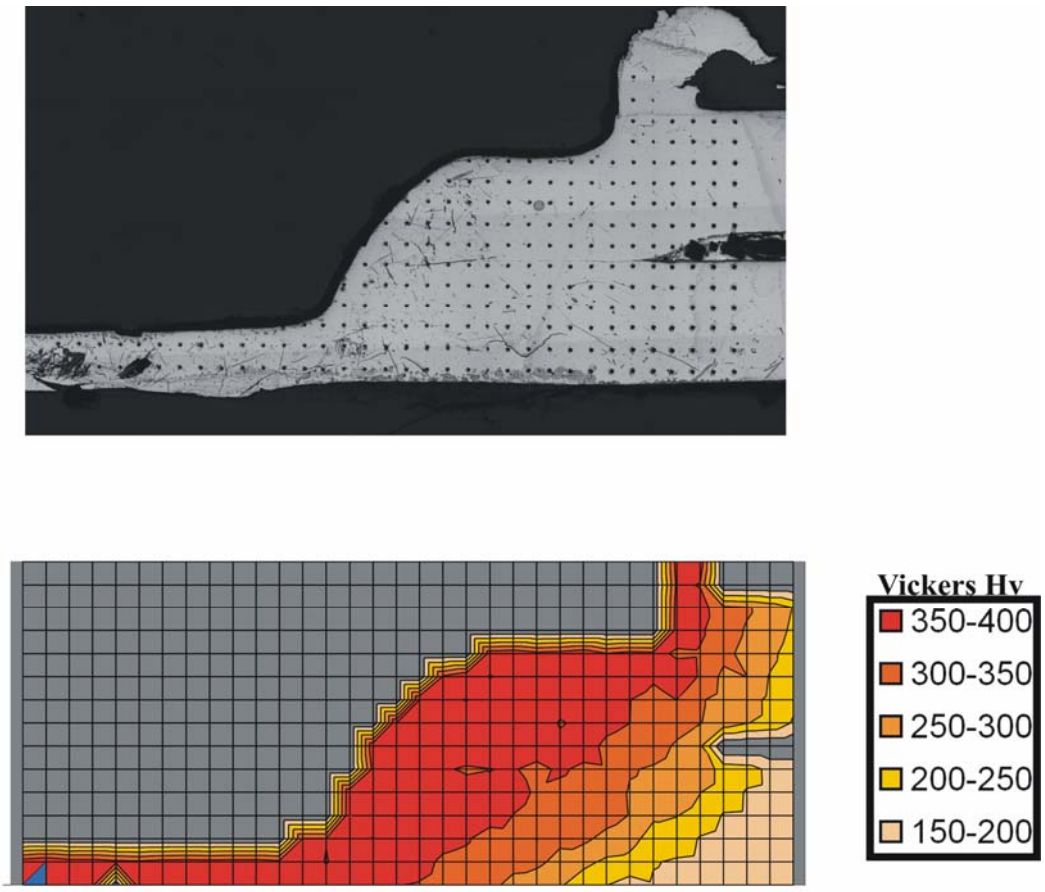

Figure 6.2: Microhardness maps of FSSW cross-section

Beyond the HAZ and towards the keyhole, in the thermo-mechanical heat-affected zone (TMAZ) region the microstructure is comprised of a mixture of lath martensite and fine acicular ferrite, shown in Figure 6.1c). This region is subject to temperatures above Ac_3 and high strain rates, resulting in dynamic recrystallization and grain growth. The prior austenite grain size in this location was markedly increased. The hardness in the TMAZ was about 300 HV, see Figure 6.2. In addition to the lathy martensitic microstructure, fine particles or rods of martensite which are less than 1 μm in diameter are observed, which will be the subject of further communications.

Immediately adjacent to the keyhole periphery the stir zone microstructure is comprised of very fine-grain martentsite that could not be resolved using optical microscopy, see Figure 6.1 d). The grain size in the stir zone of friction stir spot

welds are typically less than 10 μm in friction stir spot welds [79]. The hardness in this particular location was about 350 HV, as shown in Figure 6.2.

The top surface of the FSSW welds shows a poor finish with a keyhole resulting from the pin, and an indentation surrounded by expulsion, or debris, caused by the tool shoulder. Discoloration of the surface is a result of oxidation; however, this may be prevented by Ar shielding if desired. Figure 6.5 (b) shows a typical surface for FSSW. Compared to FSSW, the typical surface appearance for RSW is considered more acceptable for automotive applications. As shown in Figure 6.5(a) the surface is smooth with a slight indentation and discoloration of the galvanized coating resulting from the thermal effects of the welding process.

6.3 Tensile Shear Testing

Cross sections of partial tensile shear test specimens can be used to observe failure propagation. Figure 6.3 shows a partially failed tensile shear test result for a RSW sample welded under the condition of 8 kA current, 3.5 kN force and 20 cycle weld time. The fracture extends from the faying surface interface at the fusion boundary into the fusion zone along the weld centerline. Figure 6.4 shows an FSSW cross-section along the side where crack initiation occurs for partial tensile test specimen. This weld was produced under optimal welding condition (3000 rpm, 2.1mm penetration, 0.5 mm/s plunge rate). The fracture initiates from the tip of the unbonded interface, and propagates through the stir zone in the upper sheet.

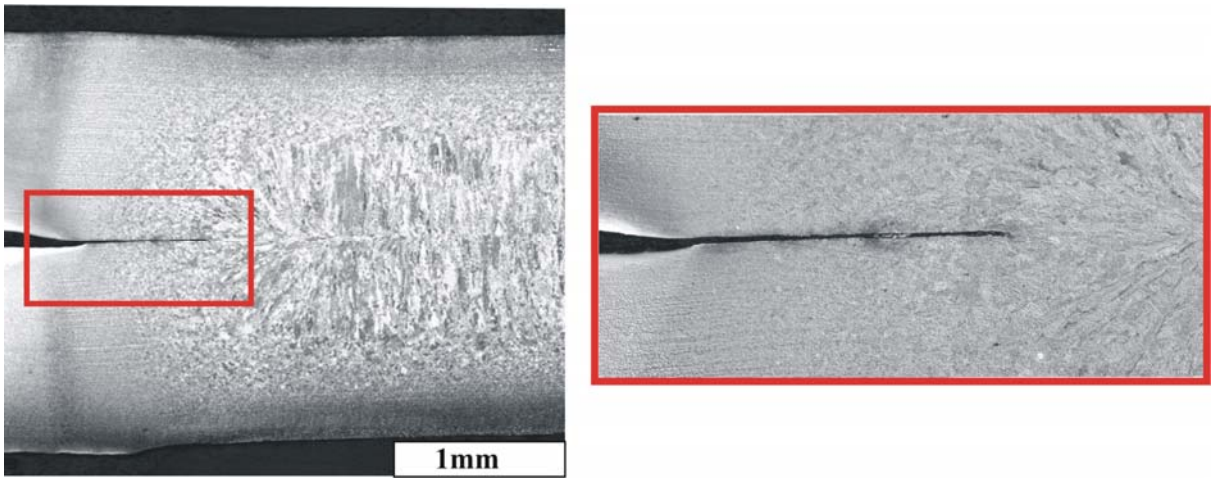

Figure 6.3: Partial tensile of RSW cross-section

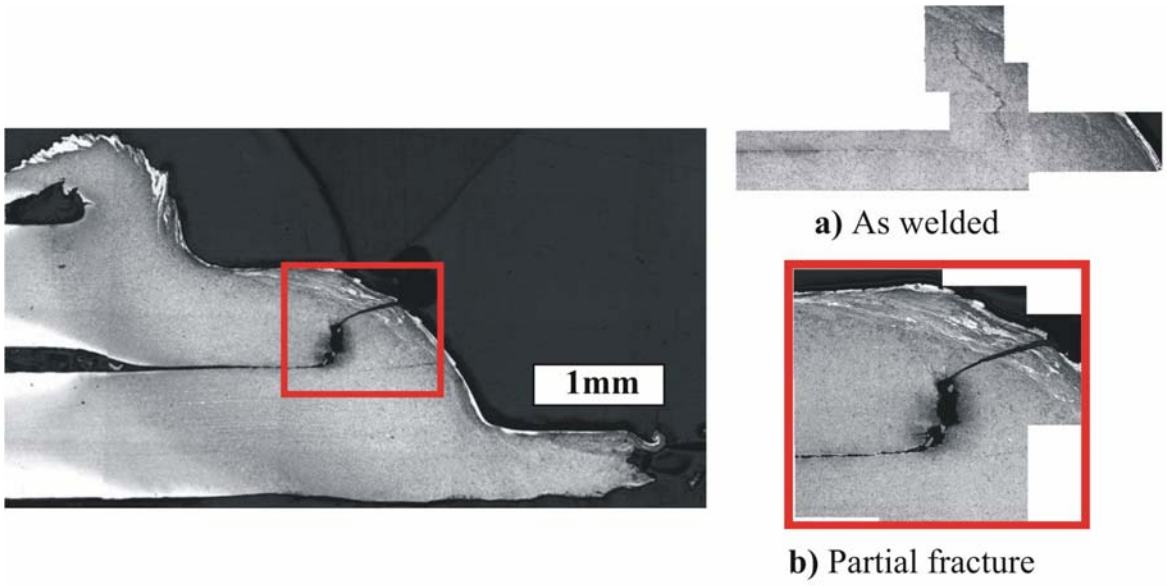

Figure 6.4: Partial tensile of FSSW cross-section

Figure 6.5 (c-f) shows the fracture surfaces produced in failed overlap shear testing specimens made using high and low energy input values. Low and high energy inputs produced an interfacial fracture through the fusion zone of the resistance spot weld, see Figure 6.5 (c,e). When a low energy input was applied during FSSW the welded joint failed across the weld zone at the interface of the two sheets**.** When high energy inputs were applied the mode of failure involved a partial pull-out, see Figure 6.5(f). There was no change in failure mechanism observed with changes in heat input.

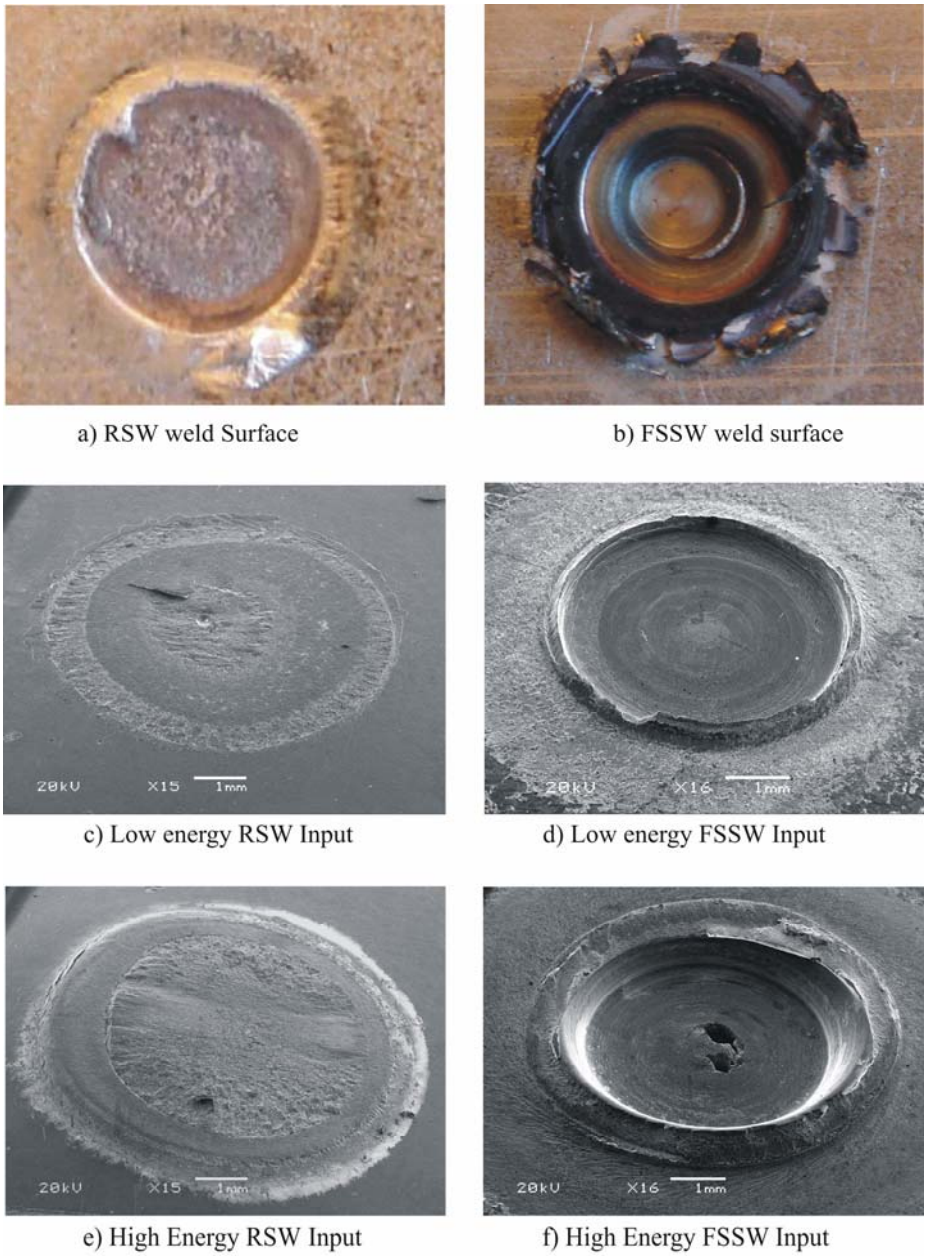

Figure 6.5: Weld and fracture surface for RSW and FSSW welds

6.4 Microstructure and Hardness

The microstructure and hardness in the weld regions of both RSW and FSSW had similar microstructural features. The IC and FG regions of the HAZ consist of a mixture of martensite and ferrite. The hardness in these regions reaches up to 280 HV.

The FSSW weld contains unique regions that are not found in the RSW case. The RSW weld microstructure shows a CG region adjacent to the fusion boundary. The microstructure is predominately martensite as indicated by the high hardness values (350 HV). The FSSW weld microstructure contains a region termed the TMAZ adjacent to the HAZ. This region consists of a mixture of hard martensite rods, lathy martensite, and bainite or acicular ferrite. The hardness in this region is 300 HV, slightly lower than the CG region in the HAZ due to the microstructure mixture. In both the TMAZ of FSSW and CG regions of the RSW welds, respectively, the prior austenite grain size is large.
The FZ in the RSW weld consists of a hard martensitic columnar microstructure in excess of 350 HV. This compares well to the fine grained FSSW stir zone microstructure hardness of 350 HV.

There is a gradual transition in hardness from the stir zone through the TMAZ and into the HAZ of the FSSW weld (Figure 6.2). The hardness gradient is much steeper in the RSW weld as a result of the smaller HAZ size (Figure 4.10). The heat input for the FSSW process is higher than the RSW process, resulting in a HAZ that is significantly larger than the RSW weld. The hardness gradient and size of the HAZ does not show any effect on weld tensile properties at low strain rates.

The keyhole produced by the stir tool decreases the bonded area for a given weld size. This necessitates a comparison of the weld size based on bonded area rather than weld diameter. The bonded area as a function of total weld energy is shown in Figure 6.8. There is a clearly increasing trend in weld area with increasing weld energy. Furthermore, the ratio of weld area to total energy is similar for both the RSW and FSSW processes. This shows that the weld efficiency of both processes is similar.

6.5 Fracture Analysis and Mechanical Properties

Taking into account the unbonded region located near the TMAZ, both FSSW are RSW welds are bonded with a zone consisting predominately of martensite, having hardness values ranging above 350Hv. Partial tensile results from Figure 6.3 and Figure 6.4 show the location of fracture initiation within the weld. From Figure 6.3 the fracture for RSW welds initiates at the interface and continues through the coarse grain region towards the centerline structure. This sequence indicates fracture occurring through a brittle median. A similar brittle path is followed with FSSW welds where the crack initiates at the tip of the unbonded region and propagates through the stirzone under the shoulder, see Figure 6.4 (a and b).

Figure 6.6 shows the relation between the failure load during overlap shear testing and the bonded area in completed welds. The failure load increased when the bonded area increased for both processes. Similar test output has been found during FSSW of both Al-alloy and Mg-alloy sheet materials [79]. This indicates similar material properties in terms of tensile strength and hardness within the stir zone and FZ for FSSW and RSW welds, respectively.

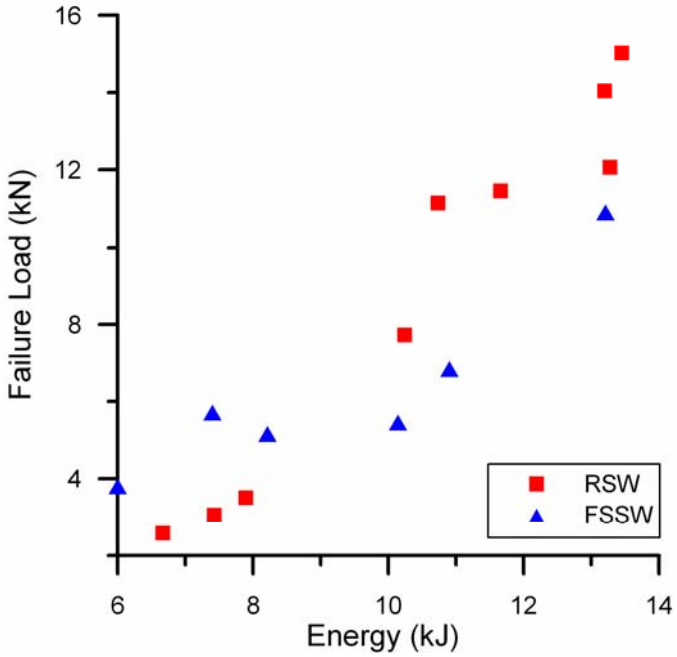

Figure 6.6: Failure load Vs total energy

Figure 6.7 shows the relation between energy input during FSSW and the failure load during overlap shear testing. Higher failure loads were produced when the energy input during spot welding increased. In this connection, it is worth noting the parallel relationship of energy input and failure load between the two welding processes. Difference in bonded area of fracture surfaces of high and low energy welds are shown in Figure 6.5 (c,e). FSSW welds produced both pull-out and interfacial fracture for high and low energy input welds.

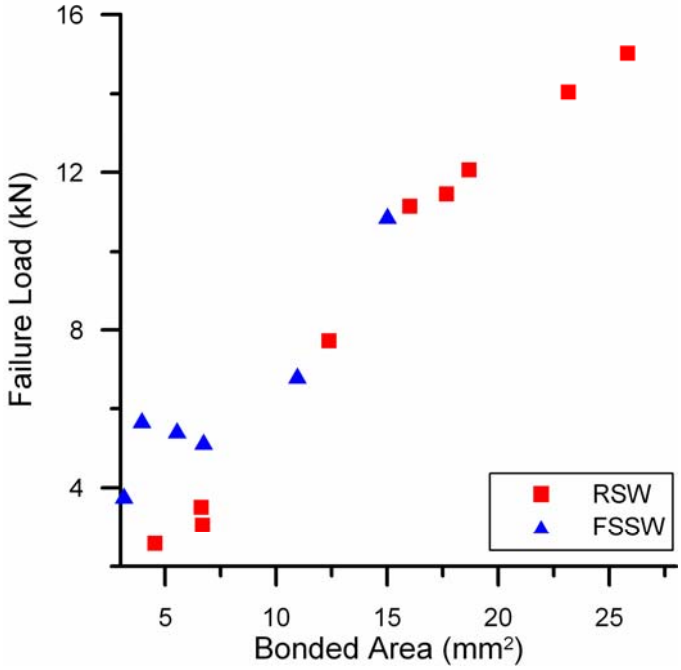

Figure 6.7: Failure load Vs bonded area

The bonded area seems to provide a reasonable basis for comparing the RSW and FSSW outputs, see Figure 6.6. A similar trend is observed between RSW and FSSW welds. Peak failure loads of 15kN and 11kN were obtained for RSW and FSSW welds respectively. Due to the geometry of the unbonded regions failure loads are greater for RSW welds. Energy requirements also show a comparable trend, see Figure 6.7. RSW welds show a relatively linear relationship with energy and failure loads. With lower energy input FSSW welds show a non-linear relationship. This is likely due to the change from only pin penetration to a combination of pin and shoulder penetration. Higher failure load energy inputs are relatively similar to RSW energy inputs.

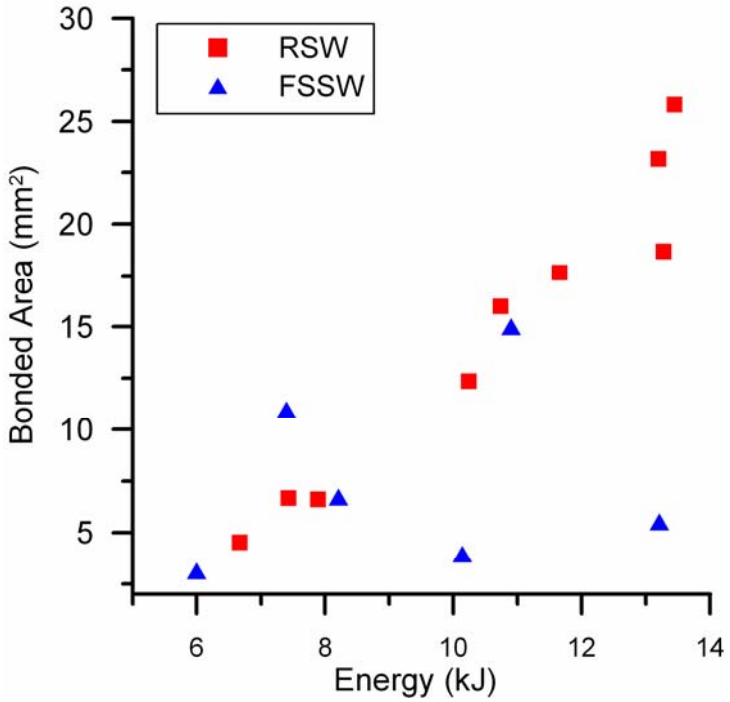

Figure 6.8: Bonded area Vs energy

6.6 Additional Factors

Aesthetically, the surface finish of welds produced using RSW are superior to those produced using FSSW. In some automotive application the smooth surface finish produced by RSW is desired, and the FSSW keyhole would be considered unacceptable. Recent advancements in tool design have produced a retractable pin tool (RPT) which refills the remaining keyhole without affecting the mechanical properties of the spot weld [80]. This, however, increases the cost and complexity of FSSW equipment. Discoloration of spot welds in steel is not considered a problem because the surface is typically finished by painting. If required, oxidation of the surface in FSSW can be prevented by adequate shielding using inert gas, but this too increases the cost of the process.

Prevention of galvanic corrosion for this particular sheet of DP600 is facilitated with a hot dip galvanized zinc coating. Studies have shown during RSW of Zn-coated steel annular zinc braze forms at the faying surface around the fusion zone [81]. Furthermore during the first two cycles of welding the molten Zn-

coating is pushed away from the fusion zone [82]. The mechanical nature of FSSW limits interference of Zn-coatings during FSSW. Previous studies show the peak temperatures reaching 0.9Tm of the base metal [83,14], which in the case for DP600 is well above the melting temperature of Zinc. Figure 6.5 (c,d) shows evidence of an annular braze forming around the RSW and FSSW weld.

The effect of the zinc coating on the RSW process is known to significantly reduce electrode contact tip life. Studies have shown that electrode degradation may be delayed through the use of conductive coatings that prevent alloying between the copper electrode and zinc coating [84]. The net result of the zinc coating is an increase in consumable cost. The FSSW process does not appear to be affected by this as there are no studies to show an observable effect of the zinc coating on tool wear.

Results from the energy calculations show that energy consumption is similar for both processes. Faster cycle times in RSW result in a greater productivity than FSSW. Due to the widespread implementation of RSW, the infrastructure and support system is already in place. The FSSW process is not yet used extensively in the automotive industry, and as a result the infrastructure and support is not yet in place. Furthermore the FSSW process requires additional fixtures due to its mechanical nature. At the moment RSW is a more cost effective process; however, further advancements in FSSW will make it more economically competitive.

It must be stressed at the outset that the objective in this particular study involves comparing the factors which determine the overlap shear strength properties of RSW and FSSW spot welded joints in dual-phase steel. A single pulse welding schedule was used in the RSW case and optimizing the welding schedule to minimize centerline growth of the columnar grains may further improve mechanical properties. Also a smooth pin FSSW tool design was used when welding dual-phase sheet a limited range of welding parameter settings. As a

result the output produced in this paper should be regarded only as a nominal starting point for future research. The fracture loads produced during overlap shear testing of spot welded dual-phase sheet should therefore are not indicative of the highest values which can be obtained when the steel sheet is spot welded.

6.7 Summary

In this chapter resistance and friction stir spot welding of DP600 was compared. Both processes exhibit potential in spot welding sheet metal for automotive applications. Microstructure and mechanical properties of welds were examined. Energy inputs and bonded areas compared. In addition, the fracture paths and failure modes were detailed.

CHAPTER 7: CONCLUSION

7.1 Microstructure

The microstructure of base metal and spot welded AHSS was characterized. From this work, the following conclusions were made:

1) A multiphase microstructure was observed in the base metal of each sheet steels. The base metal consisted of a ferrite matrix combined with a additional phases which can include retained austenite, martensite and carbides.

2) Typical IC HAZ microstructure comprised of undissolved ferrite and dispersed martensitic islands. TRIP exhibited some retained austenite within the IC HAZ.

3) FZ and IC and FG HAZ mainly comprised of martensite for the rich chemistry AHSS alloys. Leaner chemistry HSLA showed area of ferrite and bainite in the CG HAZ while bainite and martensite was observed in the FZ.

4) The FSSW weld microstructure consisted of a TMAZ between the HAZ and the stir zone. This region consists of a mixture of lathy martensite, bainite and ferrite. Martensite is observed in both the FZ and stir zone of the RSW and FSSW welds, respectively. The morphology of the microstructure; however, is very different for both processes.

7.2 Mechanical Properties

The mechanical properties and microstructure of various RSW AHSS were examined. A correlation between base metal chemistries and fusion zone hardness was determined. From this it was concluded that:

1) All welds exhibited higher failure loads with increased energy inputs until expulsion limits. DP780 produced the highest failure loads per energy input compared to the other materials tested.

2) Materials having elevated carbon equivalence experience increased FZ hardness indicated a strong correlation between chemistry and mechanical properties**.**

3) The sole use of carbon content is not sufficient in predicting FZ hardness. Differing alloying contents must be taken into account. The Yurioka CE equation shows a correlation for FZ hardness values and BM chemistries. FZ hardness can be estimated for a single pulse weld with a 5 cycle hold time using the following equation:

$$Hv_{FZ} = 630 * CE_{Y} + 188$$

5) The microstructure hardness is similar in the FZ and stir zone for RSW and FSSW, respectively. The hardness decreases from the weld centerline into the BM; however, the HAZ in RSW case was narrower.

7.3 Failure Analysis

The fracture surfaces and impact performance of spot welded AHSS was examined. Fracture surfaces for welds conducted during schedule optimization were examined. A comparison was conducted by observing failure loads, displacement, energy absorption, and fracture surfaces for static, intermediate and impact test velocities. Some key conclusions include:

1) Failure loads during tensile shear testing increased as test velocities increased. HSLA and 590R showed a decrease in displacement and energy absorption at impact test velocities.

2) Partial interfacial failure was observed for the TRIP780 and HSLA. Fracture propagated through the HAZ and into the FZ during quasi-static test velocities.

3) Button pull-out failure modes were attained for 590R and DP780 for all test velocities. Brittle interfacial failure consistently occurred when testing DP600. This resulted in its poor impact performance. HAZ softening observed in DP780 contributed to ductile pull-out failure modes.

7.4 Resistance and Friction Stir Spot Welding

In this study mechanical and metallurgical properties of RSW and FSSW DP600 welds were compared. A correlation was found between failure loads, energy requirements and bonded area for both processes. Also, partial tensile shear can be used to understand the initiation and propagation of cracks. From this it can be concluded that:

1) The microstructure of the HAZ is similar in both RSW and FSSW welds in DP600 AHSS. The IC and FG sub-regions consist of a mixture of martensite and ferrite. The martensite occurs as islands in a ferrite matrix, with increasing martensite volume fraction towards the weld centerline.

2) In the case fore RSW, fracture initiates between the two sheets and propagates through the interface of the material. For the FSSW welds, fracture initiates at the unbonded region and propagates through the

upper sheet just under the shoulder, suggesting a need for further optimization of tool geometry.

3) The failure load increased when the bonded area increased for both processes. Failure loads also increased with increase of energy input into the weld. The weld efficiency of both processes is similar for DP600 sheet steel when compared on a basis of fracture load vs. energy or bonded area.

APPENDIX A

HSLA Tensile Testing Data (N)

8000 amps

Force / Time	10	15	20
3.5	2378.925	4343.0832	4422.74
4.5	877.6026	4038.777	5396.677
5.5	758.313	4168.269	5836.95

9000 amps

Force / Time	10	15	20
3.5	1057.91	4771.996	9161.363
4.5	3865.532	7910.588	8947.309
5.5	4436.867	7736.166	8642.218

10000 amps

Force / Time	10	15	20
3.5	8026.738		
4.5	7785.8		
5.5	7907.65		

HSLA Peel Testing Data (mm)

	10	15	20
3.5	0	0	0
4.5	0	1.795	2.731
5.5	0	2.295	2.871

	10	15	20
3.5	0	2.015	5.598
4.5	1.692	4.408	5.751
5.5	2.788	4.435	5.291

	10	15	20
3.5	4.525	6.02	
4.5	4.436	5.985	
5.5	4.325		

TRIP780 Tensile Testing Data (N)

7000 amps

Force / Time	10	15	20
3.5	0	1149.405	2809.976
4.5	0	3337.95	5155.94
5.5	0	4121.77	5069.808

8000 amps

Force / Time	10	15	20
3.5	2758.77	10410.18	13017.87
4.5	8234.71	11828.9	13808.56
5.5	6194.034	11316.82	1372.93

9000 ams

Force / Time	10	15	20
3.5	11752.38	15909.37	
4.5	12962.93	16235.55	
5.5	12240.92	15450.75	

TRIP780 Peel Testing Data (mm)

	10	**15**	**20**
3.5	0	0	0
4.5	0	0	0
5.5	0	0	0

	10	**15**	**20**
3.5	0	2.54	3.305
4.5	1.81	3.161	3.306
5.5	0	2.588	3.816

	10	**15**	**20**
3.5	3.065		
4.5	3.5625		
5.5	3.086		

590R Tensile Testing Data (N)

7000 amps

Force / Time	10	15	20
3.5	4386.64	8389.512	10127.84
4.5	4449.62	9200.9952	11828.9
5.5	1803.667	7846.6266	10214.17

8000 amps

Force / Time	10	15	20
3.5	8172.515	13610.39	14585.51
4.5	9420.151	13704.57	14028.3
5.5	7591.763	12633.32	13800.71

9000 ams

Force / Time	10	15	20
3.5	13253.31	14175.45	0
4.5	13247.42	14454.05	0
5.5	12456.74	14361.84	14885.69

590R Peel Testing Data (mm)

	10	15	20
3.5	3.86	3.658	4.191
4.5	0	3.959	4.813
5.5	0	3.315	4.296

	10	15	20
3.5	3.7075	5.388	5.907
4.5	4.2	5.347	5.796
5.5	3.556	5.163	5.744

	10	15	20
3.5	0	0	
4.5	5.112	7.133	
5.5	4.818	6.298	7.057

DP780 Peel Testing Data (mm)

7000 amps

Time \ Force	10	15	20
3.5	0	5972.13	8201.55
4.5	2732.87	9296.355	12470.47
5.5	6391.61	10667.39	11921.11

8000 amps

Time \ Force	10	15	20
3.5	7124.81	16166.88	16176.69
4.5	12719.65	16853.58	0
5.5	10761.57	15413.47	16431.75

9000 ams

Time \ Force	10	15	20
3.5	16529.85		
4.5	16000.11		
5.5	14589.43	17361.74	16441.56

DP780 Tensile Testing Data (N)

	10	**15**	**20**
3.5		2.4183	3.457
4.5	2.91	3.639	4.671
5.5	2.368	4.437	4.664

	10	**15**	**20**
3.5	3.55	5.4212	
4.5	4.63		
5.5	4.37	5.587	5.938

	10	**15**	**20**
3.5			
4.5			
5.5	5.53	7.436	

REFERENCES

1 A/SP AHSS Applications Recommendations, February 8, 2005

2 Tawade, G. and Boudreau, G., "Robust Schedules for Spot Welding Zinc-Coated High Strength Automotive Steels," Great Design in Steel (2004).

3 D. Giroux, M. B. Vieth and J. F. Deffenbaugh “Resistance welding manual”, 4th edn, 1–1, 1–2; 1999, Philadelphia, PA, USA, Resistance Welder Manufacturers” Association.

4 Kunishige, K., Yamauchi, N., Taka T. and Nagao, N. 1983. Softening in Weld Heat Affected Zone of Dual Phase Steel Sheet for Automotive Wheel Rim, SAE Technical Paper Series #830632, SAE Int. Congress & Exposition, Detroit, MI, Feb 28-Mar 4.

5 Ghosh, P.K., Gupta, P.C., Pal, O.M., Avtar, R., Jha, B.K., and Sagar Dwivedi, V. 1993.Influence of Weld Thermal Cycle on Properties of Flash Butt Welded Mn-Cr-Mo Dual Phase Steel. ISIJ Int. 33 (7): 807-815.

6 Ghosh, P.K., Gupta, P.C., Avtar, R., and Jha, B.K. 1991. Weldability of Intercritical Annealed Dual-Phase Steel with the Resistance Spot Welding Process. Weld. J. 70 (1):7-s to 14-s.

7 Tawade, G. and Boudreau, G., "Robust Schedules for Spot Welding Zinc-Coated High Strength Automotive Steels," Great Design in Steel (2004).

8 Zhang, H., Senkara, J, “Resistance Welding: Fundamentals and applications”, Taylor & Frances, Boca Raton, 2006

9 Tsai, L., Jammal, O. A., Papritan, J. C., and Dickinson, D. W., Modelling of Resistance Spot Weldin Nugget Growth, Welding Journal, pp.47-s-54-s, 1992

10 Gedeon, S.A. , Eagar, T.W., Metall. Trans. B., 1986, vol. 17B, pp. 887-901.

11 Saito, T.: Weld. Int., 1992, vol. 6 (9), pp. 695-99.

12 Howe, P., Kelly, S. C., “A Comparison of the Resistance Spot Weldability of Bare, Hot-Dipped, Galvannealed, and Electrogalvanized DQSK Sheet Steels”, International Congress and Exposition, Detroit Michigan, February 29-March 4, 1988.

13 Auto Steel Partnership “Advance High Strength Steel Application Guidelines”, IISI, March 2005

14 ANSI/AWS/SAE, “Recommended Practices for Evaluating the Resistance Spot Welding Behavior of Automotive Sheet Steel Materials” 1997

15 RWMA, “Resistance Welding Manual” 4th edition, 2003.

16 Hofman, K., Soter, M. , Orsette, C., Villaire, S. , Prokator, M. “ AC or DC for Resistance Welding Dual Phase 600?”, Welding journal, vol:84 iss:1 pg:46 -48, 2005

17 Khan, M.I. , Kuntz, M.L., Zhou, Y, Chan, K. and N Scotchmer. ”Monitoring the Effect of RSW Pulsing on AHSS using FEA (SORPAS) Software” SAE technical paper (2007-01-1370), 2007

18 Dickinson, D.W., “Welding in the Automotive Industry”. AISI Report SG81-5, August, 1981.

19 Finlay, M. R., “Resistance Spot Welding of Metallic Coated Steels and PVD Coated Electrodes”, CRC Australia and WTIA, CRC No. 18, 1996

20 Natale, T.V., “ A review of the resistance spot welding behaviour of galvanized steels”, Sheet Metal Welding conference III, Detroit, USA, October 1988, Paper No. 1

21 Specific Heat of Solids, Cezairliyan A., and Anderson A. , Eds., Hemisphere Publ. Corp., Ney York (NY), 1988

22 S. Kou, Welding Metallurgy , Wiley-Interscience,1997

23 Callister W. D., Jr., “Materials Science and Engineering: An Introduction”, 6th Ed., John Wiley & Sons, Inc, New York, 2003.

24 Dearden, J, O”Niel, L, H.: Trans. Int. Weld., 3, 1940, 203.

25 Heisterkamp, F.: Metallurgical Concept And Full-Scale Testing of High Toughness, H2S Resistant 0.03%C- 0.10%Nb Steel. C.B.M.M. Report, São Paulo, February 1993.

26 Bastien, P.G.: Met. Constr. British Weld. J., 49, 1970, 9.

27 Kihara, H. et al. Technical Report of JRIM, 1, 1959, 93.

28 British Standard Institute. Dec. 1974 Specification for metal-arc welding of carbon and carbon manganese steels. BS5135.

29 Ito, Y., and Bessyo, K, 1968. Cracking Parameter of high strength steels related to heat-affected-zone cracking – Rep. 1. J. of Japan Welding Society 37(9):683-991.

30 Yatake, T., Yurioka, N. , Kataoka, R. , and Tsunetomi, E. 1980. Prevention of root cracking in multi-pass weld. J. of Japan Welding Society 49(7): 484-489.

31 Suzuki, H. 1979. Cold cracking and its prevention in steel welding – Rep. 2. Trans. Japan Welding Society 10(2):82-91.

32 Yurioka, N., Suzuki, H., Ohshita, S., Saito, S. " Determination of Necessary Preheating Temperature in Steel Welding,", Welding Journal, pp 147-153, 1983

33 Stout, R. D., Vasudevan, R., 1968. "Cracking parameter of high strength steel related to heat-affected-zone cracking –REP 1". Journal of Japan Welding Society, 37(9): 683-991

34 Kimichi, M., "Spot Weld Properties when Welding with Expulsion-A Comparative Study" Welding Journal, v 63, n 2, Feb, 1984, p 58-s-63-s

35 Banerjee, K., Chatterjee, U.K. "Effect of microstructure on hydrogen embrittlement of weld-simulated HSLA-80" Metallurgical and Materials Transactions A (Physical Metallurgy and Materials Science), v 34A, n 6, June 2003, p 1297-309

36 Dinda, S., Belleau, C.; Kelley, D. K. "High Strength Low Alloy Steel in Automotive Structures" , ASM, 1984, p 475-483

37 Dufourny, J., Bragard, A. , "Resistance Spot Welding of High Strength Low Alloy (HSLA) Steel Sheet- A Survey" Welding in the World, v 23, n 5-6, 1985, p 100-123.

38 Yoshinobu Omiya, et al., "Characteristics of 590MPa Grade Low YP Type Hot Dip Galvannealed Steel Sheet", Dec. 2002, R & D Kobe Steel Engineering Reports, vol. 52, No. 3, pp. 10-14.

39 Hilditch, T B, Matlock, D K, Levy, B S, Siekirk, J F, "Experimental Evaluation of Curl and Tensile Properties of Advanced High Strength Sheet Steels", S.A.E. transactions [0096-736X] vol:113 iss:Section 5, 2005

40 Hancock, R., 2004, "Friction welding of Aluminum Cuts Energy Cost by 99%," Welding Journal, vol. 83, pp. 40.

41 Gerlich, A., Su, P., North, T.H., Bendzsak, G.J., Friction stir welding of aluminum and magnesium alloys, accepted for publication, Proceedings of The 3rd International Conference on Advanced Materials Processing ICAMP-3, Melbourne, Australia, Nov. 29 to Dec.1 2004.

42 Weber , G., Goklu, S. , “Resistance Spot Welding of Uncoated and Zinc Coated Advance High”, Welding in the World, Vol. 50, No ¾, 2006

43 T. Kim, H. Parka and S. Rhee, “ Optimization of welding parameters for resistance spot welding of TRIP steel with response surface methodology”, International Journal of Produciton Research, Vol. 43, No. 21, 2005

44 Poggio D., Ponte M., Gambaro C and Adamowski J., “Resistance spot welding of advance high strength steel DP600” Proc. From Super High Strength Steel, Italy, 2005

45 Tawade, G.K.C. , Bhole, S.D. , Lee, A.P. “Robust Schedule for Spot Welding Zinc Coated Advance High Strength Automotive Steel”, Technical Document TP05PUB99, SME, 2005

46 Tumuluru M. D, “An Overview of the Ressitance Spot Welding of Coated High-Strength Dual-Phase Steels” Sheet Metal Welding Conference XII, Levonia Michigan May 2006

47 Uijl, N. ,Smith, S. “Resistance Spot Welding of Advance High Strength Steels for the Automotive Industry”, Advanced in Resistance Spot Welding, Austria, 2006

48 Marya, M. , Gayden, X. G. , “Development of Requirements for Resistance Spot Welding Dual-Phase (DP600) Steels: Part 1- The Causes of Interfacial Fracture”, Welding Journal, November 2005.

49 Ewing, K., W., Cheresh, M. , Thompson, R., Kukuchek, P., “Static and Impact Strengths of Spot-Welded HSLA and Low Carbon Steel: SAE technical paper 820281, 1982.

50 Peterson,W., Orth, F., “ Fracture Transition Behavior of Spot Welds in Advance High Strength Steels” , Sheet Metal Welding Conference XII, Livonia Michigan, May 2006.

51 Johnson, C. D, “Handbook of Electrical and Electronic Technology”, p 51-57 1996

52 Gerlich, A., Su, P., North, T.H. " Tool penetration during friction stir spot welding of Al and Mg alloys", J. Materials Science, Vol. 40(24), pp. 6473-6481.

53 A. Gerlich, P. Su, T. H. North and G.J. Bendzsak, Friction stir spot welding of Al and Mg alloys, in press, Materials Forum Volume 29 (ISBN: 1 876855 20 7), 2005.

54 R. Fernie and N.A. Warrior, Impact test rigs for high strain rate tensile and compressive testing of composite materials, Technical note, Strain, Volume 38, 2002, 69-
73

55. Frank S. Lepera, Improved etching technique to emphasize martensite and bainite in high-strength dual-phase steel, pp 38-39, Journal of Metals, March, 1980.

56 Caballero, F. G. , Andrea, G. , Carlos C., Garcia, D. C., "Evolution of microstructural banding during the manufacturing process of dual phase steels", Materials Transactions, v 47, n 9, September, 2006, p 2269-2276

57 Pichler, A., Traint, S. , Amoldner, G. , Stiaszny, P. , Blaimschein, M., Werner, E. A. "High-Strength Hot-Dip Galvanized Steel Grades: A Crtitical Comparison of Alloy Design, Line Configuration and Properties" 44th MWSP Conference Proceedings, Vol. XL, 2002

58 Rosenthal, D. 1941. Mathematical theory of heat distribution during welding and cutting. Welding Journal 20(5): 220-s to 234-s.

59 Chuko, W, and Gould, J. E. 2002. Development of appropriate resistance spot welding practice for transformation-hardened steels - phase 2: evaluation of post-weld cooling rate techniques. Report to the American Iron and Steel Institute.

60 Adams, C. M. Jr. 1958. Cooling rates and peak temperatures in fusion welding. Welding Journal 37(5): 210-s to 215-s.

61 Callister, W., D., "Fundamentals of Materials Science and Engineering", John Wiley and Sons Ltd, 2004

62 Yurioka, N, Okumura, M; Kasuya, T; Cotton "Prediction of HAZ Hardness of Transformable Steels" Met. Constr. Vol. 19, no. 4, pp. 217R-223R. Apr. 1987

63. Gould, J. E., Khurana S. P., Li, T. "Prediction of Microstructures when Welding Automotive Advance High-Strength Steels", Welding Journal, v. 85, no5, may 2006, 111- 116.

64 Marya, M. , Gayden, X. Q. “Development of Requirements for Resistance Spot Welding Dual-Phase (DP600) Steels Part 1 – The causes of interfacial Fracture”, Welding Journal, November 2005, pp. 172s – 182s.

65 Uijl, N. , Smith, S., “Resistance Spot Welding of Advance High Strength Steels for the Automotive Industry”, Advanced in Resistance Spot Welding, Austria, 2006

66 Kwon, H., Kim, C.M., Lee, K.B., Yang, H.R., Lee, J.H. “Effect of Alloying Additions on Secondary Hardening Behavior of Mo-Containing Steels”, V. 28A, No. 3, March 1997

67 Yurioka, N., Suzuki, H., Ohshita, S., Saito, S. “Determination of necessary Preheating Temperatures in Steel Welding”, pp 147-153, Welding Journal, June, 1980.

68 HC Chen, H Era and M Shimizu, "Effect of Phosphorus on the Formation of Retained Austenite and Mechanical Properties in Si-Containing Low-Carbon Steel Sheet," MetTrans A, V20A, 1989, P437-445

69 Zwaag, S. van der, Wang, J., “A discussion on the atomic mechanism of the bainitic reaction in TRIP steels”, Scripta Materialia 47 (2002) 169–1

70 N. Uijl, S. Smith: “Resistance Spot Welding of Advance High Strength Steels for the Automotive Industry”, pp30-62, Advances in Resistance Welding, Austria, November, 2006.

71 I. Khan, M.L. Kuntz, P. Su, A. Gerlich, T. North, Y. Zhou: “Resistance and friction stir spot welding of DP600: A comparative study”, accepted, September 2006.

72 Xia, M., Sreenivasan, N., Lawson, S., Zhou, Y., Tian, Z., “A Comparative Study of Formability of Diode Laser Welds in DP980 and HSLA Steels” Journal of Materials Science and Engineering A , Accepted

73 Frommeyer, G. Brux and Neumann, P. “ Supra –Ductile and High-Strength Manganese TRIP/TWIP Steels for High Energy Absorption Purposes,” ISIJ International, Vol, 43, No 3, pp. 438-446 (2003)

74 Peterson, W., Orth, F.,” Fracture Transititon Behavior of Spot Welds in Advance High Strength Steel”, SMWC XII, Livonia Michigan, 2006.

75 Ewing et al , “Static and Impact Strength of Spot Welded HSLA and low carbon steel joints” paper # 820281, 1982

76 Khan, M.I., Kuntz, M.L., Zhou, Y., Chan K., Scotchmer, N., ”Monitoring the Effect of RSW Pulsing on AHSS using FEA (SORPAS) Software” SAE technical paper (2007-01-1370), 2007

77 Biro, E., Lee, A. “Tensile Properties of Gleeble_Dimulated HAZ from Various Dual-Phase Steels” SMWC XII, Livonia MI, 2006.

78 Uijl, N., Smith, S., “Resistance Spot Welding of Advance High Strength Steels for the Automotive Industry”, pp30-62, Advances in Resistance Welding, Austria, November, 2006.

79 Gerlich, A., Su, P., North, T. H., Bendzsak, G.J., Materials Forum 29, 290-294.

80 Ding, R. J., “Retractable Pin-Tool Technology for Friction Stir Welding”, ASM Proceedings of the International Conference: Trends in Welding Research pg:585 -589

81 S. A. G. T. W. Eagar: Metallurgical Transaction B, 1986, 17B, 887-901.

82 Y. Z. W. Tan, H.W. Kerr: metallurgical and materials transaction A, 2002, 33A, pg:2667 -2676

83 P. S. A. Gerlich, T.H. North: Science and Technology of Welding and Joining, 2006, 29, 647-652.

84 N. Z. S. Dong, C Cheng, Y. Shi, B. Chang: Transactions of the Nonferrous Metals Society of China, 2005, v 15, pg:1219 -1225.